



HAL
open science

Slow light in two dimensional semi-conductor photonic crystals

Patricio Grinberg

► **To cite this version:**

Patricio Grinberg. Slow light in two dimensional semi-conductor photonic crystals. Other [cond-mat.other]. Université Paris Sud - Paris XI, 2012. English. NNT : 2012PA112316 . tel-00830962

HAL Id: tel-00830962

<https://theses.hal.science/tel-00830962>

Submitted on 6 Jun 2013

HAL is a multi-disciplinary open access archive for the deposit and dissemination of scientific research documents, whether they are published or not. The documents may come from teaching and research institutions in France or abroad, or from public or private research centers.

L'archive ouverte pluridisciplinaire **HAL**, est destinée au dépôt et à la diffusion de documents scientifiques de niveau recherche, publiés ou non, émanant des établissements d'enseignement et de recherche français ou étrangers, des laboratoires publics ou privés.

UNIVERSITE PARIS-SUD XI

École doctorale Ondes et Matière

Laboratoire de Photonique et de Nanostructures

PHYSIQUE

THÈSE DE DOCTORAT

Soutenue le 26 novembre 2012

par

Patricio GRINBERG

Slow light in two dimensional semi-conductor photonic crystals

Directeur de thèse:	Ariel LEVENSON	DR, LPN
Encadrant:	Kamel BENCHEIKH	CR, LPN

Composition du jury:

Président du jury:	Fabien BRETENAKER	DR, LAC
Rapporteurs:	Xavier LETARTRE	DR, INL
	Hervé MAILLOTTE	DR, Institut FEMTO-ST
Examineurs:	Philippe LALANNE	DR, LP2N
	Jean-Michel RAIMOND	Professeur, LKB

Acknowledgments

First of all I would like to acknowledge my tutors, Kamel Bencheikh and Ariel Levenson. Kamel for all the day to day support, for being always available and the patience. Ariel for being always there, the support, the positive energy and for always pushing forward.

I would like to acknowledge Fabien Bretenaker, Xavier Letartre, Hervé Maillotte and Jean-Michel Raimond for their participation in thesis jury.

I would like to acknowledge everybody in the Laboratory of Photonics and Nanostructures. The director, Dominique Mailly, for receiving me at the laboratory. I would also like to acknowledge the people involved in the fabrication of the samples used for this thesis, Isabelle Sagnes, Fabrice Rainieri and Alexandre Bazin.

I acknowledge everybody in the PHOTONIQ group. Alejandro Giacomotti for all the theoretical and experimental discussion and advices but also for the reception and the advices in sciences and others. Maia Brunstein and Samir Haddadi for the help in the experiments. Philippe Hamel for experiments and the discussions. Paul Monier for being always there to help solve all the eventual experimental problems.

I would like to acknowledge Philippe Lalanne, Christophe Sauvan and Yannick Dumeige for all the help in theory and the numerical calculations.

Y a vos, mi amor, gracias por todo, gracias por la paciencia, por el aguante, por motivarme cuando no quería más, por aguantarme, por aguantarme y, sobre todo, por aguantarme.

a Vero

(y J.R.R.)

Lumière lente par interactions non linéaires et cavités à cristaux photoniques

La première mesure expérimentale de la vitesse de la lumière a été réalisée en 1848 par Hippolyte Fizeau [Fizeau 1849] utilisant une méthode de temps de vol. Il a mesuré le temps qu'il faut à une impulsion optique créée avec une roue dentée tournante, pour faire l'aller-retour entre deux miroirs fixes: l'un à son domicile à Suresnes et l'autre à Montmartre à Paris. Cette mesure pionnière de Fizeau a encore été améliorée par le remplacement de la roue dentée par un miroir tournant et en augmentant la distance de propagation. On sait que la vitesse mesurée par Fizeau est ce qu'on appelle la vitesse de groupe, v_g , et que celle-ci peut être manipulée et particulièrement réduite considérablement par rapport à la vitesse de la lumière dans le vide $c = 300000$ km/s.

Les premières études théoriques de propagation de la lumière dans les médias avec des vitesses de groupe réduites remontent à 1880 lorsque Lorentz [Lorentz 1880] a développé la théorie classique de la dispersion des ondes électromagnétiques. La propagation lente des ondes électromagnétiques a été observée pour la première dans la gamme des micro-ondes en 1950 [Pierce 1950].

Ce champ a été au cœur d'intenses recherches depuis deux décennies. En 1999, L.V. Hau et ses collègues ont été les premiers à obtenir de la lumière lente via transparence induite électromagnétiquement (TIE) dans un condensat de Bose-Einstein [Hau 1999]. L'effet consiste à produire un trou spectral d'absorption étroite qui induit une forte dispersion de l'indice de réfraction. De nombreux groupes sont aujourd'hui en mesure de ralentir la vitesse de la lumière atteignant des vitesses de groupe de quelques mètres par seconde [Baldis 2005], allant jusqu'à arrêter le mouvement de la lumière entièrement [Phillips 2001].

Une voie alternative à l'approche atomique a également été intensivement explorée afin de manipuler la vitesse de groupe pour obtenir la lumière lente. Il s'agit de la manipulation du diagramme de dispersion photonique via l'ingénierie géométrique des propriétés optiques de matériaux transparents. C'est particulièrement le cas dans les structures où il ya une variation périodique de la constante diélectrique, comme dans les miroirs de Bragg et les cristaux photoniques (CP) [Notomi 2001].

Les deux options pour générer une lumière lente, dispersion atomique et structuration de matériaux ont été explorées en parallèle par des équipes venant d'horizons différents. Ce n'est que récemment que les deux approches ont commencé à être considérées ensemble, générant un intérêt accru ainsi que quelques controverses. Du côté structuration, il est maintenant largement admis que des indices de groupe, $n_g = c/v_g$, supérieurs à 30 sont difficilement réalisables avec des CP en raison de la forte augmentation des pertes qui suivent au moins une dépendance linéaire en n_g . Par contre, des vitesses de groupe ultra faibles, plus de 5 ordres de grandeur inférieures à c , sont actuellement obtenues par TIE et par le biais du phénomène des oscillations cohérentes de la population (OCP) [Boyd 1981]

dans des systèmes atomiques. Par ailleurs, la transmission optique pour être proche de 100 %, en dépit de l'indice de groupe extrêmement élevé. Les pertes sont donc indépendantes de l'indice de groupe. Ce paradoxe apparent est facilement résolu si l'on considère les mécanismes physiques mis en œuvre dans ces approches qualitativement différentes. La lumière lente induite par structuration de la matière est essentiellement associée au temps de retard introduit par l'augmentation de la distance de propagation. La lumière lente obtenue par des interactions non linéaires n'est pas associée à l'augmentation de la distance de propagation et ne génère donc pas de pertes supplémentaires. Ce débat soulève la question de bénéficier des atouts des deux approches en combinant dans la même structure la lumière lente obtenu par interaction non linéaire et la lumière lente obtenue par l'ingénierie des indices de refractions.

L'étude de cette association de lumières lentes et l'objet de ma thèse. Je commence par rappeler les différentes façons qui permettent d'obtenir la lumière lente (partie I).

Dans le chapitre 1, je décris l'effet des oscillations cohérents de population (OCP) utilisé dans cette thèse pour obtenir une forte dispersion de l'indice de réfraction dans les puits quantiques semi-conducteurs, et ainsi la lumière lente par effet non linéaire. Dans le chapitre suivant 2, je donne une brève description des cristaux photoniques (CP) et je montre comment ils peuvent être utilisés pour construire des nanocavités, des guides d'ondes et comment les CPs induisent des indices de groupe élevés.

La thèse est par la suite séparée en deux parties. La partie II est consacrée au ralentissement de la lumière par effet OCP dans des cavités à CP, tandis que la partie III est consacrée à la combinaison des modes lents de guides d'ondes à CP avec la lumière lente obtenue par effet OCP.

Dans la partie II, je commence (dans le chapitre 3) en décrivant théoriquement l'effet OCP dans une cavité en utilisant la théorie des modes couplés. La description théorique montre que le comportement non linéaire de la cavité provoquée par les puits quantiques actives ne peut pas être négligé, ni dissocié de l'effet OCP. Ensuite, dans le chapitre 4, le dispositif expérimental et les résultats obtenus sont présentés et confrontés à la théorie. Une forte augmentation de la durée de vie est démontrée, obtenant un facteur de qualité équivalent de 520000 qui correspond à une amélioration d'un facteur 138 par rapport au facteur de qualité initial de la cavité à CP.

La partie III est dédiée à l'association de la lumière lente par effet OCP aux modes lents des guides d'ondes à CP. Je commence dans le chapitre 5 en développant un modèle perturbatif simple pour mieux comprendre l'évolution de l'indice du groupe et l'absorption du système lorsque l'effet OCP est associé avec le mode lent du guide à CP. Cette model perturbative montre que l'interaction lumière matière a une dépendance linéaire avec l'indice de groupe initial due à la structuration du matériau formant le guide à CP, et ne depend pas de l'indice de groupe associé à l'effet OCP. Dans le chapitre 6, je présente la problématique du couplage de la lumière dans un guide d'onde à CP et propose une système alternative pour coupler la lumière dans

le guide d'ondes de l'espace libre en utilisant une super réseau. Ce système est aussi validé expérimentalement dans des guides d'ondes à CP transparents (sans puits quantiques). Le chapitre 7 présente les résultats préliminaires sur les guides d'ondes à CP actives et montrent des retards importants par rapport au retards obtenues sans l'effet OCP.

Le chapitre 8 donne, enfin, les conclusions et les perspectives de ce travail.

Contents

I	Introduction	1
1	Slow light by nonlinear means	7
1.1	Coherent Population Oscillations	7
1.1.1	Theory of Coherent Population Oscillations effect	8
1.1.2	CPO in semiconductors	11
2	Photonic Crystals	13
2.1	1D photonic crystal	13
2.2	2D photonic crystal	14
2.3	Photonic crystal cavities	15
2.4	Photonic crystal waveguides	17
II	Slow light in photonic crystal cavities	21
3	Theoretical Model	25
3.1	CPO effect in a microcavity: Basic approach	26
3.2	CPO and nonlinear effects in a Fabry-Perot cavity	28
3.3	Model for CPO in a semiconductor nonlinear microcavity	33
3.4	Analytical results	35
3.4.1	First order calculations	35
3.4.2	Asymptotic behavior	36
3.5	Numerical results	40
3.5.1	Absorptive nonlinearity	40
3.5.2	Dispersive nonlinearity	45
3.6	Conclusion	45
4	Experimental Demonstration	47
4.1	The L3 PhC cavity	48
4.1.1	Fabrication of the L3 PhC cavity	49
4.1.2	Photoluminescence characterization of the L3 PhC cavity	51
4.2	Tapered fiber assisted coupling into the L3 PhC cavity	52
4.2.1	Fabrication and characterization of the tapered fiber	52
4.2.2	Coupling efficiency	53
4.3	Pump and probe generation	55
4.4	Optical Detection	56
4.4.1	Measurement of the delays	57
4.5	Temporal Measurements	62
4.6	Spectral Measurements	66
4.7	Frequency Pulling	67

4.8	Theoretical and experimental comparison	69
III	Slow light in photonic crystal waveguides	75
5	Theoretical studies	79
5.1	1D model	79
5.2	Perturbative model	84
5.2.1	Lorentz reciprocity theorem	85
5.2.2	First-order perturbation theory	86
5.3	Numerical simulations	89
6	Coupling into a W1 waveguide	93
6.1	Lateral coupling	94
6.1.1	Sample fabrication	95
6.1.2	Cleaving process	97
6.2	Vertical coupling	98
6.2.1	Theoretical calculations	99
6.2.2	Experimental validation of the coupler and measurement of the group index	105
6.3	Conclusion	114
7	Active W1 waveguides	115
7.1	Experimental method	115
7.2	Experimental results	117
IV	Conclusions and prospects	123
8	Conclusions and prospects	125
8.1	Conclusions	125
8.2	Prospects	126
	Bibliography	129

Part I

Introduction

The first experimental measurement of the speed of light was performed in 1848 by Hippolyte Fizeau [Fizeau 1849] using a time of flight method. He measured the time it takes to an optical pulse generated with a rotating cogwheel, to make the round trip between two fixed mirrors, one at his house at Suresnes and the other one at the Montmartre hill in Paris. This Fizeau pioneering measurement was further improved by replacing the cogwheel by a rotating mirror and increasing the propagation distance.

The Fizeau measurement corresponds to what we call nowadays the group velocity. The group velocity v_g is the velocity at which a pulse envelope propagates (see figure 1) in a medium with a refraction index $n(\omega)$, where ω is the optical circular frequency. The group velocity is defined as:

$$v_g \equiv \frac{\partial \omega}{\partial k} = \frac{c}{n + \omega \frac{\partial n}{\partial \omega}} \quad (1)$$

where k is the wavenumber. The denominator is called the group index:

$$n_g \equiv n + \omega \frac{\partial n}{\partial \omega} \quad (2)$$

so that $v_g = c/n_g$.

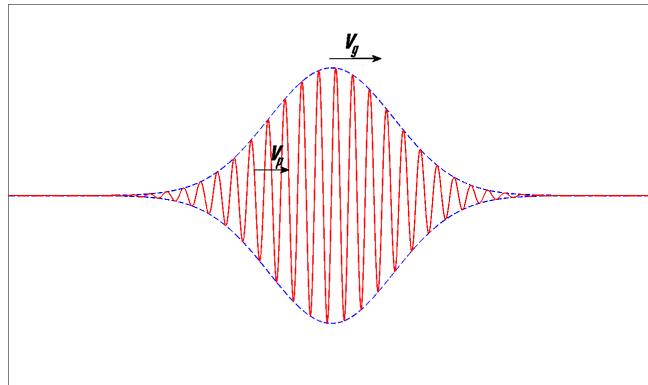


Figure 1: Sketch of a propagating wavepacket.

From equation (2) it is easy to deduce that by modifying the index dispersion $\partial n/\partial \omega$, one can manipulate the group velocity achieving, slow light ($v_g \ll c$), fast light ($v_g > c$) or light propagating with negative group velocity ($v_g < 0$).

The first theoretical studies of light propagation in media with reduced group velocities go back to 1880 when Lorentz [Lorentz 1880] developed the classical theory of dispersion of the electromagnetic waves. Slow propagation of electromagnetic waves was first observed in the microwave range in 1950 [Pierce 1950].

This field has been at the heart of intense research for two decades. In 1999, L.V. Hau and coworkers were the first to obtain slow light via electromagnetically induced

transparency (EIT) in a Bose-Einstein condensate [Hau 1999]. The effect consists in generating a narrow absorption spectral hole that induces a strong dispersion of the refraction index. Many groups are nowadays able to slow down the light achieving group velocities of few meters per second [Baldit 2005] or even stop the motion of light entirely [Phillips 2001].

An alternative avenue that has also been intensively explored is to achieve slow light based on the moulding of the photonic dispersion diagram via the geometrical engineering of the optical properties. Here spectral regions where the derivative $\partial\omega/\partial k$ tends to zero are obtained. This is particularly the case in structures where there is a periodic variation of the dielectric constant, like in Bragg mirrors and photonic crystals [Notomi 2001].

The two options to generate slow light, atomic or atomic-like dispersion and material structuration were explored in parallel by teams coming from quite different backgrounds and that gained a clear cut intuition of the assets and limitations of their slow light approaches. Only recently the two approaches were started to be considered together generating both an increased interest and some controversies. For instance it is well known, from distributed feed-back lasers, that slow light propagation in an active medium periodically structured to induce the laser feed-back, subsequently generates an increasing of the absorption, implemented in such a case in order to increase the gain and achieve laser operation. Below the laser threshold, slow light can be obtained but the increase of the absorption imposes a severe limitation to the group velocity that can be achieved. In other words, it is now largely accepted that group index higher than ~ 30 are hardly achievable in 2D PhC due to the strong increase of losses that follow at least a linear dependence on n_g . Conversely, ultra slow group velocities more than 5 orders of magnitudes lower than c are currently achieved by EIT and Coherent Population Oscillations (CPO) [Boyd 1981]. Moreover, here the optical transmission could be close to 100%, in spite of the extremely high group index. Clearly, in this case, losses are independent on the group index and velocity. This apparent paradox is easily solved when considering the physical mechanisms at work in these qualitatively different approaches. The slow light induced by the material structuring is essentially associated to the time delay introduced by the increase of the propagation distance. This increased path is at the hearth of the exaltation of the light-matter linear and nonlinear interactions and thus generates the increase of the absorption and the additional losses. This is particularly the case in 2D PhC W1 were the slow light explores more efficiently the technological defects of the periodicity surrounding the WG core. In turn, slow light by nonlinear interactions is not associated to the increase of the propagation distance and thus generates no additional loss. This discussion raises the question of benefiting from the assets of both approaches by combining in the same waveguide nonlinearly induced and geometrically engineered slow light.

Only few theoretical papers addressed such a combination. M. Soljačić and co-workers performed numerical approaches [Soljačić 2004, Soljačić 2005a] but, even though, they consider the possibility of slow mode wave guides for enhancing nonlinear effects when considering slow light from non-linear origins, e.g. EIT, they com-

bine it with PhC microcavities. More recently Mork and co-workers [Nielsen 2009] explicitly considered EIT interaction in a W1 waveguide and demonstrated that the combination of slow light by these two origins converges in a multiplication of the two independent group indices regulated by the overlap of the optical mode in the active region. They also did some research about the absorption enhancement [Mørk 2010] and showed that it scales linearly with geometrically engineered group index but it does not have a dependence on the nonlinear group index.

In this thesis I address the problem of such a combination. I start by describing the different means to achieve slow light (part I).

In chapter 1, I describe the Coherent Population Oscillations effect implemented during my thesis in order to achieve strong index dispersion in semiconductor quantum wells, and thus nonlinear slow light propagation. Next in chapter 2, I give a brief description of the Photonic Crystals (PhCs) and show how they can be used to build nanocavities, waveguides and how the PhCs induce high group indices. In chapter 2, I will also give details on the system used during this thesis: the L3 PhC nanocavities and the W1 PhC waveguides. I particularly discuss the problem of coupling and extracting the electromagnetic field in and out the W1 waveguides. Then the thesis is separated in two main parts according to the PhC structure studied. Part II is devoted to the combination of CPO and PhC cavities while part III is devoted to the combination of the slow modes of PhC waveguides with the slow light obtained by CPO effect.

In part II, I start (in chapter 3) by describing theoretically the CPO effect in a cavity using the coupled mode theory. The theoretical description shows that the nonlinear behavior of the cavity induced by the active quantum wells can not be neglected nor dissociated from the CPO effect. Next, in chapter 4, the experimental setup and the obtained results are presented and the experimental and theoretical results are compared. Strong increasing of the photonic lifetimes are therefore demonstrated. These results are also discussed in terms of the enhancement, by an order of magnitude, of the quality factor of the PhC nanocavity.

Part III is dedicated to the association of the CPO-based slow light with the W1 PhC waveguides. I start in chapter 5 by developing a simple perturbative model to gain insight into the evolution of the group index and the absorption of the system when the CPO effect is associated with the slow mode of the W1 PhC waveguide. In chapter 6, I present the problematic of coupling light in a W1 PhC waveguide and the proposed, grating, alternative for coupling light into the waveguide from the free space. I also validate it in transparent W1 PhC waveguides. Chapter 7 presents the preliminary results on active W1 PhC waveguides, that also demonstrate important time delays.

Chapter 8 gives, finally, the conclusions and perspectives of this work.

Slow light by nonlinear means

Slow light propagation is at the heart of intense research activities since two decades. Induced by nonlinear interactions, such as Electromagnetically Induced Transparency (EIT) [Fleischhauer 2005] or Coherent Population Oscillation (CPO), slow light propagation was demonstrated in several systems including cold atoms [Boller 1991, Hau 1999, Inouye 2000], vapors [Kasapi 1995, Kash 1999], rare-earth doped crystals [Bigelow 2003a, Bigelow 2003b, Baldit 2005] and semiconductors [Ku 2004].

These coherent nonlinear interactions induce a strong refractive index dispersion associated to a narrow spectral hole transparency in the absorption spectrum. This narrow window, related to the inverse of hyperfine coherence (EIT) or population (CPO) relaxation times, also determines the temporal accessible bandwidth. Coherent nonlinear interactions are thus particularly interesting to achieve extremely small group velocities that can be tuned by the absorption level or the light intensity.

Slow light based on CPO differs from EIT by several aspects. The main interest of the CPO effect is that it has less restrictions. To achieve the CPO effect there is no need of sophisticated 3-level system, indeed CPO could be implemented at room temperature in any 2-level or 2-level like system provided the population lifetime T_1 is sufficiently greater than the dephasing time T_2 . In contrast to the EIT effect it is population lifetime T_1 that is utilized in the coherent process and not the dephasing time T_2 . CPO is less affected by inhomogeneous broadening [Chang 2005], which is usually inevitable and leads to a variation of the refractive index that is not as sharp [Kim 2004] in semiconductor quantum structures.

1.1 Coherent Population Oscillations

Coherent population oscillations (CPO) was first introduced theoretically by Schwarz and Tan in 1967 [Schwarz 1967] to understand the instabilities observed in dye lasers and also to explain the presence of spectral windows narrower than the homogeneous broadening and close to the natural linewidths. In the same paper, Schwarz and Tan proposed to use the CPO effect as a spectroscopic tool in order to measure the lifetime T_1 of an atomic system when it is too short or when the atomic system is not fluorescent. In 1978 Murray Sargent III [Murray Sargent III 1978] used this approach to spectroscopic studies of the relaxation times.

In 1983, L.W. Hillman et al. [Hillman 1983] observed a 37 Hz half width half maximum (HWHM) dip in the absorption profile of the homogeneously broadened green absorption band of ruby, associated to the CPO effect. Taking benefit of this

narrow hole in the ruby transition, to which a strong index dispersion is associated, Bigelow et al. [Bigelow 2003a] demonstrated slow light propagation in ruby achieving a group velocity of 57 m/s. Since then, a large number of CPO-based slow light propagations have been reported in various media such as alexandrite [Bigelow 2003b], semiconductor structures [Ku 2004, Chang 2004, Palinginis 2005a, Palinginis 2005b, Chang 2005], and erbium-doped crystals [Baldit 2005].

1.1.1 Theory of Coherent Population Oscillations effect

The CPO effect is the main physical phenomenon I am using in the work reported in this thesis. It is then important to give a theoretical description of this effect. The starting point of this description is an ensemble of two-level atomic systems as depicted in figure 1.1, characterized by a lifetime T_1 , a dephasing time T_2 and interacting with two electromagnetic fields: a pump oscillating at ω and a weak probe oscillating at $\omega + \delta$. We further suppose that both fields are close to resonance with the atoms, that is $\omega, \omega + \delta \simeq \omega_{12}$. Due to the temporal interference between the pump and the probe, the population of the atomic systems will oscillate at the beating frequency $\delta/(2\pi n)$, in phase with the interference. The interaction of the pump with a susceptibility oscillating at $\omega \pm \delta$ induces two radiations at $\omega - \delta$ and $\omega + \delta$. This second radiated field coincides with the probe and partially annihilates its absorption. As the beating frequency $\delta/(2\pi n)$ gets larger than the natural linewidth $\Gamma_{ba} = 1/T_1$, the population oscillations decline and the radiated field at $\omega + \delta$ vanishes, retrieving thus the initial absorption of the atomic system.

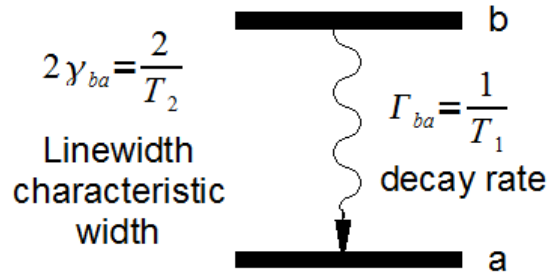


Figure 1.1: Sketch of the 2 level system. T_1 and T_2 are respectively the lifetime of the excited state and the decoherence time.

The CPO effect is a phenomenon driven by the population dynamics. However, I perform here a full theoretical description of the system using the density matrix formalism. The density matrix formalism is more adequate when one has to consider, in addition, the inhomogeneous broadening of the atomic systems. Following the formalism developed in [Boyd 2003] we end up with the following equations:

$$\begin{aligned} \dot{\sigma}_{ba} &= - \left[i\Delta - \frac{1}{T_2} \right] \sigma_{ba} - \frac{i}{\hbar} \mu_{ba} E w \\ \dot{w} &= - \frac{w - w^{\text{eq}}}{T_1} + \frac{2i}{\hbar} (\mu_{ba} E \sigma_{ab} - \mu_{ab} E^\dagger \sigma_{ba}) \end{aligned} \quad (1.1)$$

The first equation describes the evolution of σ_{ba} the coherence of the atomic system in the rotating wave approximation when excited by the electromagnetic field E . μ_{ba} is the dipole moment of the transition, $\Delta = \omega - \omega_{ba}$. The second equation describes the evolution of the population density difference $w = \rho_{bb} - \rho_{aa}$. $w^{\text{eq}} = -1$ is the population difference at equilibrium where all the atoms are supposed to be in the ground state.

Now we rewrite $\langle \hat{\mu} \rangle = \rho_{ba}\mu_{ab} + \rho_{ab}\mu_{ba} = \sigma_{ba}\mu_{ab}e^{-i\omega t} + \sigma_{ab}\mu_{ba}e^{i\omega t}$. Using the definition of the microscopic polarization $p \equiv \mu_{ab}\sigma_{ba}$, then $\langle \hat{\mu} \rangle = \tilde{p}(t) = pe^{-i\omega t} + c.c.$. Equations (1.1) expressed as:

$$\begin{aligned} \dot{p} &= - \left[i\Delta - \frac{1}{T_2} \right] p - \frac{i}{\hbar} |\mu_{ba}|^2 E w \\ \dot{w} &= - \frac{w - w^{\text{eq}}}{T_1} + \frac{4}{\hbar} \Im(E p^\dagger) \end{aligned} \quad (1.2)$$

In order to be in the CPO regime, the atomic systems have to be excited by pump and probe fields oscillating respectively at ω and $\omega + \delta$. However, experimentally most often the pump and probe are obtained from a single laser source which amplitude is modulated sinusoidally at frequency δ , ending in the Fourier space with three spectral components at ω and $\omega \pm \delta$. We consider then that the atomic system are interacting with three fields: the pump $E_p(\omega)$, the signal $E_s(\omega + \delta)$ and the idler $E_i(\omega - \delta)$. We suppose that E_s and E_i are smaller than E_p . Equations (1.2) are solved considering the typical solutions:

$$\begin{aligned} p &= p_0 + p_1 e^{-i\delta t} + p_{-1} e^{-i\delta t} \\ w &= w_0 + w_1 e^{-i\delta t} + w_{-1} e^{-i\delta t} \end{aligned} \quad (1.3)$$

since $w(t) \in \mathbb{R}$, $w_1 = w_{-1}^\dagger$ and then $w(t) = w_0 + 2|w_1| \cos(\delta t + \phi)$ where ϕ is the phase of w .

The susceptibility at $\omega + \delta$ is given by $\chi_{\text{eff}}^{(1)}(\omega + \delta) = N p_1 / E_s$ where N is the density of the atomic systems and p_1 is the microscopic polarization oscillating at $\omega + \delta$. They are obtained by solving the system (1.3).

$$\chi_{\text{eff}}^{(1)}(\omega + \delta) = \frac{N |\mu_{ba}|^2 w_0}{\hbar D(\delta)} \left[\left(\delta + \frac{i}{T_1} \right) \left(\delta - \Delta + \frac{i}{T_2} \right) - \frac{1}{2} \Omega^2 \frac{\delta}{\Delta - i/T_2} \right] \quad (1.4)$$

where $D(\delta) = \left(\delta + \frac{i}{T_1} \right) \left(\delta - \Delta + \frac{i}{T_2} \right) \left(\delta + \Delta + \frac{i}{T_2} \right) - \Omega^2 \left(\delta + \frac{i}{T_2} \right)$ and $\Omega = \frac{2\mu_{ba}E}{\hbar}$ is the pump Rabi frequency.

Now using the definition of the linear unsaturated absorption at the resonance $\alpha_0 = -\frac{N |\mu_{ba}|^2 w^{\text{eq}} \omega_{ba} T_2}{c \hbar \varepsilon_0}$, setting $w_0 = w^{\text{eq}} \frac{1 + \Delta^2 T_2^2}{1 + \Delta^2 T_2^2 + \Omega^2 T_1 T_2}$ and defining the saturation parameter s as the pump intensity normalized to the saturation intensity, which is also related to the Rabi frequency trough $s = \Omega^2 T_1 T_2$, the susceptibility reads:

$$\chi_{\text{eff}}^{(1)}(\omega + \delta) = \frac{-\alpha_0 c \varepsilon_0}{\omega_{ba} T_2 D(\delta)} \frac{1 + \Delta^2 T_2^2}{1 + \Delta^2 T_2^2 + \Omega^2 T_1 T_2} \left[\left(\delta + \frac{i}{T_1} \right) \left(\delta - \Delta + \frac{i}{T_2} \right) - \frac{1}{2} \Omega^2 \frac{\delta}{\Delta - \frac{i}{T_2}} \right] \quad (1.5)$$

As the susceptibility is much smaller than 1 ($|\chi| \ll 1$) we can make a Taylor approximation in first order $\sqrt{1 + \chi} = 1 + \chi/2$, then we can write the absorption and refraction index as:

$$n(\delta) \simeq 1 + \frac{1}{2} \Re[\chi(\omega + \delta)] \quad (1.6)$$

$$\alpha(\delta) = \frac{\omega + \delta}{c} \Im[\chi(\omega + \delta)] \quad (1.7)$$

Figure 1.2 shows $n(\delta) - 1$ and the absorption $\alpha(\delta)$ for an absorption $\alpha_0 = 6.5 \text{ cm}^{-1}$, a saturating parameter $s = 0.5$ and for $T_1/T_2 = 20$. The pump field is supposed to be in resonance with the atomic transition ($\Delta = 0$). A narrow CPO hole appears in the homogeneous absorption line (see figure 1.2.a), to which a steep dispersion of the index of refraction is associated (see figure 1.2.b). The dashed curves are the absorption and the index of refraction in the same atomic systems when only excited by the probe field.

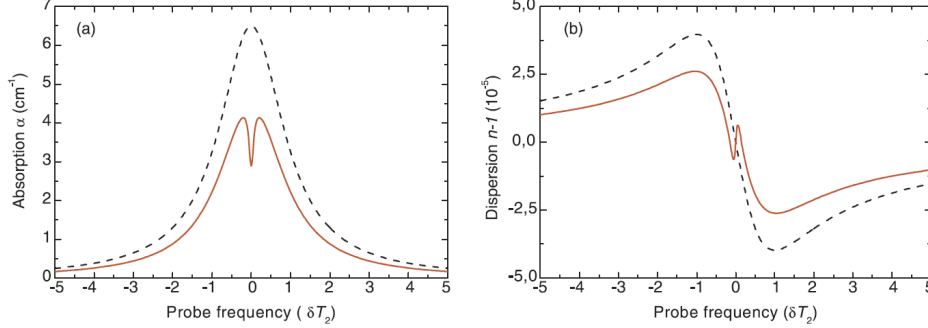


Figure 1.2: Absorption (a) and refraction index $n - 1$ (b) of the probe field when the pump is present (continuous red line) and without the pump (dashed black line). The parameters are $\alpha_0 = 6.5 \text{ cm}^{-1}$, $s = 0.5$, $T_1/T_2 = 20$, and a pump frequency $\Delta \times T_2 = 0$.

Considering a resonant pump ($\Delta = 0$), $T_2 \ll T_1$ and a small pump-probe frequency detuning we can further simplify equations for the absorption and the refraction index:

$$n(\delta) = 1 + \frac{\alpha_0 c T_1}{2\omega} \frac{s}{1 + s} \frac{\delta}{(\delta T_1)^2 + (1 + s)^2} \quad (1.8)$$

$$\alpha(\delta) = \frac{\alpha_0}{1 + s} \left[1 - \frac{s(1 + s)}{(\delta T_1)^2 + (1 + s)^2} \right] \quad (1.9)$$

Using the expression of the refraction index (equation (1.8)) in the expression of the group index (2) we can approximate it as:

$$\begin{aligned} n_g &\simeq 1 + \omega \frac{n(\omega + \delta) - n(\omega - \delta)}{2\delta} \\ &= \frac{\alpha_0 c T_1}{2} \frac{s}{1+s} \frac{1}{(\delta T_1)^2 + (1+s)^2} \end{aligned} \quad (1.10)$$

Equation (1.10) for the group index shows that in order to achieve the maximal n_g we need to optimize the pump intensity, which is such that $s \simeq 0.5$ for homogeneously broadened systems. The exact value depends on the frequency. More importantly, equation (1.10) shows that the group index depends on the product $\alpha_0 T_1$. This suggests using high absorption media and long lived atomic systems in order to achieve the slowest light propagation. However, by increasing α_0 , we increase the propagation losses and for long T_1 , the slow light bandwidth is considerably reduced.

1.1.2 CPO in semiconductors

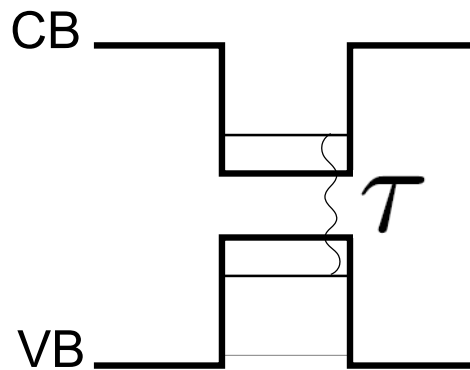
Originally observed in atomic systems, the CPO effect has also been evidenced in semiconductors allowing slow light propagation. The semiconductors have multiple advantages over the atomic systems. The time scale of the population lifetime falls in the range of nanoseconds, which corresponds to GHz bandwidths, much larger than other atomic systems [Bigelow 2003b, Baldit 2005]. These large bandwidths are compatible with the actual optical communication systems. Moreover, semiconductors allow easy on-chip integration with other active semiconductor-based devices.

The first demonstration of CPO-based slow light propagation in a semiconductor was carried out in a multi-quantum-wells (MQWs) sample achieving a group index $n_g = 3.12 \times 10^4$ [Ku 2004]. Since then, other demonstrations have been reported using either the quantum wells or the quantum dots [Chang 2005]. The main results that have been achieved are summarized in table 1.1.

From the theoretical point of view, the semiconductors are considered as two-level-like systems for the CPO effect. Indeed, as shown in figure 1.3, the electron in the conduction band (CB) and the hole in the valence band (VB) play the role of the 2-level atomic system, and the electron-hole recombination time τ is similar to the atomic lifetime T_1 . It is then possible to use the formalism developed in section 1.1.1 to describe or predict the efficiency of the CPO effect in a given semiconductor structure knowing two of its main properties: the unsaturated absorption α_0 and the recombination time τ .

n_g	Length	Delay	Bandwidth	Medium	Temp.	Reference
$3 \cdot 10^4$	202.5 nm	60 ps	2 GHz	15 QWs AlGaAs	10°K	[Ku 2004]
$1.5 \cdot 10^6$	195 nm	1 ns	120 MHz	15 QWs AlGaAs	10°K	[Palinginis 2005a]
565	440 μm	830 ps	100 MHz	QW AlGaAs	Room	[Palinginis 2005b]
10.6	100 μm	2 ps		Bulk InGaAsP	Room	[?]
6	700 μm	7 ps	2 GHz	QDs InGaAs	Room	[Su 2006]

Table 1.1: Previous experiences of CPO in semiconductors.

Figure 1.3: Sketch of the 2 level system in a semiconductor. CB is the conduction band, VB is the valence band and τ is the electron-hole recombination time.

Photonic Crystals

Over the last few decades a wide range of studies have been performed with the objective of controlling light and its interaction with matter at the nanometer scale. A particular interest has come to a point as we try to engineer materials that would allow a light wave to propagate only in a certain direction (waveguides) or to confine it within a region (cavities).

The first approach to this problem was the total internal reflection systems, where light is confined in a dielectric or semiconductor using the refraction index contrast between two materials. An important example of this are the fiber-optics that revolutionized the telecommunications but cavities as microdisks or microspheres also rely on this principle.

An other possible approach is to work with the interferences in a medium with a periodicity in the refractive index. As in solids, where the periodicity of a crystal modifies the conduction properties of electrons by defining allowed and forbidden electronic energy bands, periodic structures of the refractive index at the wavelength scale modify the propagation of light in certain directions for certain frequencies. It is because of this analogy that one calls this kind of structure *photonic crystals*. The first and well known example is the Bragg mirror that is indeed a sort of one dimensional photonic crystal. In our days, we can also fabricate two dimensional or three dimensional photonic crystals allowing light to propagate in a unique direction (waveguides) or confining it to a given region (cavities). In this chapter we make a brief description of these possibilities focusing on the particular structures studied in this thesis the L3 photonic crystal cavity and the W1 photonic crystal waveguide.

2.1 1D photonic crystal

The Bragg mirror is the simplest 1D photonic crystal structure. It consists of a structure with a periodical succession of layers of permittivities ε_1 and ε_2 and period Λ , as shown in figure 2.1. If we consider the case of an electromagnetic wave at a wavelength $\lambda \ll \Lambda$ interacting with the structure then the problem can be explained by geometrical optics (Snell-Descartes Law). If $\Lambda \ll \lambda$ the electromagnetic wave *perceives* an homogeneous permittivity given by the average between ε_1 and ε_2 weighted by the respective thicknesses. It is between these two regimes, when $\Lambda \sim \lambda$, that the periodic structure behaves like a Bragg mirror, i.e. if all the successive reflexions are in phase the wave attenuates rapidly as it penetrates the medium.

The propagation properties in such periodic medium is well described by the dispersion relation $\omega(k)$ where the frequencies are given as a function of the wavevector

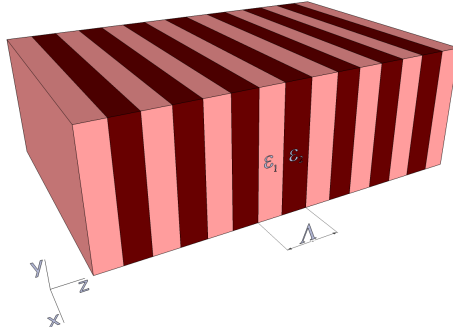


Figure 2.1: Sketch of a structure with a unidimensional periodicity in the permittivity (Bragg mirror).

k . The dispersion relation is obtained starting from the Maxwell equation considering the periodicity of the permittivity $\varepsilon(z) = \varepsilon(z + \Lambda)$. We can decompose the permittivity using a Fourier expansion:

$$\varepsilon(z) = \sum_m \varepsilon_m e^{-iK_m z}$$

where $K = 2\pi/\Lambda$.

The solution of the Maxwell equations for this periodic system are the *Bloch waves*:

$$\begin{aligned} E(z) &= e_m e^{-i(k_z + mK)z} \\ H(z) &= h_m e^{-i(k_z + mK)z} \end{aligned} \quad (2.1)$$

where e_m and h_m are periodical. Note that the wave-vector, $k_z + mK$, of the Bloch mode is invariant under a $\pm K$ transformation. Indeed, in order to fully describe the physics of propagation we can restrict ourselves to the interval $-K/2 < k \leq K/2$: this region in k space is called the Brillouin zone. We also define the *effective index* as $n_{\text{eff}}(\omega) = k_z(\omega)/k_0$ where $k_0 = 2\pi/\lambda$.

Figure 2.2 shows the dispersion relation, called also band diagram, for the case $\varepsilon_1 = \varepsilon_2 = 13$ (a) and for $\varepsilon_1 = 13$ and $\varepsilon_2 = 1$ (b). It is important to note that, for $\varepsilon_1 \neq \varepsilon_2$, there is no propagative solution for $k = K/2$, this is called *band gap* in an analogy with solid state physics. At the band gap the 1D photonic crystal works as a mirror. Bragg mirrors give thus a simple and intuitive example of band gap structures. Nevertheless, the appellation *photonic crystal* is reserved to higher dimensional periodical systems.

2.2 2D photonic crystal

The next step is to go from unidimensional periodic structure to a system with periodicity in two directions and invariant in the third one, such structure is called

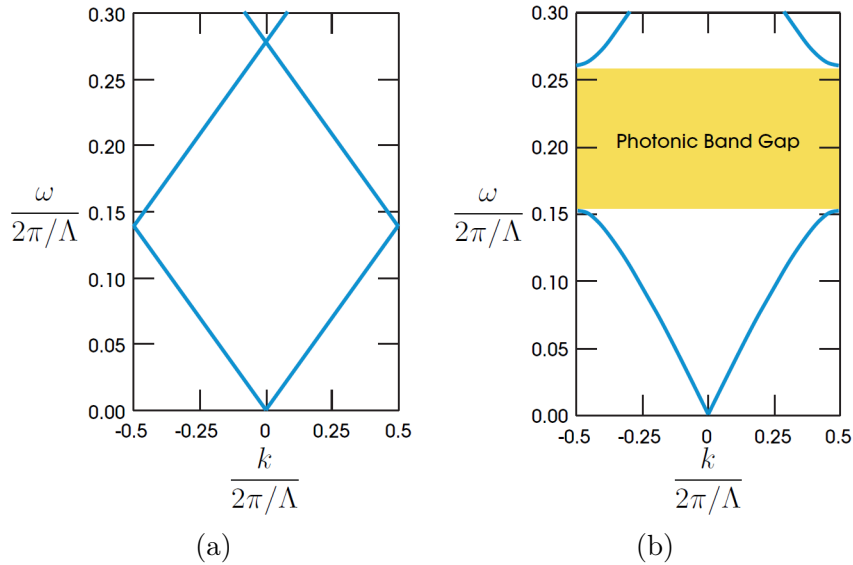


Figure 2.2: Photonic band structure for a propagation perpendicular to the structure for (a) $\varepsilon_1 = \varepsilon_2 = 13$ and (b) $\varepsilon_1 = 13$ and $\varepsilon_2 = 1$ [Joannopoulos 2008].

2D photonic crystal. The most usual geometry is a triangular lattice of holes in a 2D membrane, as shown in figure 2.3.a. Using this geometry we can confine light in the 2 directions of the plane with the help of band gaps. The confinement in the third direction (perpendicular to the plane of symmetry) is achieved by index contrast using total internal reflection. Indeed, usually the slab is sufficiently thin to constitute a single mode waveguide. We consider an index periodicity given by air holes ($n=1$) embedded in a high refractive index material. A key point for 2D photonic crystals is the discrimination between two polarizations of the electromagnetic fields: *transverse-electric* (TE) modes where the magnetic field is normal to the plane and the electric field lies on the plane, and *transverse-magnetic* (TM) modes where the magnetic field is in the plane and the electric field is normal to the latter. The band structure for the TE and TM modes can be completely different, as shown in figure 2.3.b. In particular, it may occur that a photonic bandgap exists for one polarization while no bandgap exists for the other one. Frequency bands for which propagation is forbidden both for TE and TM modes are called total bandgaps. The search for total bandgap was a key issue at the beginning of the engineering of 2D PhC. We will now concentrate in the two devices at the heart of this thesis: 2D PhC cavities and W1 PhC waveguides.

2.3 Photonic crystal cavities

The photonic bandgap can be used to confine light in reduced volumes. This was the key issue in the pioneering work of E. Yablonovitch [Yablonovitch 1987]. The aim being to confine light in a volume reduced to the wavelength in order to control

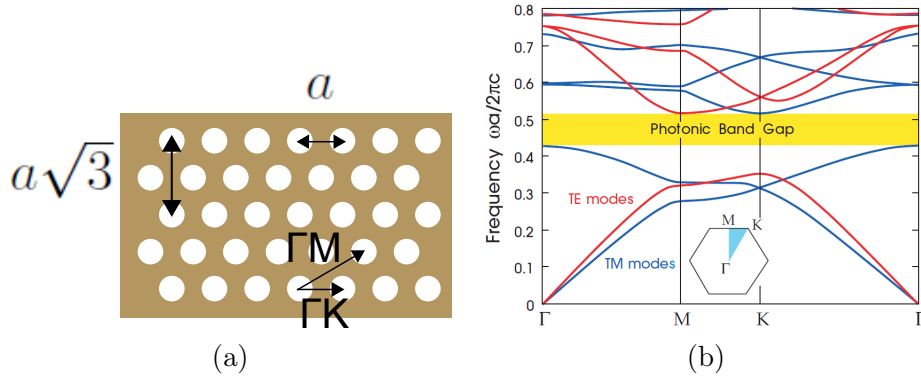


Figure 2.3: (a) 2D Photonic crystal of triangular lattice. The periodicity is given by air holes of radius r in a material with dielectric constant $\epsilon = 13$. (b) Band diagram for the structure in (a). The red lines represent the TE modes while the blue lines the TM modes. The inset shows the Brillouin zone. [Joannopoulos 2008]

the spontaneous emission of a single emitter. Imagine that we include a defect in a 2D PhC for instance by removing some holes in the lattice: if this defect has the appropriate size to support a mode surrounded by the photonic band gap, then the light gets trapped into it. As a result, an optical cavity is achieved. These cavities can have very small volumes and high quality factors (Q), where Q represents the rate of energy loss relative to the stored energy in the cavity. It is given by $Q = \tau\omega/2 = \omega/\Delta\omega$, with τ the photon lifetime inside the cavity, ω the cavity resonance frequency, and $\Delta\omega$ the resonance width.

As mentioned before photonic crystal nanocavities can be formed by removing and/or modifying (i.e. by changing the hole size or the refractive index) one or more holes in an otherwise perfectly periodic lattice. Such a breaking in the periodicity of the lattice, that introduces new energy levels within the photonic band gap, can be achieved for different types of lattice geometries and can have itself different geometries. The most popular nanocavity geometries are defect cavities and double heterostructures.

The simplest defect cavity in a bi-dimensional photonic crystal consists of removing one hole [Painter 1999] in a perfect triangular lattice of holes. This cavity is called H1. However, it typically has quality factors of a few hundreds, which exclude them as good candidates for most nonlinear optical applications. L3 cavities where 3 consecutive holes are missing in a line of holes are nowadays the most emblematic defect cavities since they ensure relative small volume and high Q -factor. Such kind of cavities are sketched in figure 2.4.a (top).

In recent years, a considerable amount of effort has been devoted to improve PhC cavity design in terms of both Q -factors and mode volumes. In particular, it has been shown that given a defect cavity, the quality factor of the structure can be improved by shifting the position of the nearby holes or increasing/decreasing their size. This is the case of the L3 modified cavity in a suspended PhC membrane.

Such cavities are given by three missing holes in a line of a triangular periodic lat-

tice, as shown in figure 2.4.a. Noda et al. [Akahane 2003] have demonstrated that a slight shift of the two holes closing the cavity increases the cavity quality factor by almost one order of magnitude, figure 2.4.b. Sauvan et al. [Sauvan 2004, Sauvan 2005] have given a successful interpretation of this phenomenon. Two elements contribute to the increase of the quality factor of the cavity: the shift of the surrounding holes better adapt the cavity mode profile to the *mirrors*, improving their reflectivity and producing a decrease of the group velocity of the cavity modes. We will come back to this particular point in chapter 3. Thanks to this shift, high quality factors (Q), e.g. $Q \sim 10^4$ in GaAs and $Q \sim 45000$ in Si, are achieved. In this thesis, we have implemented this kind of cavities in InP suspended membranes (chapter 4).

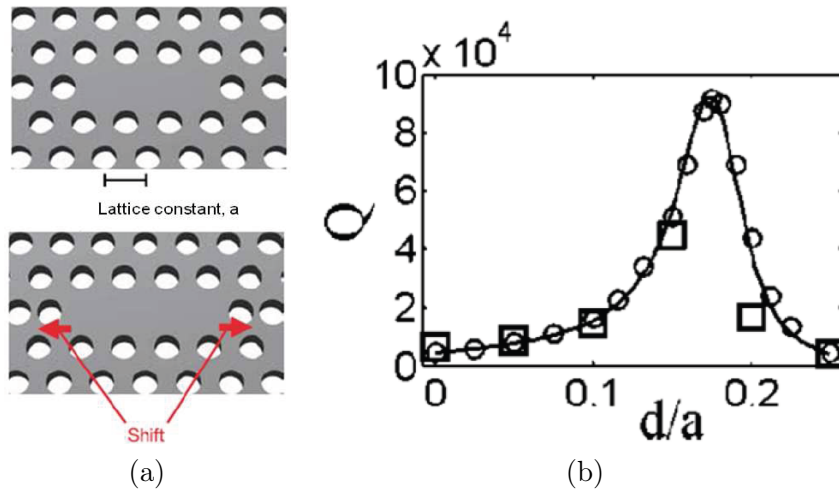


Figure 2.4: (a) Sketch of a L3 cavity with a lattice constant a , where the two holes closing the cavity are shifted away a distance d . Image from [Akahane 2003]. (b) Quality factor Q of the L3 cavity as a function of the holes shift, d . Squares correspond to the experimental results in [Akahane 2003] while the line and the circles correspond to the numerical results from [Sauvan 2005]. Image from [Sauvan 2005].

2.4 Photonic crystal waveguides

As we have seen in section 2.3, a punctual defect obtained by removing one or several holes in a region induced a cavity; a linear defect created by removing a row of holes generates a waveguide. Light propagates through this defect, confined by total internal reflection in the vertical direction and *Bragg like reflection*, due to the photonic crystal band gap, in the lateral direction. This kind of photonic crystal waveguides where there is just one line of holes missing are usually called *W1 waveguides*. Figure 2.5.a shows a sketch a W1 waveguide. Variations can be made to build different kinds of waveguides following the same principle.

Figure 2.5.b shows the dispersion curve of the mode propagation in a W1 photonic crystal waveguide with a refractive index $n = 3.31$ (corresponding to InP), a

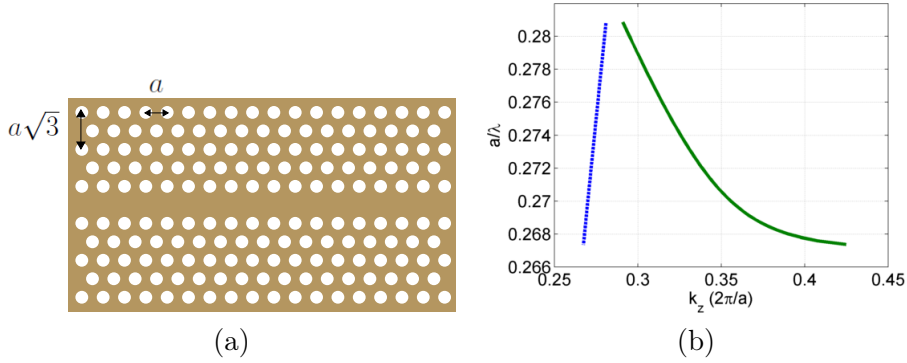


Figure 2.5: (a) Sketch of a 2D PhC W1 waveguide. (b) Dashed blue line: light line, straight green line: Dispersion curve of a W1 waveguide mode with: $a = 420$ nm, $r = 125$ nm, thickness $e = 265$ nm and $n = 3.31$.

triangular lattice period $a = 420$ nm, a hole radius $r = 125$ nm and a membrane thickness $e = 265$ nm. W1 photonic crystal waveguides can be either mono or multimode, in our case we have chosen to work with a small thickness which ensures a monomode operation.

Equation (2) in the introduction shows that the group velocity is the derivative of the frequency with respect of the wavevector, i.e. the slope of the dispersion curve. Figure 2.5.b shows that as we approach the limit of the Brillouin zone ($k_z = 0.42 (2\pi)/a$) the group velocity becomes smaller and thus the corresponding group index n_g is large. The nature of this slowing down is the backscattering where light is coherently backscattered at each unit cell of the crystal. If the forward propagating and the backscattered light match in phase and amplitude (as they do at the Brillouin zone boundary for $k = \pi/a$), a standing wave results, which can also be understood as a slow mode with zero group velocity. Another mean to obtain slow light in PhC WGs is the omnidirectional reflection states. Because of the fact that photonic crystal waveguides do not have a cut-off angle, light propagating at any angle is reflected at the *borders* of the waveguide. We find then a zigzag movement that becomes stiffer as we approach the Γ -point, i.e. $k \simeq 0$, obtaining slow modes and forming a standing wave for $k = 0$. The nature of slow light in PhC WGs is fully discussed by T. F. Krauss [Krauss 2007]. In this thesis I will focus on the backscattering phenomenon close to $k = \pi/a$.

The first experimental demonstration of slow light in a W1 photonic crystal waveguides was achieved by Prof. Notomi's group in 2001 [Notomi 2001]. Since this pioneering work several articles have tackled experimentally the slow modes on W1 waveguides. Table 2.1 shows some of the results of slow light in photonic crystal waveguides. A review of these results was published by Prof. Baba [Baba 2008].

Group index (n_g)	Length (μm)	Delay (ps)	Bandwidth (nm)	Reference
40-60	250	40	10-12	[Kawasaki 2007]
25-60	390	40	3-12	[Hamachi 2009]
34	500	56	11	[Frandsen 2006]
300	250	250	20	[Vlasov 2005]

Table 2.1: Previous experiences of Slow light in W1 photonic crystal waveguides.

Part II

Slow light in photonic crystal cavities

Reducing cavity mode volumes and increasing the cavity lifetimes is a crucial trend in photonics for integration of various optical functions and as well for fundamental studies [Vahala 2003, Matsko 2006, Ilchenko 2006]. The narrow resonance and the long photon lifetime of such devices can be used in optical and microwave filtering applications [Strekalov 2003, Oraevsky 2001] or for optical buffer miniaturization [Tanabe 2006]. Moreover, such properties may result in suitable conditions to enhance light-matter interaction with applications in nonlinear optics [Yanik 2003, Shinya 2008, Chembo 2010], biosensing [Arnold 2009], microwave filtering [Strekalov 2003], pulse storage [Tanabe 2006, Xu 2007, Dumeige 2009a], quantum information and quantum electrodynamics [Aoki 2009, Rivoire 2011], potentially in integrated platforms.

Intrinsic limits for the Q -factor in a microcavity are given either by its radiative losses due to imperfect light confinement or by the residual absorption of the constituting material. Therefore, the manufacturing of high- Q resonators requires high purity materials [Savchenkov 2004], complex technological processes to reduce fabrication imperfections [Takahashi 2007] and careful design to avoid radiative losses [Akahane 2003, Lu 2010]. One can note that it is possible to compensate for optical losses by using a gain material within the microcavity [Minin 2004, Peng 2006, Dumeige 2008]. A rigorous theoretical analysis by C. Sauvan *et al.* [Sauvan 2005] has shown that among the physical mechanisms involved in the Q -factor enhancement via the geometrical engineering of the nanocavity neighborhood is the increase of the the group index n_g of the nanocavity mode. By slightly changing the size and position of few holes surrounding the cavity, the cavity mode group index is indeed increased.

Another way to increase the Q -factor consists in inserting a highly dispersive material inside the microcavity [Soljačić 2005b]. This technique has already been experimentally demonstrated in atomic systems embedded in macroscopic ring cavities using coherent non-linear effects such as coherent population trapping or electromagnetically induced transparency (EIT) [Müller 1997, Lukin 1998, Wang 2000, Goorskey 2002, Yang 2004, Lauprêtre 2011]. In those configurations, a *powerful* pump beam induces a steep dispersion at the probe frequency, tuned to the cavity resonance; the resulting increase of the group index strongly decrease the cavity linewidth. In this context, it has also been shown that a nonlinear susceptibility at the probe frequency can enhance the Q -factor of the cavity [Wu 2007]. The Q -factor of a solid state whispering gallery mode microresonator has been recently greatly improved using the dispersion induced by optomechanical effects [Weis 2010].

In this part slow light via non-linear interactions in photonic crystal nanocavities is studied. It is theoretically and experimentally demonstrated that slow light enables to have a small-size and ultra-high Q -factor cavity, regardless of the technological and design issues. For the experimental demonstration we use L3 2D Photonic Crystal (PhC). The theoretical study of coherent nonlinear interaction in nanocavities is developed in chapter 3. Chapter 4 presents the experimental setup and the experimental results. Finally, the experimental results and the theoretical predictions are compared.

Theoretical Model

Contents

3.1	CPO effect in a microcavity: Basic approach	26
3.2	CPO and nonlinear effects in a Fabry-Perot cavity	28
3.3	Model for CPO in a semiconductor nonlinear microcavity .	33
3.4	Analytical results	35
3.4.1	First order calculations	35
3.4.2	Asymptotic behavior	36
3.5	Numerical results	40
3.5.1	Absorptive nonlinearity	40
3.5.2	Dispersive nonlinearity	45
3.6	Conclusion	45

We have discussed in the general introduction of chapters 1 and 2 the different ways to achieve slow light and more generally optical delays. We will concentrate here on those associated to nonlinear interactions in a cavity. More precisely we will consider different theoretical approaches of increasing complexity. Firstly, we describe the situation of a cavity containing a 2-level system (TLS) in which CPO effect is induced (section 3.1) [Dumeige 2012]. Second, we consider a simple Fabry-Perot cavity in which CPO coexists with a nonlinear refractive index (section 3.2). These simplified models allow to gain a first intuition on the physical situation that will certainly exist in an active semiconductor nanocavity. A more sophisticated approach based on coupled mode theory (CMT) is presented in section 3.3 [Dumeige 2012]. The theoretical model is based on the coupled equations describing the evolution of the mode amplitude a in the cavity and the evolution of the carrier density N in the quantum wells. Finally, analytical (section 3.4) and numerical (section 3.5) results are presented.

Table 3.1 gives a summary of the different approaches, their advantages and limitations.

	CPO in a microcavity	Fabry-Perot cavity	Coupled mode theory	
			Analytical	Numerical
Advantage	Simple approach	Separate contributions	Full model	Validation
Analytical expressions	YES	YES	NO	NO
CPO	YES	YES	YES	YES
Nonlinear	NO	YES	YES	YES

Table 3.1: Characteristics of the different models.

3.1 CPO effect in a microcavity: Basic approach

In this approach, the 2D photonic crystal nanocavity containing active quantum wells used for the experimental demonstrations in this thesis, is modeled by a simple resonator containing two-level atomic like systems (TLSs) simulating the active quantum wells. As shown in figure 3.1, the resonator is characterized by its lifetime τ given by

$$\frac{1}{\tau} = \frac{2}{\tau_e} + \frac{1}{\tau_{rad}} + \frac{1}{\tau_a}, \quad (3.1)$$

where τ_{rad} is cavity lifetime limited by the radiation losses, τ_a is the cavity lifetime related to the absorption α of the atomic-like systems in the resonator, given by

$$\frac{1}{\tau_a} = \frac{c\alpha}{2n_0}, \quad (3.2)$$

where n_0 is the refractive index of the material constituting the cavity. τ_e characterizes the evanescent coupling of an electromagnetic field into the resonator through, for example, an optical fiber. To induce the CPO effect in the TLSs, a pump field at frequency ω_p with intensity I shines the cavity whereas a weaker signal field at frequency $\omega_p + \delta$ is coupled into the cavity through the fiber. In order to avoid non-linear dispersion, and have only the bare CPO effect, the pump field is not resonant. We will come latter to the general case.

As it has been explained in chapter 1, for a pump-probe detuning $\delta < 1/T_1$, where T_1 is the population lifetime of the TLS, the CPO effect generates a strong dispersion on the probe beam characterized by a group index n_g calculated from a density matrix approach and given by [Boyd 1981, Bigelow 2003a]

$$n_g = \frac{\alpha_0 c T_1}{2} \frac{I}{(1+I)^3} \quad (3.3)$$

where $I = I_0/I_{sat}$ with I_0 and I_{sat} being respectively the pump and saturation intensities. In the limit of $T_2 \ll T_1$, where T_2 is the dephasing time of the TLSs and in the limit where $\delta T_1 \ll 1$. The absorption is given by:

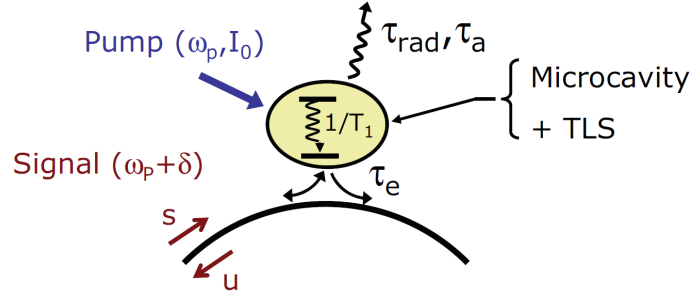


Figure 3.1: Microcavity containing a two level system. The pump (frequency ω_P) is non-resonantly coupled to the cavity. s (frequency $\omega_s = \omega_P + \delta$) is the input probe field. The cavity mode is coupled to the reflected field u via evanescent waves with a characteristic lifetime τ_e .

$$\alpha = \frac{\alpha_0}{(1 + I)^2}, \quad (3.4)$$

where α_0 is the unsaturated absorption of the TLS. If $n_g \gg n_0$, the quality factor of the cavity experienced by the probe beam is thus given by [Müller 1997, Soljačić 2005b, Sauvan 2005, Dumeige 2009b]:

$$Q = \frac{n_g \omega_0 \tau}{n_0 2}, \quad (3.5)$$

which can also be written using equations (3.1-3.5)

$$Q = \frac{\omega_0 T_1 I}{2(1 + I) \left[1 + \tau_{a0} \left(\frac{2}{\tau_e} + \frac{1}{\tau_{rad}} \right) (1 + I)^2 \right]}, \quad (3.6)$$

where

$$\frac{1}{\tau_{a0}} = \frac{c\alpha_0}{2n_0}. \quad (3.7)$$

Depending of the different lifetimes of the system, two scenarios are considered.

Strong unsaturated absorption: in this first limit, we suppose that the absorption α_0 in the cavity is strong. In this case $\tau_e, \tau_{rad} \gg \tau_{a0}$, and the overall Q -factor can be approximated by:

$$Q = \frac{\omega_0 T_1 I}{2(1 + I)}. \quad (3.8)$$

This expression shows that the new lifetime of the cavity is $T_1 I_0 / (1 + I_0)$. Choosing $T_1 \gg \tau_{rad}$ the population oscillation greatly increases the cavity lifetime which originally could only reach the maximum value τ_{rad} when all the other optical loss sources are negligible. The only drawback of this case is that the reflected power given by:

$$\left| \frac{u}{s} \right|^2 = \left(\frac{2\tau_{a0}}{\tau_e} \right)^2 (1 + I)^4 \quad (3.9)$$

can be very weak as $\tau_{a0} \ll \tau_e$.

Weak unsaturated absorption: in this second situation we suppose that the absorption in the cavity is very weak. As a consequence $\tau_e, \tau_{rad} \ll \tau_{a0}$. The Q -factor can now be written as

$$Q = \frac{T_1}{\tau_{a0}} \frac{I_0}{(1 + I_0)^3} Q_0, \quad (3.10)$$

where the Q -factor of the cold cavity $Q_0 = \omega_0 \tau_0 / 2$ is deduced from the photon lifetime of the cold cavity

$$\frac{1}{\tau_0} = \frac{2}{\tau_e} + \frac{1}{\tau_{rad}} + \frac{1}{\tau_{a0}}. \quad (3.11)$$

Considering the hypothesis, we get

$$\frac{1}{\tau_0} \approx \frac{2}{\tau_e} + \frac{1}{\tau_{rad}}. \quad (3.12)$$

The main limitation of this approach is that the Q -factor is proportional to T_1/τ_{a0} which is limited since we have assumed a high value of τ_{a0} . This leads to a moderate value of CPO enhanced Q -factor.

As a partial conclusion, we point out that the photon lifetime of a microcavity containing a two level system where CPO occurs can be strongly increased. The cavity lifetime is then basically limited by the population lifetime T_1 . However, as it has been pointed out in chapter 1 unlike other coherent effect based schemes where absorption is completely canceled, in the CPO approach, the residual unsaturated absorption limits the reflected power from the cavity. Our experimental situation is closer to the second case where the unsaturated absorption is $\alpha_0 = 58 \text{ cm}^{-1}$, which in equation 3.3 can give a maximum $n_g = 30$, which can achieve an enhancement of 3 of the quality factor. However, it will be shown in next sections that the nonlinear properties of the cavity strongly contribute in the enhancement of the quality factor.

3.2 CPO and nonlinear effects in a Fabry-Perot cavity

In this section we discuss a simple model consisting of an optical cavity containing a material with both dispersive and nonlinear effects in order to gain intuition of the physical behavior when both CPO and nonlinear dispersion are present in our nanocavity. In this model, we consider a Fabry-Perot cavity of length L , with finesse \mathcal{F} , and partially filled with a medium with a group index n_g due to the CPO effect and a negative nonlinear index n_2 . The cavity is simultaneously injected with a strong pump beam $E_P = E_{P,0} e^{-i\omega_P t}$ and a weak signal (probe) $E_S = E_{S,0} e^{-i\omega_S t}$.

The respective wavevectors are: $k_{P,T} = k_P + \Delta k^{(NL)}$ for the pump and $k_{S,T} = k_S + \Delta k^{(NL)}$ for the probe, where $\Delta k^{(NL)}$ is the nonlinear term associated with the nonlinear index n_2 . The nonlinear term can be written, considering a perturbative approach, as:

$$\Delta k^{(NL)} = \frac{\omega}{v_g} \Gamma \frac{\Delta n^{(NL)}}{n} = -\frac{\omega}{v_g} \Gamma \mathcal{A} \frac{n_2 |E|^2}{n} \quad (3.13)$$

where Γ is the normalized overlap of the unperturbed mode with the perturbation, v_g represents the group velocity associated with the dispersion due to the periodic structuration of the photonic crystal, and \mathcal{A} is given

$$\mathcal{A} = \frac{cn\varepsilon_0}{2},$$

such that $I = \mathcal{A}|E|^2$.

A detailed explanation of the origin of this equation will be given ahead, in chapter 5 (see equation (5.25)).

We can then rewrite the pump and probe wavevectors as:

$$k_{P,T} = k_P - \mathcal{A}' \frac{n_2 |E|^2}{L} \quad (3.14)$$

$$k_{S,T} = k_S - \mathcal{A}' \frac{n_2 |E|^2}{L} \quad (3.15)$$

where for simplicity we defined $\mathcal{A}' = \mathcal{A} \frac{\omega \Gamma L}{v_g n}$.

In order to calculate the delay due to the CPO effect and to the nonlinear dispersion, we start by the determination of the transmitted probe field. This is done by considering the conservation of the tangential electric field at the boundaries of the cavity, i.e. at $z = 0$ and at $z = L$, as shown in figure 3.2. We first suppose that the two mirrors of the cavity are identical having the same amplitude transmission t and reflection r .

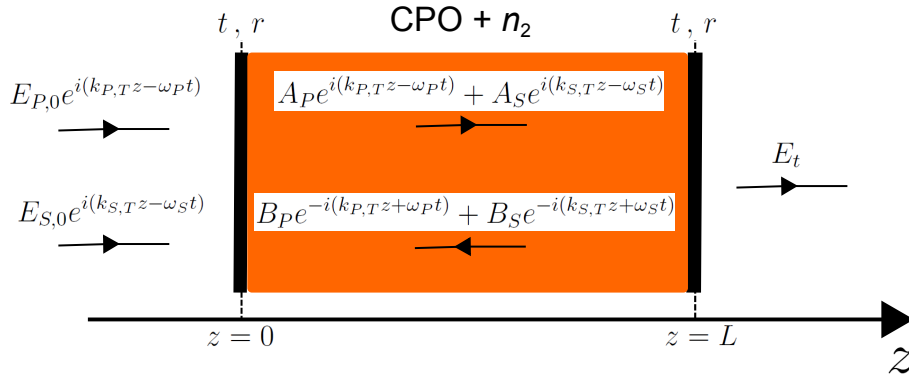


Figure 3.2: Fabry-Perot system studied.

At $z = 0$, we obtain:

$$\begin{aligned}
& A_P e^{-i\omega_P t} + A_S e^{-i\omega_S t} = \\
& t (E_{P,0} e^{-i\omega_P t} + E_{S,0} e^{-i\omega_S t}) + r (B_P e^{-i\omega_P t} + B_S e^{-i\omega_S t})
\end{aligned} \tag{3.16}$$

multiplying on both sides by $e^{i\omega_P t}$ and integrating between $-\infty$ and ∞ only the terms oscillating at $-\omega_P t$ are non null, giving:

$$B_P = \frac{A_P - tE_{P,0}}{r}. \tag{3.17}$$

doing the same thing but multiplying by $e^{i\omega_S t}$ we obtain the equivalent probe condition:

$$B_S = \frac{A_S - tE_{S,0}}{r} \tag{3.18}$$

Evaluating at $z = L$ we can write the fields as:

$$\begin{aligned}
& B_P e^{-i(k_P L + \omega_P t)} + B_S e^{-i(k_S L + \omega_S t)} = \\
& r (A_P e^{i(k_P L - \omega_P t)} + A_S e^{i(k_S L - \omega_S t)})
\end{aligned} \tag{3.19}$$

Now we replace B_P and B_S by the expressions given in equations (3.17) and (3.18), the expressions of the wavevectors (3.14) and (3.15) and assume that the nonlinear term is small.

$$\begin{aligned}
& \frac{A_P - tE_{P,0}}{r} e^{-i(k_P L + \omega_P t)} (1 + i\mathcal{A}' n_2 |E|^2) + \frac{A_S - tE_{S,0}}{r} e^{-i(k_S L + \omega_S t)} (1 + i\mathcal{A}' n_2 |E|^2) = \\
& r [A_P e^{i(k_P L - \omega_P t)} (1 - i\mathcal{A}' n_2 |E|^2) + A_S e^{i(k_S L - \omega_S t)} (1 - i\mathcal{A}' n_2 |E|^2)]
\end{aligned} \tag{3.20}$$

We can write the field $|E|^2$ as:

$$|E|^2 = |A_P e^{i(k_P L - \omega_P t)} + A_S e^{i(k_S L - \omega_S t)} + B_P e^{-i(k_P L + \omega_P t)} + B_S e^{-i(k_S L + \omega_S t)}|^2$$

and assuming the pump and probe condition $|A_S|^2 \ll |A_P|^2$, $|B| \sim |A|/r$ and disregarding the terms oscillating at $2k_S L$ or $2k_P$:

$$|E|^2 \simeq |A_P|^2 \left(1 + \frac{1}{r^2} \right) + A_P^* A_S e^{i(\omega_P - \omega_S)t} \left(e^{i(k_S - k_P)L} + \frac{e^{i(k_P - k_S)L}}{r^2} \right) + c.c.$$

we introduce this expression in equation (3.20). Multiplying on both sides by $e^{i\omega_S t}$ and integrating between $-\infty$ and ∞ only the terms oscillating at $-\omega_S t$ are non null, giving:

$$\begin{aligned}
& i \frac{A_P - tE_{P,0}}{r} e^{-ik_P L} \mathcal{A}' n_2 A_P^* A_S \left(e^{i(k_S - k_P)L} + \frac{e^{i(k_P - k_S)L}}{r^2} \right) \\
& + i r A_P e^{ik_P L} \mathcal{A}' n_2 A_P^* A_S \left(e^{i(k_S - k_P)L} + \frac{e^{i(k_P - k_S)L}}{r^2} \right) \\
& + \frac{A_S - tE_{S,0}}{r} e^{-ik_S L} \left[1 + i \mathcal{A}' n_2 |A_P|^2 \left(1 + \frac{1}{r^2} \right) \right] \\
& - r A_S e^{ik_S L} \left[1 - i \mathcal{A}' n_2 |A_P|^2 \left(1 + \frac{1}{r^2} \right) \right] = 0
\end{aligned} \tag{3.21}$$

We can finally write the probe field A_S as:

$$A_S = \frac{tE_{S,0}}{1 - e^{2ik_S L} [r^2 - i \mathcal{A}' n_2 |A_P|^2 (e^{-2ik_P L} + 5r^2)] + i \mathcal{A}' n_2 |A_P|^2 \left(\frac{1}{r^2} + e^{2ik_P L} \right)} \tag{3.22}$$

where we disregarded the terms where the product of transmission t , nonlinear index n_2 and/or probe field amplitude A_S gives a third order contribution.

We now introduce the wavevector for the probe:

$$k_S = \frac{\omega_S}{c} n_{\text{eff}}(\omega_S) + \frac{\omega_S}{v_g} \Gamma \frac{\Delta n^{(CPO)}}{n}. \tag{3.23}$$

We write the refraction index by separating the constant term from the frequency dependent one and approximate to:

$$n \simeq n_0 + \frac{dn}{d\omega} \delta\omega. \tag{3.24}$$

From the expression of the group index, we can write the derivative as:

$$\frac{dn}{d\omega} = \frac{n_g - n}{\omega}$$

then

$$\Delta n^{(CPO)} = \frac{\delta\omega}{\omega} \frac{n_g^{CPO} - n}{n}$$

using this expression we develop the probe wavevector k_S close to the linear resonance:

$$k_S \simeq \frac{m\pi}{L} + \frac{\delta\omega}{v_g} \left(1 + \Gamma \frac{n_g^{CPO} - n}{n} \right) \tag{3.25}$$

and:

$$e^{2ik_S L} = e^{2i \frac{\delta\omega}{v_g} \left(1 + \Gamma \frac{n_g^{CPO} - n}{n} \right)} \tag{3.26}$$

where $\delta\omega = \omega_S - \omega_0$ with ω_S being the probe frequency and ω_0 the cavity linear resonance frequency. We further develop equation (3.26) at second degree of Taylor expansion. We indeed need the second order to well describe the perturbations.

$$e^{2iksL} \simeq 1 + 2i \frac{\delta\omega}{v_g} \left(1 + \Gamma \frac{n_g^{CPO} - n}{n} \right) + \frac{1}{2} \left[2i \frac{\delta\omega}{v_g} \left(1 + \Gamma \frac{n_g^{CPO} - n}{n} \right) \right]^2 \quad (3.27)$$

Using equation (3.27) in (3.22) we obtain:

$$A_S = \frac{tE_{S,0}}{1 - \left\{ 1 + 2i \frac{\delta\omega}{v_g} \left(1 + \Gamma \frac{n_g^{CPO} - n}{n} \right) + \frac{1}{2} \left[2i \frac{\delta\omega}{v_g} \left(1 + \Gamma \frac{n_g^{CPO} - n}{n} \right) \right]^2 \right\} \times [r^2 - i\mathcal{A}'n_2|A_P|^2 (e^{-2ik_P L} + 5r^2)] + i\mathcal{A}'n_2|A_P|^2 \left(\frac{1}{r^2} + e^{2ik_P L} \right)} \quad (3.28)$$

From this equation we study numerically which terms contribute and which terms can be neglected, obtaining:

$$A_S \simeq \frac{tE_{S,0}}{1 - r^2 - f(\delta\omega) - 2ri \frac{\delta\omega^{(NL)}L}{v_g} \left(1 + \Gamma \frac{n_g^{CPO} - n}{n} \right)} \quad (3.29)$$

where $\delta\omega^{(NL)} = \omega_S - \omega_0^{(NL)}$,

$$f(\delta\omega) \simeq 2r^2 \frac{\delta\omega L}{v_g} \left(1 + \Gamma \frac{n_g^{CPO} - n}{n} \right) \left[6\mathcal{A}'n_2|A_P|^2 - \frac{\delta\omega L}{v_g} \left(1 + \Gamma \frac{n_g^{CPO} - n}{n} \right) \right],$$

and

$$\omega_0^{(NL)} \simeq \omega_0 + \frac{v_g}{L} \frac{4\mathcal{A}'n_2|A_P|^2}{1 + \Gamma \frac{n_g^{CPO} - n}{n}}$$

From equation (3.29) we can write the group phase:

$$\phi_g \simeq \arctan \frac{y\delta\omega^{(NL)}}{1 - r^2 - f(\delta\omega)} \quad (3.30)$$

where we defined $y \equiv \frac{2r^2L}{v_g} \left(1 + \Gamma \frac{n_g^{CPO} - n}{n} \right)$.

Finally, from equation (3.30) we can calculate the final group delay in the cavity as $\tau_g = \frac{d\phi_g}{d\omega_S}$:

$$\tau_g \simeq \frac{2\mathcal{F}Ln}{\pi c} \left(1 + \Gamma \frac{n_g^{CPO} - n}{n} \right) \left[1 + \Gamma n_2 \kappa \Delta\omega \left(1 + \Gamma \frac{n_g^{CPO} - n}{n} \right) \right] \quad (3.31)$$

where \mathcal{F} is the finesse of the cavity $\mathcal{F} = \frac{\pi|r|}{1-|r|^2}$, we assumed $v_g = \frac{c}{n}$ and defined $\Delta\omega \equiv \omega_S^{(NL)} - \omega_0$ and $\kappa \equiv \frac{2\varepsilon_0\omega_P \mathcal{F} n^2 L^2}{\pi c}$.

This expression shows that the total group delay has three contributions: the passive cavity delay ($\sim 2\mathcal{F}Ln/(\pi c)$), the CPO effect given by the group index n_g^{CPO} , and the nonlinear term proportional to n_2 . Notice that the latter vanishes close to the resonance frequency and it is maximum near the maximum slope of $|A_P|^2$ at the high frequency side.

This perturbative approach clearly shows that in the presence of a nonlinear refractive index the overall delay results from the contribution of both the change of the group index resulting from the CPO effect and the nonlinear phase due to the nonlinear refractive index.

3.3 Model for CPO in a semiconductor nonlinear microcavity

In order to fully take into account the two contributions highlighted in section 3.2, we consider here the case where the pump and probe fields, necessary for the CPO effect, are in resonance with the cavity. In this situation as the pump amplitude is high in the cavity, the nonlinear effect associated with the quantum wells is not negligible anymore. The coupled mode theory is very well suited to describe this nonlinear behavior of the cavity. Basically two equations are considered in the CMT model. The first one describes the evolution of the field in the cavity and the second concerns the evolution of the electrons, i.e. the carriers density in the active quantum wells.

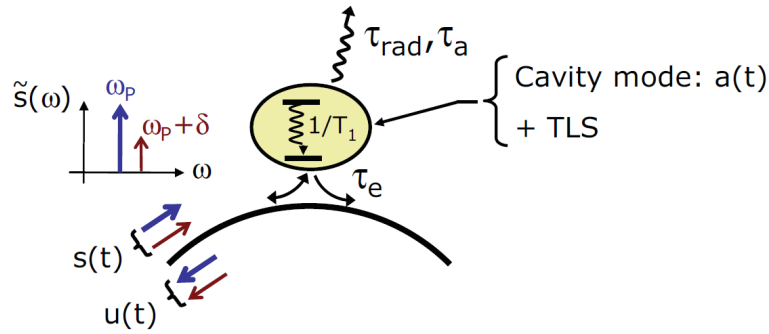


Figure 3.3: Nonlinear microcavity and its access line. s is the input field consisting of a pump and a signal which carrier frequencies are respectively ω_P and $\omega_s = \omega_P + \delta$ ($\tilde{s}(\omega)$ represents the input signal spectrum). The cavity mode a is coupled to s and to the reflected field u via evanescent waves with a characteristic lifetime τ_e .

The mode amplitude in the cavity $a(t)$ is described by a simple harmonic oscillator model [Haus 1984]

$$\frac{da}{dt} = \left[j(\omega_0 + \Delta\omega) - \frac{1}{\tau} \right] a(t) + \sqrt{\frac{2}{\tau_e}} s(t) \quad (3.32)$$

where $s(t)$ is the input field. Note that $|a(t)|^2$ is the energy stored inside the cavity

and the power of the input signal is given by $|s(t)|^2$. We assume that the absorption linearly depends on the carrier density N in the quantum wells through:

$$\alpha = \alpha_0 \cdot \left(1 - \frac{N}{N_t}\right) \quad (3.33)$$

where N_t is the carrier density at transparency. The refractive index variations due to the photocreated carriers induce a frequency shift $\Delta\omega$ of the cavity resonance. The absorption and the index variations are related through the Henry's linewidth enhancement factor α_H [Henry 1982]. With these definitions, ω_0 is the resonance frequency of the cavity at transparency ($N = N_t$). The frequency shift due to carrier density variations is [Spinelli 1998, Yacomotti 2006a, Yacomotti 2006b, Brunstein 2011]

$$\Delta\omega = \frac{\alpha_H}{\tau_{a0}} \cdot \left(\frac{N}{N_t} - 1\right). \quad (3.34)$$

The output field $u(t)$ is obtained from the cavity mode amplitude expression

$$u(t) = \sqrt{\frac{2}{\tau_e}} a(t). \quad (3.35)$$

Considering the time domain slowly varying envelope approximation, the definition of the pump angular frequency ω_P and the expression of the field amplitudes

$$a(t) = A(t)e^{j\omega_P t} \quad (3.36a)$$

$$s(t) = S(t)e^{j\omega_P t} \quad (3.36b)$$

$$u(t) = U(t)e^{j\omega_P t} \quad (3.36c)$$

Equations (3.32) can be recast as:

$$\frac{dA}{dt} = \left[j\Delta - \frac{1}{\tau_0} + \frac{N}{N_t\tau_{a0}} (1 + j\alpha_H) \right] A(t) + \sqrt{\frac{2}{\tau_e}} S(t) \quad (3.37)$$

where Δ is the detuning between the pump frequency and the cold cavity resonance frequency:

$$\Delta = \omega_0 - \frac{\alpha_H}{\tau_{a0}} - \omega_P. \quad (3.38)$$

The carrier density is simultaneously obtained by solving the differential equation [Kapon 1999, Raineri 2009]

$$\frac{dN}{dt} = -\frac{N(t)}{T_1} - \frac{|A(t)|^2}{T_1 |a_{sat}|^2} [N(t) - N_t] \quad (3.39)$$

where $|a_{sat}|^2$ is the saturation energy and T_1 the carrier lifetime. This simple model could also be applied to a atomic two level system [Piredda 2007], in this case the Henry's factor α_H would be replaced by the detuning between the atomic resonance frequency and the pump frequency.

3.4 Analytical results

3.4.1 First order calculations

An input field consisting of a strong pump s_0 and a weak probe signal s_1 (with $|s_1| \ll |s_0|$) slightly detuned from the pump frequency is considered

$$S(t) = s_0 + s_1 e^{j\delta t}. \quad (3.40)$$

The cavity mode and the carrier density can be expanded in a similar way

$$A(t) = a_0 + a_1 e^{j\delta t} + a_{-1} e^{-j\delta t} \quad (3.41a)$$

$$U(t) = u_0 + u_1 e^{j\delta t} + u_{-1} e^{-j\delta t} \quad (3.41b)$$

$$N(t) = N_0 + N_1 e^{j\delta t} + N_{-1} e^{-j\delta t}. \quad (3.41c)$$

Due to the nonlinear term in equation (3.39) the frequency component in $-\delta$ for the cavity mode, the output field and the carrier density must be taken into account. The three following equalities are obtained by combining the last expressions with equation (3.37) and identifying the zero and first order terms

$$0 = \left(j\Delta - \frac{1}{\tau_0} \right) a_0 + \frac{N_0(1 + j\alpha_H)}{N_t \tau_{a0}} a_0 + \sqrt{\frac{2}{\tau_e}} s_0 \quad (3.42a)$$

$$j\delta a_1 = \left(j\Delta - \frac{1}{\tau_0} \right) a_1 + \frac{1 + j\alpha_H}{N_t \tau_{a0}} (N_0 a_1 + N_1 a_0) + \sqrt{\frac{2}{\tau_e}} s_1 \quad (3.42b)$$

$$-j\delta a_{-1} = \left(j\Delta - \frac{1}{\tau_0} \right) a_{-1} + \frac{1 + j\alpha_H}{N_t \tau_{a0}} (N_0 a_{-1} + N_{-1} a_0) \quad (3.42c)$$

The same operation can be done using equation (3.39), then

$$0 = -\frac{N_0}{T_1} - \frac{|a_0|^2}{T_1 |a_{sat}|^2} (N_0 - N_t) \quad (3.43a)$$

$$j\delta N_1 = -\frac{N_1}{T_1} - \frac{(N_0 - N_t)(a_0 a_{-1}^* + a_1 a_0^*) + N_1 |a_0|^2}{T_1 |a_{sat}|^2} \quad (3.43b)$$

$$-j\delta N_{-1} = -\frac{N_{-1}}{T_1} - \frac{(N_0 - N_t)(a_0 a_1^* + a_{-1} a_0^*) + N_{-1} |a_0|^2}{T_1 |a_{sat}|^2}. \quad (3.43c)$$

Equation (3.43a) gives the relation between the normalized intracavity pump energy $x = |a_0/a_{sat}|^2$ and the static carrier density N_0 ,

$$\frac{N_0}{N_t} = \frac{x}{1 + x}. \quad (3.44)$$

For convenience, $y = N_0/N_t$ is introduced. Combining equation (3.44) and equation 3.42a a relation between x and the pump input power $P_{in} = |s_0|^2$ is obtained:

$$\frac{P_{in}}{P_0} = \frac{x\tau_0\tau_e}{2} \left| j\Delta - \frac{1}{\tau_0} + \frac{x}{1+x} \cdot \frac{1+j\alpha_H}{\tau_{a0}} \right|^2, \quad (3.45)$$

where $P_0 = |a_{sat}|^2/\tau_0$. Basically, this relation gives the nonlinear pump transmission. Under some conditions, the equation $P_{in} = f(x)$ can have two solutions giving a bistable behavior to the cavity. Since $N(t)$ is real we have $N_1 = N_{-1}^*$, thus using equation (3.42c):

$$a_{-1}^*(\delta) = a_0^* \frac{N_1(\delta)}{N_t} H(\delta) \quad (3.46)$$

where

$$H(\delta) = \frac{1 - j\alpha_H}{\eta + j(\delta + \Delta)\tau_{a0} - y(1 - j\alpha_H)} \quad (3.47)$$

and $\eta = \tau_{a0}/\tau_0$. Using equation (3.46), equation (3.43b) can be rewritten:

$$\frac{N_1}{N_t} = \frac{a_1 a_0^*}{|a_{sat}|^2} F(\delta) \quad (3.48)$$

where $F(\delta)$ is defined as:

$$F(\delta) = \frac{1}{1 + x + j\delta T_1 - yH(\delta)}. \quad (3.49)$$

Substituting equation (3.48) into equation (3.42b) and using equation (3.35) the expression of the probe amplitude reflection $r = u_1/s_1$ is given by

$$r(\delta) = \frac{2\tau_{a0}/\tau_e}{j(\delta - \Delta)\tau_{a0} + \eta - (1 + j\alpha_H)[y + xF(\delta)]}. \quad (3.50)$$

3.4.2 Asymptotic behavior

In this section, equation (3.50) at resonance ($\Delta = 0$) is evaluated in two asymptotic cases.

3.4.2.1 Purely absorptive nonlinearity $\alpha_H = 0$

This simple model could describe a TLS with a pump tuned to the maximum of absorption. Now, the assumption that $\Delta = 0$ is taken, then $H(\delta)$ can be expressed as

$$H(\delta) = \frac{1}{\eta - y + j\delta\tau_{a0}}. \quad (3.51)$$

At resonance, $\delta \rightarrow 0$ and $|j\delta\tau_{a0}| \ll \eta - y$ which leads to

$$H(\delta) = \frac{1}{\eta - y} - \frac{j\delta\tau_{a0}}{(\eta - y)^2}. \quad (3.52)$$

Substituting this last relation in equation (3.49) and making the same approximations, the following equation is obtained:

$$F(\delta) = \frac{1}{(1+x)^2 + \frac{x}{y-\eta}} + j \frac{\delta \left[\frac{T_1}{y-1} - \frac{\tau_{a0}x}{(\eta-y)^2} \right]}{\left[(1+x)^2 + \frac{x}{y-\eta} \right]^2}, \quad (3.53)$$

with $F(\delta) = p + j\delta q$, the reflection coefficient reads

$$r(\delta) = \frac{2\tau_{a0}/\tau_e}{\eta - y - xp + j\delta(\tau_{a0} - xq)}. \quad (3.54)$$

The power reflection coefficient $|r(\delta)|^2$ has a Lorentzian profile and the associated Q -factor can be easily evaluated using

$$Q = \frac{\omega_0}{2} \left| \frac{\tau_{a0} - xq}{\eta - y - xp} \right|. \quad (3.55)$$

In the case of a long carrier lifetime: $T_1 \gg \tau_{a0}$, using equation (3.53) simpler expressions for q and p and the overall Q -factor are obtained

$$Q = \frac{\omega_0 T_1 (y - \eta) x}{2(y - 1) |\xi(x)| [\xi(x) + x]}, \quad (3.56)$$

where

$$\xi(x) = (\eta - y)(1 + x)^2 - 2x \quad (3.57)$$

One can check that $\xi(x) + x > 0$. For $\eta < 9/8$, $\xi(x)$ can be null for two distinct values x_1 and x_2 ($x_1 < x_2$) of x . This is the bistability condition for a nonlinear absorptive resonator [Boyd 2003]. At the matching values of the input pump power, the probe cavity Q -factor dramatically increases. The normalized reflected power at resonance given by

$$|r(0)|^2 = \left[\frac{2\tau_{a0} [\xi(x) + x]}{\tau_e (\eta - y) \xi(x)} \right]^2, \quad (3.58)$$

can be higher than unity since $\xi(x) \rightarrow 0$ when $x \rightarrow x_1$: the signal probe is amplified. This behavior comes from a differential gain [Gibbs 1976] experienced by the probe due to the nonlinear shape of the transmission curve of the device as illustrated at figure 3.4. The saturation of the differential amplification can be calculated by numerically solving equations (3.37) and (3.39).

The enhancement of the Q -factor results from the bistable behavior of the cavity. Indeed, in this configuration, in the bistability power zone, the pump reflectivity and phase shift have a very stiff profile. Consequently, the probe signal undergoes a strong phase shift together with a steep amplitude transmission. This leads to a strong dispersion as well as to a differential amplification. Assuming now that $\eta \approx 1$, which is possible since $1 < \eta < 9/8$, equation (3.56) can be written

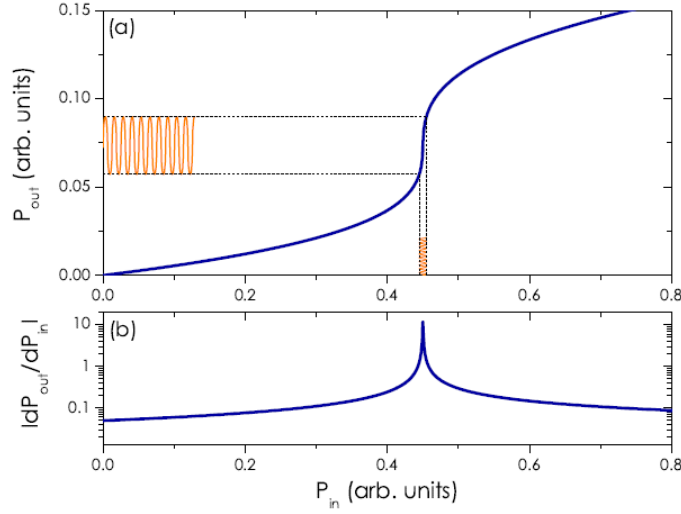


Figure 3.4: (a) Nonlinear transfer function $P_{out} = f(P_{in})$ where $P_{out} = |u_0|^2$ of a cavity just below the bistability threshold. The transfer function of a small modulation stemming from the beating between the pump and the probe fields is also schematically sketched. (b) For input power values close to the switching power ($P_{in} = 0.45$ in the example), the differential gain $|dP_{out}/dP_{in}|$ can be very high and can even diverge for bistable cavities.

$$Q = \frac{\omega_0 T_1 x}{2|1-x|}. \quad (3.59)$$

This last equation explicitly shows that the Q -factor enhancement is twofold: i) as expected, the photon lifetime and thus the Q -factor are proportional to T_1 and ii) for $x \rightarrow x_1 = 1$, the Q -factor can be arbitrarily increased. As already discussed, the latter effect also gives a strong differential amplification which can be useful to compensate for residual losses of the cavity. For $x \approx 0$ and $x \gg 1$ equations (3.8) and (3.59) give the same results; the two approaches differ only when $x = x_1$ and $x = x_2$. From another point of view, if $\eta \gg 1$ then

$$|\xi(x)| \approx \xi(x) + x \approx \eta(1+x)^2, \quad (3.60)$$

noting that $y-1 = -1/(1+x)$ one can check that equations (3.8) and (3.56) lead to the same expression of the Q -factor. Thus it becomes clear that far from bistability, the saturable absorber model used in the present calculations is equivalent to the non-resonant pump approach shortly introduced in section 3.1.

In the case of a short carrier lifetime: $T_1 \ll \tau_{a0}$, the carrier density can be adiabatically eliminated and the Q -factor enhancement only comes from the nonlinear behavior of the cavity. The Q -factor reads

$$Q = \frac{\omega_0 \tau_{a0} \left\{ [\xi(x) + x]^2 + x^2 \right\}}{2(\eta - y) |\xi(x)| [\xi(x) + x]}. \quad (3.61)$$

In the limit of $\eta \approx 1$ and $x \approx 1$, Q can be approximated by

$$Q = \frac{2\omega_0 \tau_{a0}}{|1 - x|}, \quad (3.62)$$

the Q -factor enhancement is only brought about by the bistable effect controlled by the pump beam. Comparing equation (3.59) and equation (3.62), the Q -factor enhancement coming from the carrier oscillations, which is about $T_1/(4\tau_{a0})$ for a given unsaturated absorption.

3.4.2.2 Dispersive regime: $\alpha_H \gg 1$

The cavity nonlinearity is thus mainly dispersive. In this case, it can be considered that $x \ll 1$ and consequently $y \approx x$. $\Delta_0 = \Delta\tau_{a0}$ and $X = \alpha_H x$ is set. These assumptions lead to

$$H(\delta) = \frac{-j\alpha_H}{\eta + j[\delta\tau_{a0} + \Delta_0 + X]}, \quad (3.63)$$

which is used to write

$$F(\delta) = \frac{\eta + j[\delta\tau_{a0} + \Delta_0 + X]}{\eta - \delta T_1(\Delta_0 + X) + j(\Delta_0 + 2X + \eta\delta T_1)}. \quad (3.64)$$

The amplitude reflection coefficient is now

$$r(\delta) = \frac{2\tau_{a0}/\tau_e}{\eta + j\{\delta\tau_{a0} - \Delta_0 - X[1 + F(\delta)]\}}. \quad (3.65)$$

The expression of the group delay τ_g is deduced from the expression of $r(\delta)$

$$\tau_g(\delta) = -\frac{\partial \arg[r(\delta)]}{\partial \delta}. \quad (3.66)$$

In the studied configuration $Q = \omega_0 \tau_g(0)/2$ [Li 2010], which enables to calculate the overall Q -factor

$$Q = \frac{-\omega_0 T_1 X \sigma(X)}{2[\vartheta(X)]^2 [\vartheta(X) - X^2]} \quad (3.67)$$

where it has been set

$$\vartheta(X) = \eta^2 + (\Delta_0 + 2X)^2 \quad (3.68a)$$

$$\sigma(X) = \eta^2 [\Delta_0 X(8\Delta_0 + 9X) + \Delta_0 \eta^2 + 2(\Delta_0^3 + X^3)] + (\Delta_0 + X)^2 (\Delta_0 + 2X)^3. \quad (3.68b)$$

The Q -factor enhancement mechanism is the same as in the absorptive case. As it has been underlined in the absorptive case, the Q -factor is proportional to

the population lifetime T_1 . $\vartheta(X)$ is strictly positive and thus never goes to zero. Nevertheless, assuming

$$\Delta_0 < -\sqrt{3}\eta, \quad (3.69)$$

which is the dispersive bistability condition for the pump [Gibbs 1985], the following equation

$$\vartheta(X) - X^2 = 0 \quad (3.70)$$

can have two solutions $X_1 = \alpha_H x_1$ and $X_2 = \alpha_H x_2$. When the normalized intracavity pump energy is close to one of these two values the Q-factor is strongly increased due to the nonlinear phase-shift and the differential amplification. This will be illustrated at section 3.5.

As a conclusion, this analytical study emphasizes the physical effects producing a strong Q-factor enhancement in a nonlinear microcavity. It is important to highlight that the cavity has a nonlinear behavior only for the pump beam. This induces a strong dispersion on the probe beam via the saturation of the absorption or the cross nonlinear index. The strong increase in the dispersion value is due to the stiff phase shift undergone by the probe near the transition points of the bistable cavity transfer function. Finally, in certain domain of parameters, the delay associated to this phase shift adds up to the increase of the group index due to the CPO effect.

3.5 Numerical results

The analytical model gives expressions for the radiative and external coupling Q-factors, $Q_{rad} = \omega_0 \tau_{rad}/2$ and $Q_e = \omega_0 \tau_e/4$ respectively. Without absorption, for a linear microcavity, the maximal attainable Q-factor is given by $1/(Q_{rad}^{-1} + Q_e^{-1})$. The associated normalized reflection is $\left(\frac{Q_{rad}}{Q_{rad} + Q_e}\right)^2$. All the following results have been obtained in a cavity with radiative losses such as $\tau_{rad} = \tau_e$. We will now consider full numerical calculations.

3.5.1 Absorptive nonlinearity

In this section a medium with a strong absorption and negligible nonlinear dispersive effects on the pump ($\alpha_H = 0$) is considered. In order to reach the pump induced bistability regime we assume that $\eta = 1.05$. The aim of this study is to show that the induced dispersion can be used to increase the probe Q-factor under realistic conditions. For this purpose, a long carrier lifetime such as $T_1 = 250\tau_{a0}$ is considered.

3.5.1.1 Probe reflectivity spectrum

This part is focused on the case where a pump field is set at the cavity resonance ($\omega_P = \omega_0$). Three reflection spectra are depicted in figure 3.5.a for three different values of x . The dash curve is obtained for $x = 0$, the resulting overall Q-factor is equal to Q_0 and the reflection under this condition is very low ($< 10^{-3}$) since $\tau_{a0} \ll \tau_e$. The reflection spectrum displays a very narrow peak when x increases

($x = 0.1$ and $x = 0.3$) mainly due to the fact that a strong dispersion is induced by the pump via the carrier oscillations. In the meantime, the absorption saturation increases the photon lifetime τ in the cavity and both effects sum up to improve the reflected power. These two effects were expected according to the basic model description at section 3.1. The bistability does not play any role here since the chosen values of x are sufficiently far from the turning points (x_1 and x_2) as shown in figure 3.5.b. Next to the switching zone of the bistable power curve, the probe can be amplified. In figure 3.5.c the normalized intracavity energy is set close to the first turning point (x_1) in order to obtain 100% reflectivity. This spectrum is compared with the one of an identical non absorbant cavity ($\alpha = 0$). Still slightly increasing the pump input power ($x = 1.24$) a strong Q -factor enhancement ($2.5 \times 10^4 Q_0$ instead of $20Q_0$ in the best linear configuration) is now observed together with a selective amplification as depicted in figure 3.5.d.

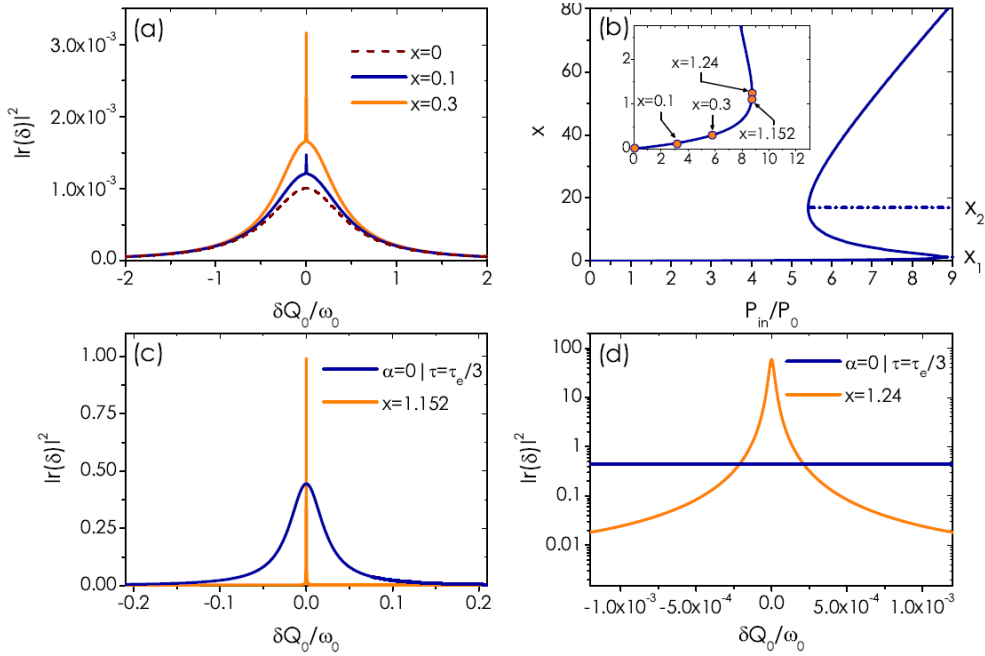


Figure 3.5: (a) Probe reflection spectra for three values of x for a nonlinear cavity with $\eta = 1.05$, $\alpha_H = 0$ and $T_1 = 250\tau_{a0}$. (b) Intracavity normalized pump energy as a function of the input pump power. The inset is a zoom of the lowest part of the curve. (c) Probe reflection spectra, the value of $x = 1.152$ has been set to obtain a 100% reflection. The case $\alpha = 0$ corresponds to an absorption-free linear cavity. (d) Example of a reflection spectrum with a high differential selective amplification.

3.5.1.2 Frequency pulling

The introduction of the CPO effect generates a strong dispersion of the medium in the cavity achieving a linewidth narrowing that, in contrast to the methods based on geometrical designs and technological performance, is robust and not critical in

terms of field detunings with respect to the cavity resonance. This way the resonance frequency of the narrowed cavity is fixed by the pump frequency. The numerical calculations predicting this so called *frequency pulling* effect are presented in this section.

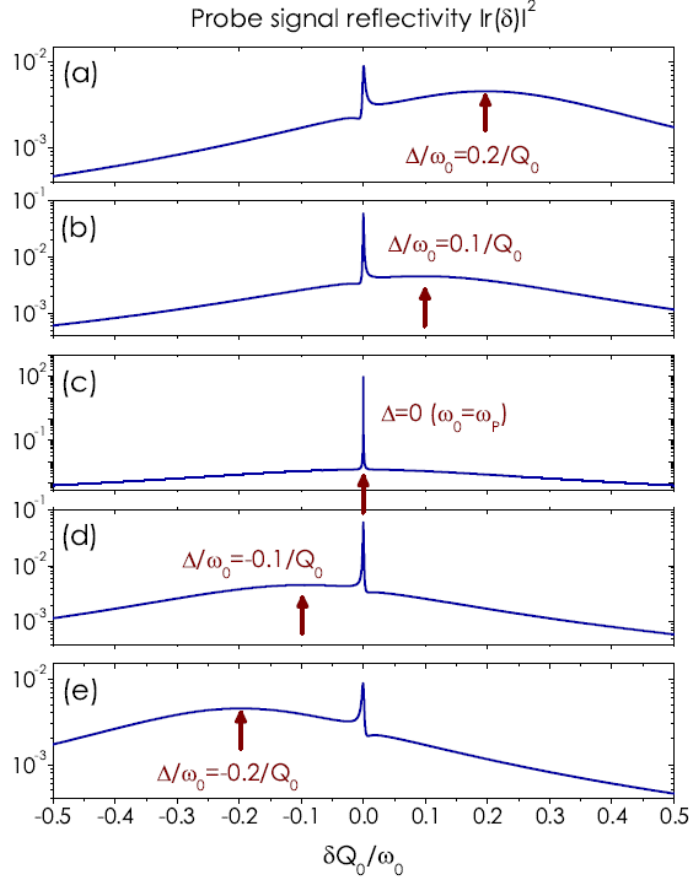


Figure 3.6: Probe reflection spectra for several values of cavity/pump detuning (a) $\Delta/\omega_0 = 0.2/Q_0$ (b) $\Delta/\omega_0 = 0.1/Q_0$ (c) $\Delta = 0$ ($\omega_0 = \omega_p$) (d) $\Delta/\omega_0 = -0.1/Q_0$ (e) $\Delta/\omega_0 = -0.2/Q_0$. In all the cases $x = 1.24$ and the arrow points out the cavity resonances.

Figure 3.6 shows reflection spectra calculated for five values of the detuning Δ decreasing from $0.2\omega_0/Q_0$ to $-0.2\omega_0/Q_0$. The intracavity energy is $x = 1.24$. In this figure the arrow points out the initial cavity resonance. For all the initial detunings, the probe resonance is pulled towards the pump frequency and its resonance is obtained at $\omega_s \approx \omega_P$ ($\delta \approx 0$). This effect has already been discussed for EIT [Lukin 1998].

However, figure 3.6 also shows that the reflectivity decreases with a broader cavity/pump detuning. This can be compensated for by increasing the pump power. Figure 3.7 depicts the same conditions for a normalized intracavity energy and a pump detuning respectively set at: $x = 1.42$ and $\Delta = -\omega_0/(15Q_0)$. The reflectivity coefficient is about 100% and the resonance is at least two orders of magnitude

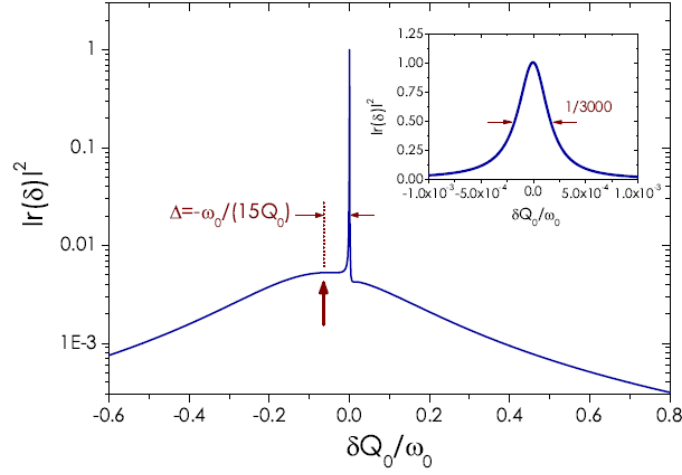


Figure 3.7: Probe reflection spectra for $\Delta = -\omega_0/(15Q_0)$ and $x = 1.42$ in a logarithmic scale. The inset depicts the resonance with a linear scale. The resonance full width at half maximum is $\omega_0/(3000Q_0)$.

narrower than the cavity/pump detuning.

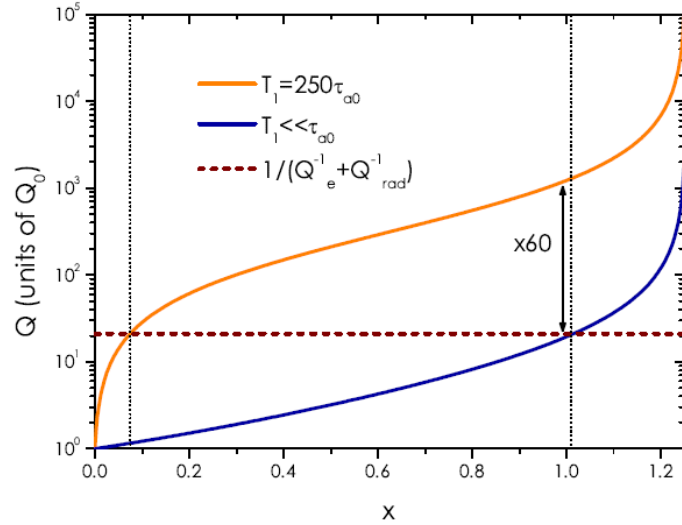


Figure 3.8: Quality factor for the probe signal as a function of the normalized pump intracavity energy x for $T_1 = 250\tau_{a0}$ and $T_1 \ll \tau_{a0}$. We have also plotted the value of the Q -factor of an equivalent linear cavity without absorption.

3.5.1.3 Role of population oscillations

In the previous calculations a long carrier lifetime was assumed. In this section, the reflectivity coefficients are compared in the cases where $T_1 \gg \tau_{a0}$ and $T_1 \ll \tau_{a0}$. In the first case, the Q -factor enhancement is due to a combination of population oscil-

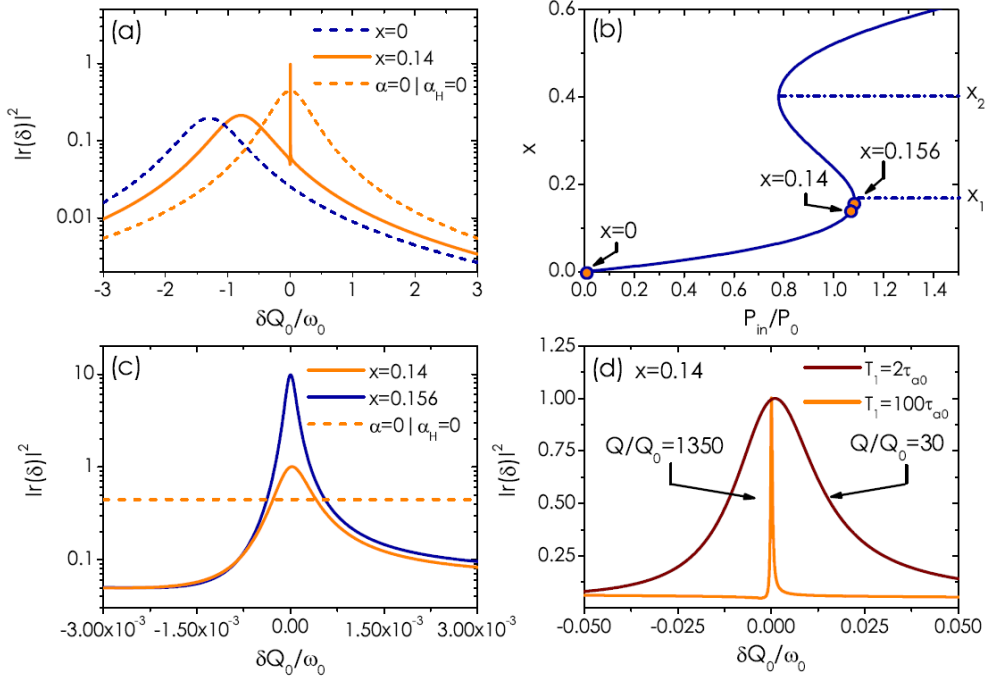


Figure 3.9: (a) Probe reflection spectra for $x = 0$ (dash dark line) and $x = 0.14$ (full line) in the case of a nonlinear cavity which physical characteristics are $\eta = 3$, $\Delta_0 = -3\sqrt{3}\eta/2$, $\alpha_H = 25$ and $T_1 = 100\tau_{a0}$. For $x = 0.14$, the cavity reflection is 100%. For comparison, the bright dash line represents the spectrum of the same cavity in the linear and absorption-free case ($\alpha = 0$). (b) Intracavity normalized pump energy as a function of the input pump power. (c) Probe reflection spectra for $x = 1.4$ and 0.156 . (d) Reflectivity spectrum calculated for $x = 0.14$ assuming $T_1 = 100\tau_{a0}$ or $T_1 = 2\tau_{a0}$.

lations and nonlinear effects whereas in the second case, the Q -factor enhancement is exclusively related to the pump bistability effects. At figure 3.8 the Q -factor enhancement is plotted in comparison with the unsaturated cavity Q -factor (Q_0) both for $T_1 = 250\tau_{a0}$ and $T_1 \ll \tau_{a0}$. For $x \leq 0.2$ and $T_1 = 250\tau_{a0}$, the Q -factor increase is mainly due to population oscillations and for $x \geq 0.2$ the nonlinear effect induces an additional improvement. The straight horizontal dash line is the Q -factor of the cavity without absorption.

For high values of T_1 , the dispersion induced by the pump strongly rises the Q -factor in comparison with the short lifetime carrier approach. For example, in the case $T_1 = 250\tau_{a0}$, $Q = 1/(Q_e^{-1} + Q_{rad}^{-1})$ for $P_{in} = 2.1P_0$ ($x = 0.08$) whereas in the limit of very short T_1 , an input power $P_{in} = 8.6P_0$ ($x = 1.02$) is required to obtain the same enhancement. At this power value the Q -factor is 60 times larger at $T_1 = 250\tau_{a0}$ than that at $T_1 \ll \tau_{a0}$. These results highlight the convenient effects of the population oscillations induced dispersion. Firstly it produces an increase factor around $T_1/(4\tau_{a0})$ and secondly it reduces the required power for a given Q -factor

enhancement. This enables to use an input power much lower than the switching power. Note that near the switching point, the system is strongly sensitive to pump fluctuations as it is the case for delay lines based on critical slowing down [Bonifacio 1979, Daunois 1988]. As a consequence the system combining CPO and nonlinear effects is less sensitive to pump fluctuations and thus much more stable than purely nonlinear system where $T_1 \ll \tau_{a0}$.

3.5.2 Dispersive nonlinearity

We will now briefly discuss the dispersive nonlinearities. This case will be extensively addressed in chapter 4 in regard to our actual experimental results. A dispersive medium with $\alpha_H = 25$ is considered and $\eta = 3$ is taken to avoid absorptive bistability. The cavity/pump detuning is set to $\Delta_0 = -3\sqrt{3}\eta/2$ in order to produce dispersive bistability. In most of the cases presented in this paragraph $T_1 = 100\tau_{a0}$ is used. Figure 3.9.a shows the reflectivity spectrum for $x = 0.14$; we compare this spectrum with those without pumping ($x = 0$) or without absorption ($\alpha = 0$). As already extensively discussed in the absorption dominated case, the cavity resonance width is strongly reduced and next to the switching point as shown in figure 3.9.b the reflection signal can be increased ($|r(0)|^2 = 1$ for $x = 0.14$) in comparison with the absorption-free cavity case ($|r(0)|^2 = 4/9$). Figure 3.9.c presents the reflectivity spectra for $x = 0.14$ and $x = 0.156$ on a smaller frequency span. For $x = 0.14$ the Q -factor enhancement is 1350. For $x = 0.156$ the enhancement is around 5000 and the resonant reflectivity is close to 10. Finally in figure 3.9.d the reflectivity spectrum has been plotted again for $x = 0.14$ and $T_1 = 100\tau_{a0}$ but also for $T_1 = 2\tau_{a0}$. The ratio between the two Q -factor enhancement values is 45 which is in good agreement with equation (3.67).

3.6 Conclusion

We have studied theoretically coherent population oscillations in a nonlinear microcavity. We proposed to simple approaches. First, we proposed a Fabry-Perot cavity where we introduced perturbatively the CPO effect and a nonlinear refractive index showing in a simple manner how both contributions ad up enhancing of the cavity lifetime. Second, we developed a CMT model where we considered a generic two level system (semiconductor, atomic medium, ...) driven by a *powerful* pump field and probed by a weak signal. These analytical models enable us to discuss the physical processes which lead both to a strong enhancement of the Q -factor and to a control of the transmission at the probe frequency.

The photon lifetime of a microcavity containing a TLS where only CPO occurs can be strongly increased by the reduction of the group velocity of the light coupled into the cavity. The cavity lifetime is then basically limited by the population lifetime T_1 . However, as in the CPO approach it remains a residual unsaturated absorption that limits the reflected power from the cavity. This leads to a moderate value of CPO enhanced Q -factor.

In a nonlinear microcavity a strong Q -factor enhancement can also be achieved. In this case the cavity has nonlinear behavior for the pump beam inducing a strong dispersion on the probe beam. The dispersion value increases as the probe gets near the transition points of the bistable cavity transfer function. This way, in order to get high dispersion the regime becomes less stable.

Finally, in certain domain of parameters, the delay associated to this phase shift adds up to the increase of the group index due to the CPO effect. This is the case we are most interested since we obtain strong stable enhancement of the cavity Q -factor.

Additionally, the simultaneous action of population oscillations and the nonlinear response of the cavity induces a strong intracavity dispersion and a differential gain. This technique could be used to stabilize a microcavity using the frequency pulling effect for example, in fact we will show an experimental demonstration of this effect in an photonic crystal nonlinear nanocavity in the next chapter.

Experimental Demonstration

Contents

4.1	The L3 PhC cavity	48
4.1.1	Fabrication of the L3 PhC cavity	49
4.1.2	Photoluminescence characterization of the L3 PhC cavity	51
4.2	Tapered fiber assisted coupling into the L3 PhC cavity	52
4.2.1	Fabrication and characterization of the tapered fiber	52
4.2.2	Coupling efficiency	53
4.3	Pump and probe generation	55
4.4	Optical Detection	56
4.4.1	Measurement of the delays	57
4.5	Temporal Measurements	62
4.6	Spectral Measurements	66
4.7	Frequency Pulling	67
4.8	Theoretical and experimental comparison	69

Experiments of slow light in photonic crystals cavities were performed using modified L3 PhC cavity containing semiconductor quantum wells (QWs) as active, absorptive, nonlinear medium [Grinberg 2012]. The light is coupled into the cavity using a tapered fiber. The pump and probe fields required for the CPO effect are produced by the intensity modulation of a single laser beam. The measurements of the delay and the probe intensity are performed using a home-made lock-in amplifier system.

In figure 4.1, a general scheme of the experimental set-up is represented. A fibered continuous-wave (cw) laser emitting up to 15 mW and tunable from 1490 nm to 1650 nm is used. In order to avoid thermal effects, the cw laser is modulated with a fibered acousto-optic modulator producing 100 ns duration square pulses repeated every 20 μ s, longer than the thermal relaxation time [Moreau 2010]. The CPO effect is induced by a sine-wave intensity modulation with a time period longer than the electron-hole recombination time $\tau_r = 200$ ps, the sine-wave modulation is generated using a fibered Mach-Zehnder interferometer. The beam passes then through a circulator that allows to send the transmission to the tapered fiber, coupling thus the light in the cavity, and recovering the reflection. The reflected signal is sent to a fast avalanche photo-diode (APD). The measurement of the delay and intensity of the probe is achieved using a home made lock-in amplifier whose outputs are

sensitive to the in- and out-of-phase quadratures of the modulation. In this chapter a detailed description of the sample and each of the parts of the experimental setup is presented.

Using this set-up we experimentally implement some of the predictions of chapter 3. In particular we demonstrate, through temporal and spectral measures, a strong enhancement of the cavity Q -factor. We also put into evidence the frequency pulling effect.

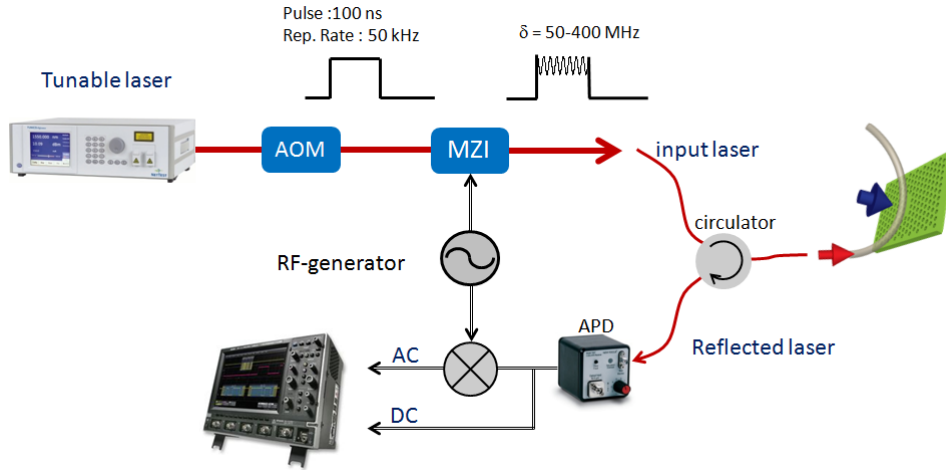


Figure 4.1: Set-up used to perform the experiments on slow light in the semiconductor photonic crystal cavity.

4.1 The L3 PhC cavity

The photonic crystals (PhCs) are $10 \mu\text{m} \times 50 \mu\text{m}$ air hole triangular lattice InP suspended membranes. The nanocavity is placed in the center of the PhC, as shown by the scanning electron microscope (SEM) image in figure 4.2. The L3 nanocavity is made by missing three holes over a line during fabrication. In order to achieve a higher value of Q -factor the two holes closing the cavity are shifted apart by $0.15a$. Indeed, Noda et al. [Akahane 2003] have demonstrated that this shift increases the cavity quality factor by almost one order of magnitude.

The PhC period and hole radius are $a = 450 \text{ nm}$ and $r = 120 \text{ nm}$, respectively. The PhC membrane is grown by metalorganic vapour phase epitaxy (MOCVD) and contains four central layers of InGaAs/InGaAsP quantum wells (QWs) (see figure 4.3.a) each layer with a thickness of $\sim 13.5 \text{ nm}$ and $\sim 16 \text{ nm}$ for the well and the barrier, respectively. The QWs luminescence at 300 K, measured over an unetched region, close to the PhC, is centered at $\sim 1.51 \mu\text{m}$ (see figure 4.3.b) with a spectral broadening of 75 nm. The membrane thickness (265 nm , $\lambda/2n_{\text{eff}}$) is set such that the field maximum (at 1550 nm) is located at the center of the membrane, matching the location of the active material. A SiO_2 sacrificial layer

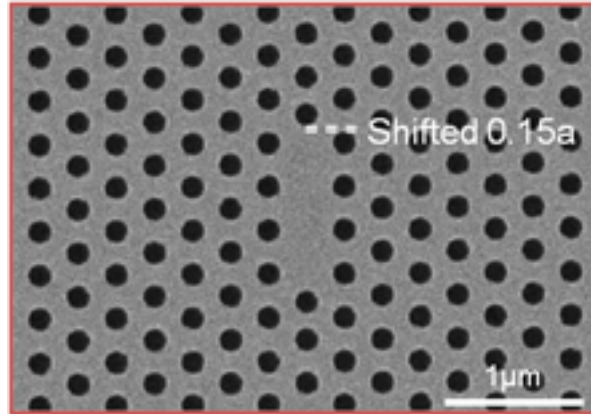


Figure 4.2: SEM (scanning electron microscope) image of a modified L3 cavity (triangular lattice with period $a=450$ nm, holes radius $r=120$ nm). The two holes closing the cavity are shifted away by $0.15a$.

underneath the InP is bonded on a Si substrate through a benzocyclobutene (BCB) layer [Karle 2010]. A $1\ \mu\text{m}$ air spacer, obtained after etching the sacrificial layer, lies between the InP membrane and the substrate.

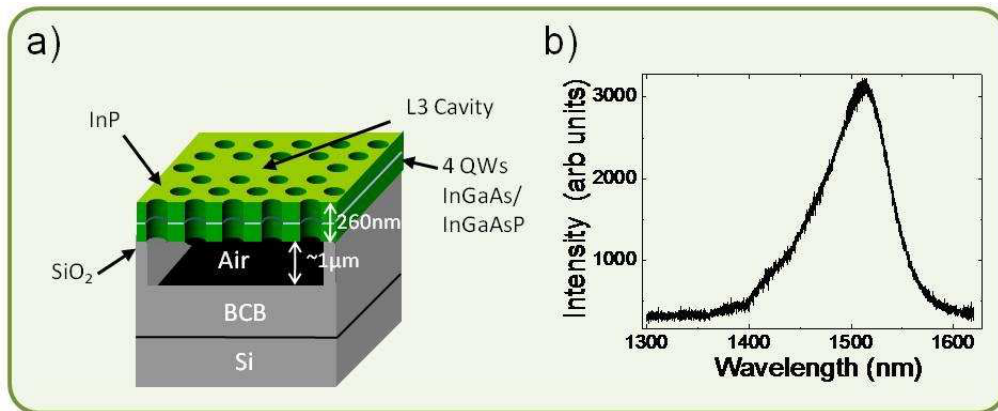


Figure 4.3: (a) L3 PhC nanocavity and the quantum wells. (b) Quantum wells photoluminescence spectrum when pumped at 810 nm.

4.1.1 Fabrication of the L3 PhC cavity

This section contains a brief description of the fabrication process. The samples were fabricated in the clean room facilities of LPN by Alexandre Bazin, Yacine Halioua, Fabrice Raineri, Isabelle Sagnes and Remy Braive. More details about the fabrication process are given in [Karle 2010].

The first step is the metalorganic vapour phase epitaxy (MOCVD) of the InP structure. This starts by the growth of an InGaAs etch stop over an InP substrate, followed by an InP layer, which will form the suspended membrane. In its center, four InGaAsP/InGaAs QWs are grown. The membrane total thickness is ~ 265 nm and it corresponds to $\lambda/2n_{\text{eff}}$ with n_{eff} the effective refractive index calculated as the weighted average of the refractive index of air and material. Finally, a 1 μm -thick sacrificial layer of SiO_2 is deposited over the InP active membrane. This structure is positioned (upside down) over a Si substrate coated with a BCB layer used for the bonding, see figure 4.4. In order to polymerize the BCB and finalize the bonding, a hard bake is performed in a nitrogen atmosphere for 2h at 300°C.

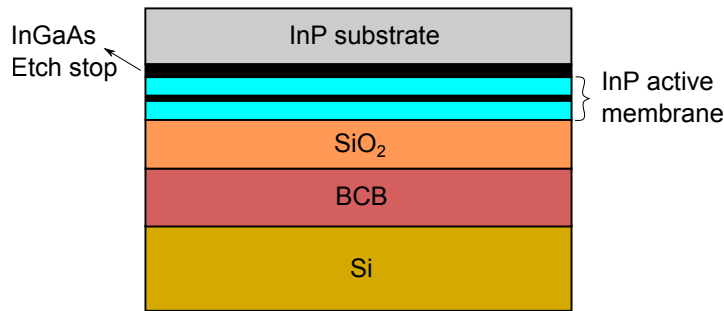


Figure 4.4: Sketch of the structure before the etching processes

Once hard baked, the InP substrate is removed by HCl wet etching. The InGaAs etch stop is removed using $\text{H}_2\text{SO}_4:\text{H}_2\text{O}_2:\text{H}_2\text{O}(3:1:1)$ leaving on top the InP layer with the QWs.

The second step is the fabrication of an etching mask in order to define the geometrical parameters of the 2D PhC. This mask is made of a 300 nm thick layer of Si_3N_4 deposited at 300°C by PECVD (Plasma Enhanced Chemical Vapor Deposition) over the InP. The SiN is then covered by 450 nm of an electro-sensitive resin (PMMA, Polymethyl Methacrylate). The sample is positioned in an e-beam writer (LEICA EBPG 5000+) which allows to focus an electron beam over the resin following the structure design, with 2.5 nm precision. Then, using an appropriate chemical solution the isolated regions are dissolved.

After the resin exposure, the design is transferred into the nitride layer by a dry etching using a CCP-RIE (Capacitively Coupled Plasma-Reactive Ion Etching) which allows a directional etching. Then the motif is transferred to the semiconductor by a ICP-RIE (Inductively Coupled Plasma-Reactive Ion Etching). During this stage the InP membrane is drilled by cylindrical air-holes (few hundreds nm depth) down to the SiO_2 sacrificial layer.

Finally, in order to obtain the suspended membrane, the SiO_2 sacrificial layer is etched in a HF wet atmosphere. The HF is able to penetrate into the sample through the holes dissolving the sacrificial layer. Residual HF resting on the sample is removed by a supercritical drying technique.

4.1.2 Photoluminescence characterization of the L3 PhC cavity

Right after the fabrication, the sample (both QWs and PhC cavity) is characterized by measuring its photoluminescence. The experimental set up used for this purpose is shown in figure 4.5. The sample is pumped at 810 nm using a pulsed Ti:Sa laser source having a 80 MHz-repetition rate and 100 fs-pulse duration. The pump is focused on the sample with a 50X microscope objective ('Mitutoyo', M Plan Apo NIR, 50X, $f = 170$ mm, NA=0.42). The emission is collected by the same objective and sent to, either a CCD camera in order to visualize the sample, or to a spectrometer ('Princeton Instruments', Acton SP2500i, with a 600 g/mm grating 1.6 μm blaze and Ni cooled camera) to record the spectrum of the QWs fluorescence. After passing through the spectrometer the signal is sent to an InGaAs 1D array spectroscopy camera ('Princeton Instruments', OMA V, spectral range 0.7 μm -1.6 μm , resolution FWHM: 0.315 nm).

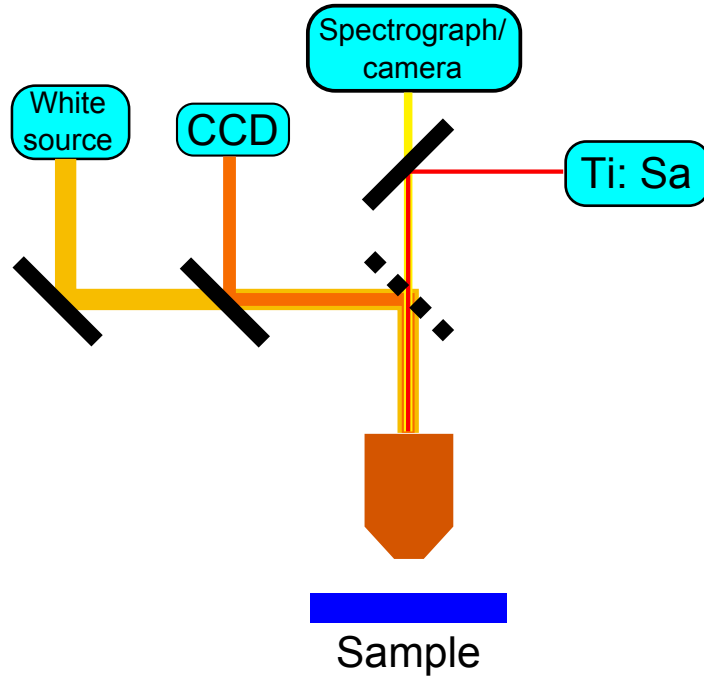


Figure 4.5: Sketch of the set up used to characterize the QWs sample

First, a characterization of the photoluminescence spectrum of the QWs for different excitation intensities is performed. Figure 4.3.b shows a typical photoluminescence spectrum. Independently, the radiative lifetime was measured by Maia Brunstein [Brunstein 2011] finding it is of the order of $\tau_r \simeq 200$ ps. Secondly, the photoemission of the active material (QWs) is also used to identify the cavity mode under incoherent pumping. Indeed, the resonant cavity mode filters the broadband luminescence giving a spectral narrow peak. A typical spectrum of the L3 cavity described above is shown in figure 4.6, for a pump average power of 36 μW at the pupil of the microscope objective. A mode centered at 1565 nm is observed. The

quality factor obtained from the FWHM of the cavity ($\Delta\lambda = 1.1$ nm) resonance gives $Q \sim 1700$. It is important to point out that the measurement of the quality factor $Q = \lambda/\Delta\lambda$ by means of photoluminescence spectra has two limitations: one instrumental, since the FWHM of the emission peak is limited by the monochromator resolution and one inherent to the system, due to the material absorption, which leads to pump power dependent quality factors. Therefore, the Q -factor measured for low pumping powers has to be considered as a lower bound limit approximation of the intrinsic quality factor. More precise values will be measured later on.

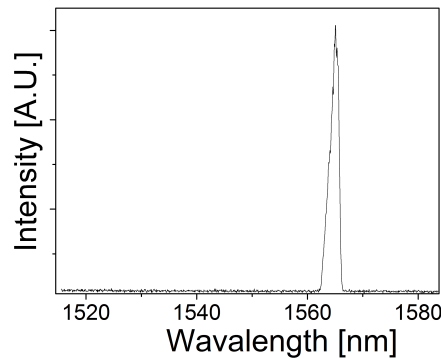


Figure 4.6: Photoluminescence spectrum of a L3-type cavity for a pump power of $36 \mu\text{W}$ and 0.5 s of integration time. The mode is centered at $\lambda = 1565$ nm and the resonance width is 1.7 nm (for this injected power). The PhC period and radius are: $a = 450$ nm and $r = 120$ nm, respectively.

4.2 Tapered fiber assisted coupling into the L3 PhC cavity

In order to couple light into the L3 PhC cavity, we use the tapered fiber approach since it diminishes insertion, propagation and absorption losses in a waveguide while it easily allows probing several cavities on a chip. However, this coupling method requires a device allowing to control the taper position and displacement with high accuracy (sub- μm resolution) and stability. This system was developed at the LPN by Maia Brunstein during her PhD [Brunstein 2011, Brunstein 2009] in collaboration with Laurent Bigot from Laboratory PhLAM (Laboratoire de Physique des Lasers, Atomes et Molécules) in Lille. Figure 4.7 shows a sketch of the system.

4.2.1 Fabrication and characterization of the tapered fiber

This section contains a brief description of the fabrication process of the taper, fabricated at the Laboratoire de Physique des Lasers, Atomes et Molécules (PhLAM) in Lille by Laurent Bigot.

The tapered fiber, with a diameter of $\sim 1.5 \mu\text{m}$, has an U-shape and is fixed on

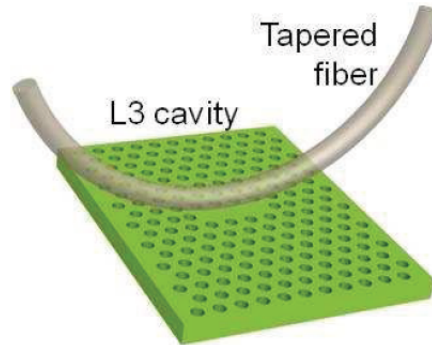


Figure 4.7: PhC nanocavity evanescently coupled to the outside by a tapered fiber.

a microscope slide. The fabrication process starts with a standard single-mode telecommunications fiber. The plastic jacket is removed exposing the $125\ \mu\text{m}$ cladding in a region of the order of 3 cm. After this, the fiber is fixed at both extremities and a gas burner is positioned 1 mm under the naked fiber. The two fixed points pull out the fiber at a speed of $50\ \mu\text{m/s}$ during 175 seconds until a minimum diameter between 1 and $3\ \mu\text{m}$ is reached. Once the fiber is tapered down, it is bent in the narrow part forming an U-shape and then stuck on the microscope slide using UV glue in such a way that the thin curved segment (between 0.5-1 cm) is freely standing in air. Such length of the free standing segment achieves a good compromise between mechanical stability and physical constraints in the set-up. In addition, the curvature of the fiber at the stretched segment reduces the optical coupling to the substrate outside the PhC membrane, thus decreasing optical losses [Hwang 2005]. Finally, two APC fiber pigtailed were soldered at each fiber end.

For the characterization of the taper, losses are measured by means of a continuous wave laser source emitting at 1550 nm. It is important to point out that the taper diameter also plays a dramatic role: for diameters lower than $1.5\ \mu\text{m}$ the fiber becomes extremely unstable and fragile (losses rapidly increase with the use). On the other hand, for diameters larger than $4\ \mu\text{m}$, the evanescent tail of the optical mode out of the fiber is reduced and the coupling in the L3 PhC cavity becomes inefficient. The tapers used during this work have diameters between 1.5 and $3\ \mu\text{m}$.

4.2.2 Coupling efficiency

The microscope slide with the tapered fiber is fixed in a 3-axes stage with two piezoelectric (PZT) driven axes (x-z) as shown in figure 4.8. The PZT is used to set the fiber exactly over the cavity. Besides, the sample is also mounted on PZT-driven axes that allow to move it in the x-y directions, as shown in figure 4.8. Hwang et al. [Hwang 2005] have demonstrated that the maximal coupling efficiency is obtained for a PhC-taper gap of $0.1\ \mu\text{m}$. However, fiber-sample distances as short as $0.1\ \mu\text{m}$ cannot be fixed in our system since the fiber systematically sticks on the sample surface, most probably due to electrostatic forces originated by charges

accumulated on the fiber. Nevertheless, the contact configuration ensures robustness to the system and reproducibility, since it guaranties the system stability during measurements. A picture of the whole sample is shown in figure 4.9(a) where each tiny square corresponds to a PhC and the red curved line to the tapered fiber. Figure 4.9(b) shows a picture of the PhC with the fiber positioned over the PhC cavity. In order to reduce mechanical vibrations of the taper due to air currents and decrease thermal fluctuations and humidity, the whole device (sample plus tapered fiber) is covered with a Polymethyl methacrylate (PMMA) box.

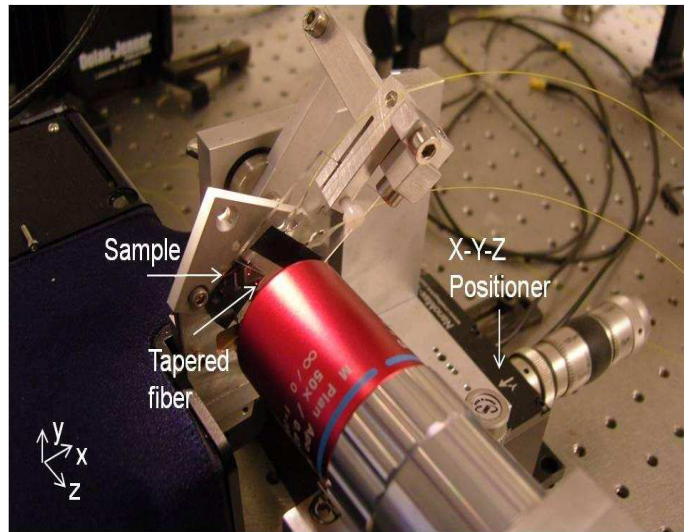


Figure 4.8: Set up to place the fiber over the PhC. A 3-axes stage (Nanomax) is used to precisely set the position of the fiber over the cavity.

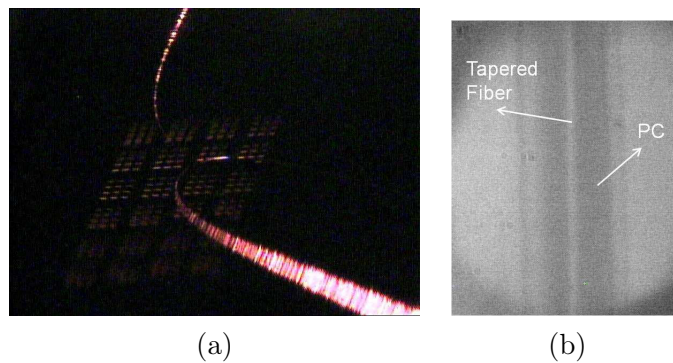


Figure 4.9: (a) Image of the whole sample and the tapered fiber. (b) Visible image of the PhC membrane with the fiber positioned above the cavity.

The coupling efficiency was characterized using a 80 MHz repetition rate, 120 fs-duration laser pulses delivered by an Optical Parametric Oscillator (OPO) ('Opal', Spectra physics). The mean wavelength of the 30 nm-linewidth pulses is set to be in coincidence with the cavity resonance wavelength and sent through a fibered po-

larization controller to a circulator and then through the tapered fiber as shown in figure 4.10. The polarization state is changed by means of the polarization controller to optimize the optical coupling. The circulator allows measuring both the transmitted (through the taper) and the reflected signals. Both signals are sent to an optical spectrum analyser (OSA). The best measured coupling efficiency was 28%. We must clarify that this result is the maximal that could be attained using the tapered fiber method. However, the coupling efficiency has a strong dependence on the position of fiber on the sample and on the level of degradation of the fiber itself. Thus each fabricated tapered fiber has a different coupling quality. The coupling efficiency of the tapered fiber used in the L3 PhC cavity experiment was of $\sim 7\%$.

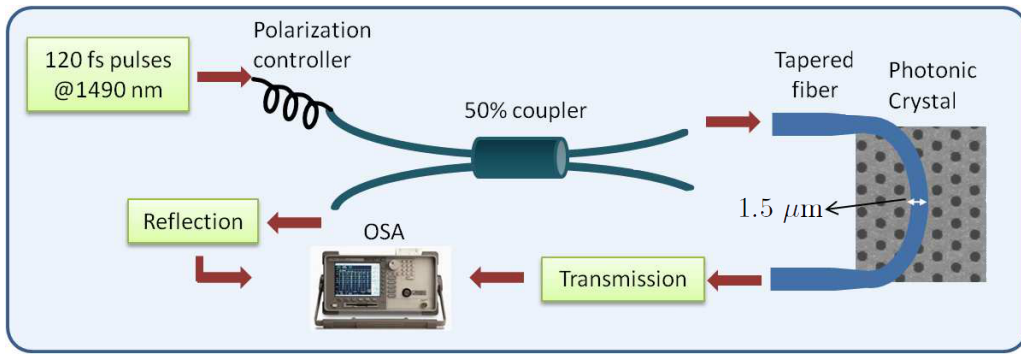


Figure 4.10: Set up used to the characterize the coupling between the tapered fiber and the nanocavity. A SEM image of the L3 cavity is shown.

4.3 Pump and probe generation

As discussed in more details in chapters 1 and 3, the CPO effect is induced by a pump beam and a probe beam with their relative frequency detuned by δ , which should be smaller than $1/\tau_r$. $\tau_r = 200$ ps being the electron-hole recombination time in the quantum wells. For the experimental point of view, the pump and the probe are produced starting from a single laser source whose intensity is modulated using the sine-wave function $\sin(\delta t)$. From the spectral point of view, this modulation induces in the Fourier space two new spectral components at $\omega \pm \delta$ around the carrier oscillating at the optical frequency ω and which corresponds to the average intensity of the beam (see figure 4.11). It is then the modulation amplitude and the average intensity that play respectively the role of the probe and the pump that are required to induce the CPO effect.

Practically, the intensity modulation is achieved by driving a fibered Mach-Zehnder interferometer (MZI) with a rf signal, following the function $f(t) = 1 + m \sin(\delta t)$, where m is the depth of the modulation and δ the modulation frequency, as shown in figure 4.11. So the function describing the beam after passing through

the MZI can be written as:

$$\varepsilon = (\varepsilon_0 e^{i\omega t} + cc) \times f(t) = \varepsilon_0 \left[e^{i\omega t} + \frac{m}{2} (e^{i(\omega-\delta)t} + e^{i(\omega+\delta)t}) \right] + cc \quad (4.1)$$

where we recognize the fields oscillating at ω with amplitude ε_0 , and the fields at $\omega \pm \delta$ with amplitude $\varepsilon_0 \frac{m}{2}$.

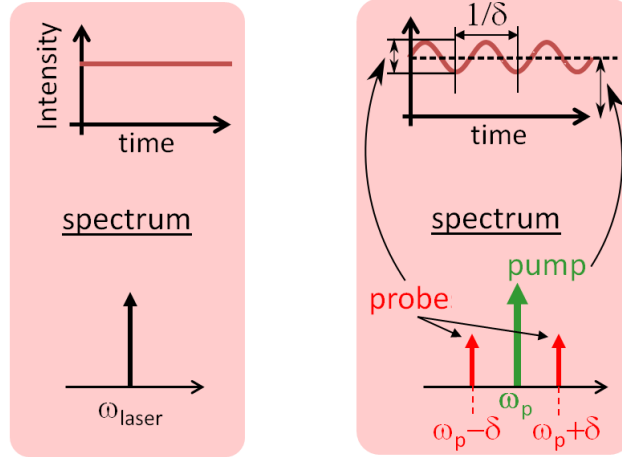


Figure 4.11: Sketch of the Fourier space for a continuous or intensity modulated beam

The source used to generate the pump and probe is a tunable, from 1490 nm to 1650 nm, continuous-wave (cw) laser emitting up to 15 mW (Yenista Tunics-T100R). In order to avoid thermal effects, the cw laser is modulated using a fibered acousto-optic modulator producing 100 ns duration square pulses with a repetition rate of 50 kHz, longer than the thermal dissipation time [Moreau 2010]. The CPO effect is induced by using a sine-wave intensity modulation with a time period longer than electron-hole recombination time $\tau_r = 200$ ps [Bigelow 2003a, Baldit 2005]. By driving the fibered Mach-Zehnder interferometer with an RF signal, a 10% intensity modulation depth is applied to the square pulses. The rf signal oscillating at the frequency δ is supplied by a pulse function arbitrary generator (Agilent 81150A or Agilent E40428). The beam passes then through a circulator that allows to send the transmission to the tapered fiber and recover the reflection of the cavity. The reflected signal is sent to a fast Avalanche Photo-Diode (APD, New Focus 1647) with a bandwidth of 1.1 GHz. The measurement of the delay and intensity of the probe are achieved using a home made lock-in detection whose outputs are sensitive to the in- and out-of-phase quadratures of the modulation.

4.4 Optical Detection

In our experiments, most of the time, we measure the delays achieved by the L3 PhC cavity. We have then developed a detection system that is sensitive to the phase.

We start by detecting the light reflected by the cavity which we retrieve using the optical circulator connected to the tapered fiber. The output of the circulator is then directly connected to the fibered APD. Figure 4.12.b shows a typical electrical signal corresponding to the reflection detected at the APD for an input signal depicted in figure 4.12.a. We recognize the 100 ns square pulse with the small amplitude modulation. The reflected signal is rather noisy since the signal level is very low. To extract the delay achieved in the cavity from the noisy amplitude modulation we have developed a lock-in amplifier.

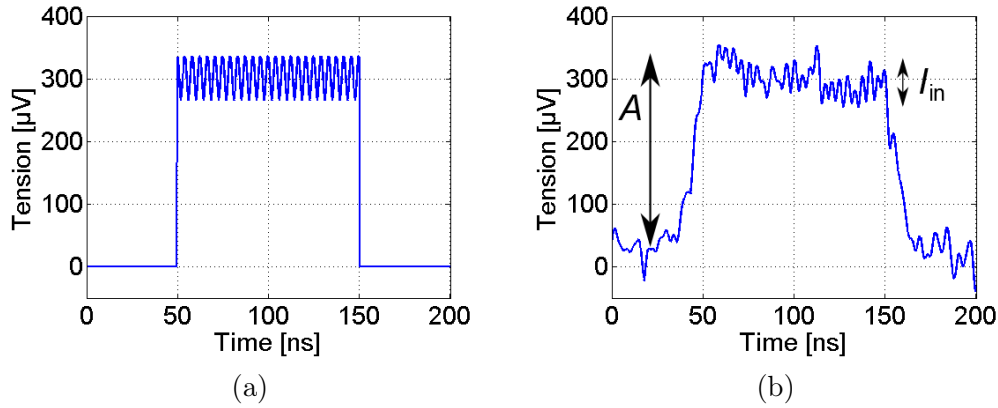


Figure 4.12: Shape of the input signal (a) and typical signal obtained by the APD detector (b), for a square pulse duration of 100 ns and a modulation frequency $\delta = 240$ MHz.

4.4.1 Measurement of the delays

Basically, a lock-in amplifier is aimed to analyze a noisy electrical signal at a particular frequency by mixing it with a sine-wave reference oscillating, at the same frequency. The lock-in amplifier delivers then the amplitude of the signal with a high signal-to-noise ratio and its phase relative to the phase of the reference. Mathematically, the electrical signal delivered by the APD and corresponding to figure 4.12, can be written as:

$$I_{\text{probe}}(t) = A + I_{\text{in}} \cos(\delta t + \phi) \quad (4.2)$$

where A corresponds to pump amplitude, I_{in} to the modulation amplitude corresponding to the probe, and ϕ is the phase of the modulation carrying the information on the delay induced in the cavity. In the lock-in amplifier the signal (4.2) is mixed with a sine-wave reference. In fact, two references are necessary to obtain the amplitude and the phase of the modulation: an "in-phase" reference R_1 and an "out-of-phase" reference R_2 whose phase is shifted by 90° with respect to the phase of R_1 . These two references can be written as:

$$R_1(t) = R \cos(\delta t + \phi_r) \quad (4.3)$$

and

$$R_2(t) = R \cos\left(\delta t + \phi_r + \frac{\pi}{2}\right) = R \sin(\delta t + \phi_r) \quad (4.4)$$

We have supposed that $R_1(t)$ and $R_2(t)$ have the same amplitude R . When mixing the signal (4.2) with the references we obtain:

$$\begin{aligned} S_1(t) &= R \cos(\delta t + \phi_r) I_{\text{in}} \cos(\delta t + \phi_s) \\ &= \frac{RI_{\text{in}}}{2} [\cos(\phi_s - \phi_r) + \cos(2\delta t + \phi_s + \phi_r)] \end{aligned} \quad (4.5)$$

$$\begin{aligned} S_2(t) &= R \cos(\delta t + \phi_r) I_{\text{in}} \sin(\delta t + \phi_s) \\ &= \frac{RI_{\text{in}}}{2} [\sin(2\delta t + \phi_s + \phi_r) - \sin(\phi_s - \phi_r)] \end{aligned} \quad (4.6)$$

Both $S_1(t)$ and $S_2(t)$ have a constant term and one oscillating at 2δ . To extract the pertinent information only the constant term is kept, obtaining:

$$S_1 = \frac{RI_{\text{in}}}{2} \cos(\phi_s - \phi_r) \quad (4.7)$$

$$S_2 = -\frac{RI_{\text{in}}}{2} \sin(\phi_s - \phi_r) \quad (4.8)$$

From (4.7) and (4.8), the phase of the probe relative to the reference can be obtained through:

$$\begin{aligned} \frac{S_2}{S_1} &= \frac{-\sin(\phi_s - \phi_r)}{\cos(\phi_s - \phi_r)} = \tan(\phi_r - \phi_s) \\ \phi_s - \phi_r &= \arctan\left(\frac{S_2}{S_1}\right), \end{aligned} \quad (4.9)$$

and the delay between the probe and the reference can then be calculated:

$$\tau_g = \frac{\arctan\left(\frac{S_1}{S_2}\right)}{2\pi\delta} \quad (4.10)$$

We emphasize here that τ_g is the group delay which is the derivative of the phase with respect to the frequency. However, and according to the work of Q. Li *et al.* [Li 2010], the cavity lifetime in our case, is given by $\tau = \tau_g/2$.

The amplitude of the modulation (probe) is obtained by adding the square power of both signals:

$$\begin{aligned} S_2^2 + S_1^2 &= \left(\frac{I_{\text{in}}R}{2}\right)^2 \\ I_{\text{in}} &= \frac{2\sqrt{S_2^2 + S_1^2}}{R} \end{aligned} \quad (4.11)$$

It is worth noting that the delay (4.10) and the amplitude (4.11) are given relatively to the reference phase ϕ_r and amplitude R respectively. However, as these values are constants during the experimental measurements, variations in τ and I_{in} are associated to physical effects occurring in the cavity.

For the experimental demonstrations we developed two types of lock-in amplifiers.

Electronic home-made lock-in amplifier The electronic setup used is sketched in figure 4.13. The frequency of the sine-wave modulation was $\delta = 240$ MHz.

This particular frequency is a good compromise as it fulfills the requirement $\delta < 1/\tau_r$ and allows to measure delays up to 4 ns. The reference of the lock-in detection is supplied by a second exit of the same wave generator used to drive the MZI for the amplitude modulation. The relative phase between the two exits of the generator can be controlled and it is set respectively at 0° and 90° to obtain the in and out of phase references. Before the mixing, the DC part of the signal is filtered out using a 50 MHz high pass filter (Mini Circuits BHP-50). The AC part is then amplified electronically. After the mixing, the term oscillating at 2δ is eliminated with a 90 MHz low pass filter (Mini Circuits BLP-90), ending with electrical signals proportional to the probe amplitude modulation quadratures S_1 and S_2 , obtained respectively when $\phi_r = 0$ and $\phi_r = 45^\circ$.

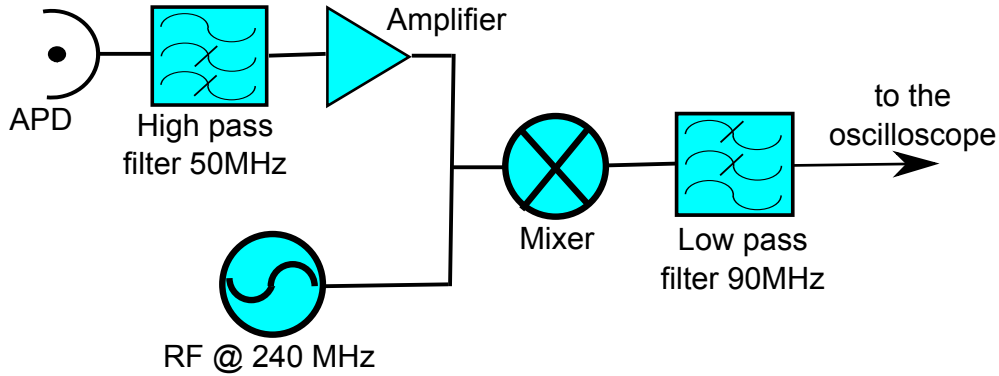


Figure 4.13: Sketch of electronic set-up used to demodulate the signal

The performance of the lock-in system is tested on a signal similar to the one depicted in figure 4.12, delivered by the laser without going through the cavity. Its intensity is adjusted using an attenuator in order to have the same magnitude as the signal obtained on the actual experiments with the cavity. The results are shown in figure 4.14 showing the evolution of the signal as the laser power increases. Figure 4.14.a shows the pump intensity, proportional to the DC component of the signal (equation 4.2), and the demodulated probe amplitude (equation 4.11); both show a linear dependence with respect to the laser power as expected. Figure 4.14.b shows the in and out of quadrature terms corresponding to S_1 and S_2 , normalized by the amplitude of the modulation $\sqrt{S_1^2 + S_2^2}$. They are thus proportional to the cosine and sine of the phase $\phi - \phi_{\text{ref}}$. We can see that for the low intensities (less than $\sim 4\text{mW}$) the signal is very noisy; for higher powers both signals remain constant as the laser power increases. This shows that relative phase between the signal and the reference is constant (equation (4.10)), provided the intensity is sufficiently high. We show this graphically in figure 4.14.c where we see that the relative delay remains

constant with the exception of the low power region, where noise dominates. This confirms the good functioning of the home-made lock-in system.

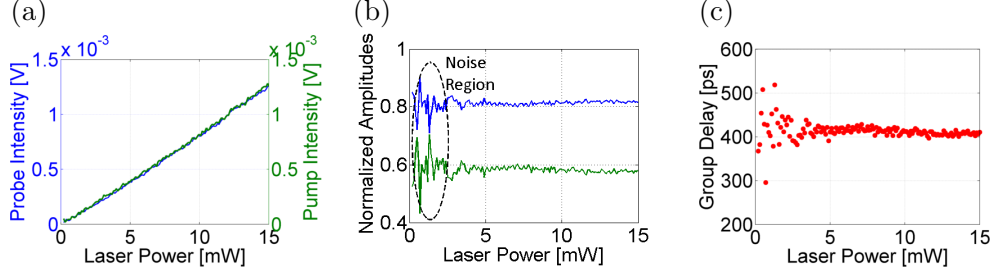


Figure 4.14: Direct measurements (without cavity). (a) Demodulated probe intensity (blue) and pump intensity (green) as a function of the laser power. (b) In and out quadratures S_1 and S_2 , normalized by the modulation amplitude as a function of laser power. (c) Group delay as a function of the laser power.

Figure 4.15 is equivalent to figure 4.14, but this time the signal comes from the L3 PhC cavity. Figure 4.15.a shows now a highly nonlinear behavior for both the pump and the probe amplitudes. We can also see in figure 4.15.b that in this case the normalized in and out of phase amplitudes vary in a different way, indicating that the relative phase between the signal and the reference is changing as the power is increased. As shown in figure 4.15.c, this enables us to measure the delay induced in the nanocavity (except for the low power regions where signal is too noisy).

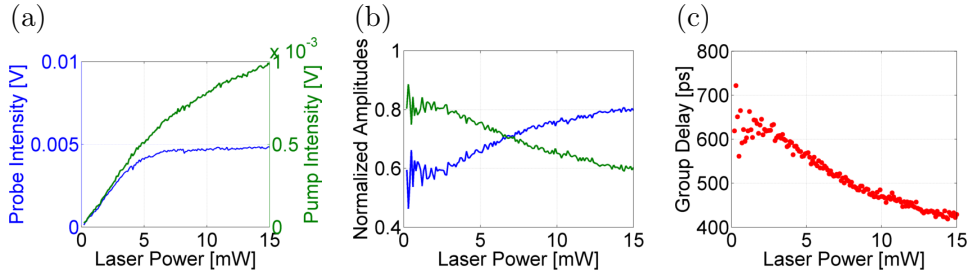


Figure 4.15: Cavity measurements. (a) Demodulated probe intensity (blue) and pump intensity (green) as a function of the laser power. (b) In and out quadratures S_1 and S_2 , normalized by the modulation amplitude as a function of laser power. (c) Group delay as a function of the laser power.

Digital home-made lock-in amplifier The measurements reported in this thesis are recorded as a function of various parameters such as power, wavelength, or pump-probe detuning. The latter is simply achieved by changing the modulation frequency δ . When this particular parameter is tuned, the electronic lock-in amplifier has to be rebuilt and optimized for each frequency δ . To overcome this difficulty the phase-sensitive detection is performed digitally on an advanced function fast digital oscilloscope (Lecroy Wavemaster 813Zi 13GHz).

The basis of the digital lock-in is to reproduce the electronic treatment numerically. In order to do this we acquire the signal from the APD using a fast oscilloscope for each point of interest, i.e. each wavelength, power and pump-probe detuning. The signal is then averaged on the oscilloscope in order to improve the signal-to-noise ratio. This process is automatized using a *LabView* code that drives the laser source, the function generator and the oscilloscope. The acquired data are then analyzed using a *MatLab* code to retrieve the pump intensity and probe phase and amplitude following the mathematical analysis in section 4.4.1. Simultaneously, the pump intensity is obtained measuring the height of the square pulse. References are generated digitally as a sine and a cosine of the same frequency as the modulation. Using the references we follow the mathematical procedure explained above with the only difference that instead of using a low pass frequency filter we take the mean value to obtain S_1 and S_2 .

4.5 Temporal Measurements

The measurements reported in this section are performed for a fixed pump-probe detuning $\delta = 240$ MHz, while both the laser power and wavelength are tuned. The wavelength is tuned around the cavity resonance wavelength while the power is tuned from 1 to 15 mW from the laser corresponding to 5 to 75 μ W pump power in the tapered fiber incident on the cavity. In a first set of experiments the modulation frequency -hence the pump-probe detuning- is fixed and the electrical home-made lock-in detection described in section 4.4.1 is used.

The first set of measurements is done for a fixed power of the laser as the wavelength is tuned around the L3 PhC nanocavity resonance. In figure 4.16.a is shown the reflected pump as a function of the wavelength for different laser powers. This reflection corresponds to the standard cavity reflection that one can obtain even without the sine-wave amplitude modulation at δ . We recognize for the lowest power an almost symmetrical cavity resonance. When the laser is increased the resonance becomes asymmetric with a stiff variation on the short wavelength side and a smooth fall on the longest wavelength side of the resonance. This kind of asymmetric resonances and wavelengths shifts are the signature of an optical non-linearity in the quantum wells embedded in the cavity and are the precursors of the optical bistability.

Figures 4.16 (b) and (c) are the corresponding amplitude modulation (probe) reflectivities and delays engendered by the nanocavity on the probe at $\delta = 240$ MHz. For each curve, the maximum delay τ_M is achieved for a particular laser wavelength which we call λ_M . After correcting the measured delays from the virtual delay associated to the phase of the reference of the lock-in detections, negative delays are found at long wavelengths. Though confirmed theoretically, their absolute value origins are still not yet understood.

The probe reflectivities reach as well the maximum values at the same wavelength λ_M . It is worth noting that at the same wavelength λ_M , the pump reflectivity is on the stiff side of the resonance. Using the maximum group delay τ_M for each laser power, obtained at λ_M we can calculate the corresponding Q -factor,

$$Q = \frac{\tau_M}{2} \frac{2\pi c}{\lambda_M}.$$

Figure 4.17 shows the maximum group delay and the corresponding effective Q -factor obtained for each laser power. For comparison, the Q -factors corresponding to the loaded cavity (Q_l) and the cavity in the absence of absorption (Q_{rad}) are also indicated in figure 4.17 by the blue and green lines respectively. It becomes clear that as the laser power is increased the total delay, hence the Q -factor is enhanced.

In order to fully understand the behaviors we perform additional studies tuning simultaneously the power and the wavelength. Figure 4.18.a presents the power of the reflected pump as a function of the laser power and wavelength. As the laser power increases the cavity resonance becomes larger and asymmetric. Figure 4.18.b shows the evolution of the amplitude of the modulation (probe) as the laser power

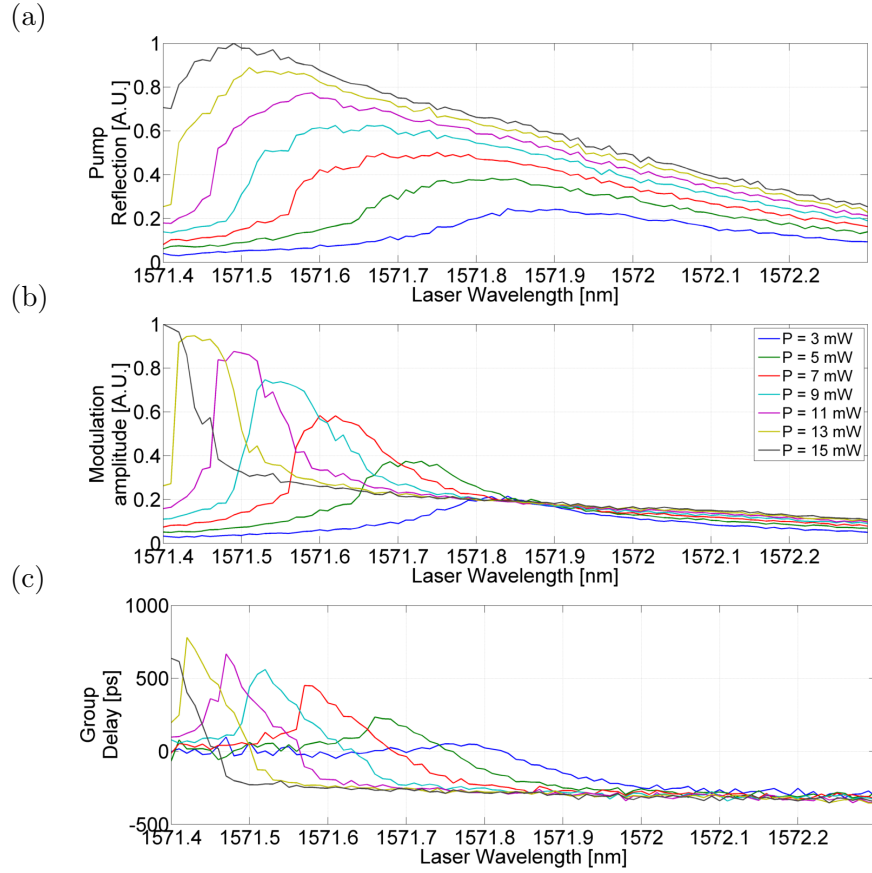


Figure 4.16: Measured pump (a), modulation amplitude (b) reflections and group delay (c) as a function of the laser wavelength for $\delta = 240$ MHz and for different pump intensities.

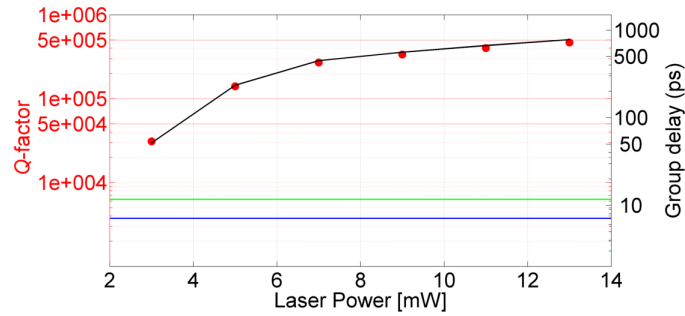


Figure 4.17: • Effective Q -factor and group delay (black line) as a function of the laser power. Blue line $Q_l = 3752$, green line $Q_{\text{rad}} = 6300$.

and wavelength are tuned, the position of the maximum of resonance follows the position of the steepest slope of the pump resonance on the blue side. Finally, figure 4.18.c presents the evolution of delay, it is clear that the position of the maximum delay coincides with the position of the maximum amplitude of the probe; also, if we

follow the delay peak we can see that it is increased as the laser power is increased.

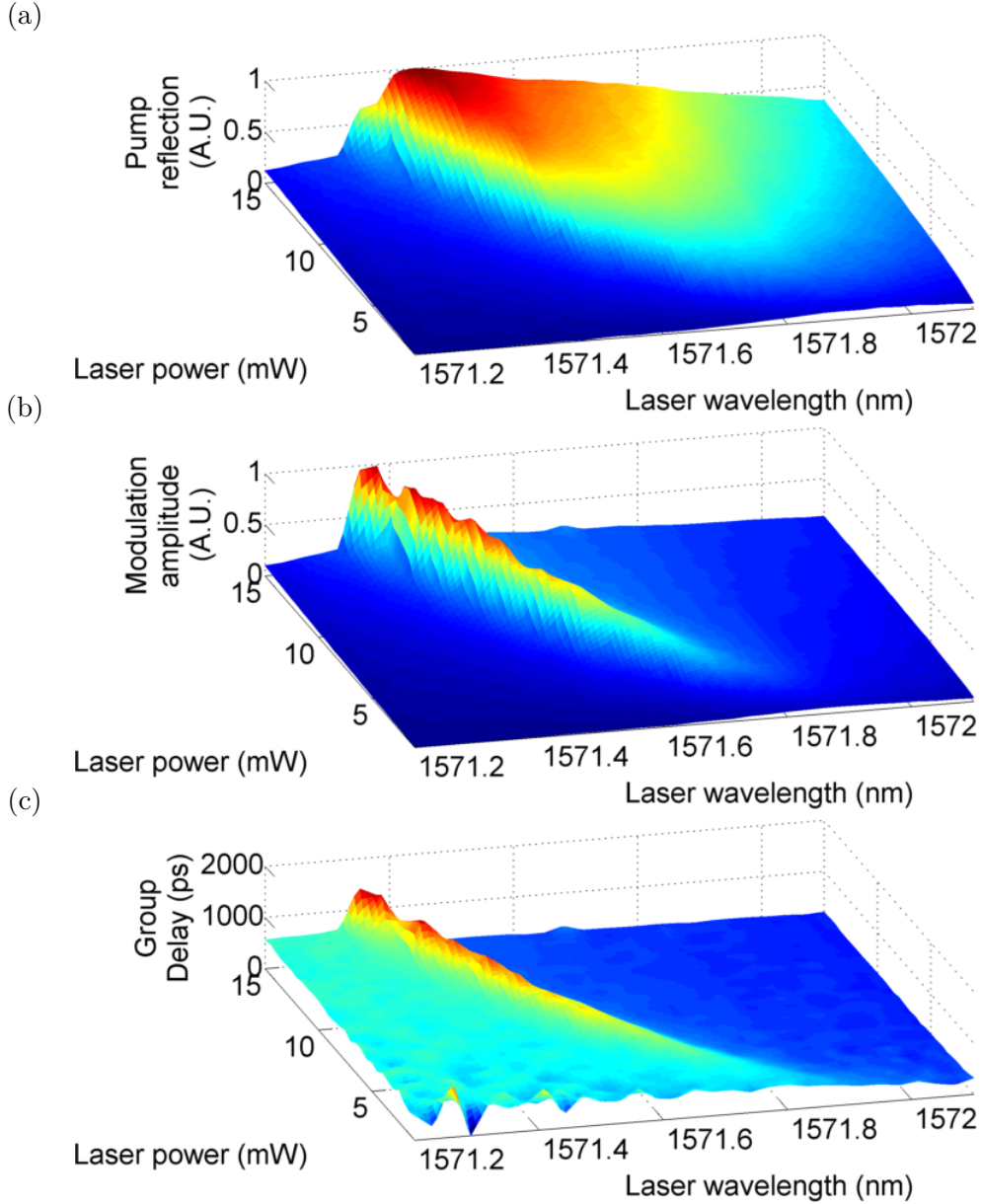


Figure 4.18: Measured pump (a), modulation amplitude (b) reflections and group delay (c) as a function of the laser wavelength and power for $\delta = 240$ MHz and for different pump intensities.

To represent the evolution more clearly we make sections of the 3D figures 4.18, fixing the laser wavelength and showing the evolutions as a function of the laser power. Figures 4.19 (a) and (b) show respectively the measured pump and modulation amplitude reflectivities from the nanocavity as the laser power is changed, for different laser wavelengths. Figure 4.19.c presents the corresponding group delay.

It becomes clear from figure 4.19.a that as we reduce the wavelength, the pump reflection shows a smooth variation as the laser power is increased, and a rapid variation starting at a particular laser power threshold, and then saturates at higher laser powers. Regarding the modulation amplitude, i.e. the probe, figure 4.19.b shows that a maximum value is achieved at a particular laser power, named P_M , for which the pump reflection slope with respect to the laser power is maximum. This laser power value P_M is wavelength dependent, shorter is the laser wavelength and higher is the value of P_M . This is coherent with the results obtained in figure 4.16.a. Concerning the group delay achieved in the L3 PhC cavity, a maximum value is also achieved at P_M , according to figure 4.19.c.

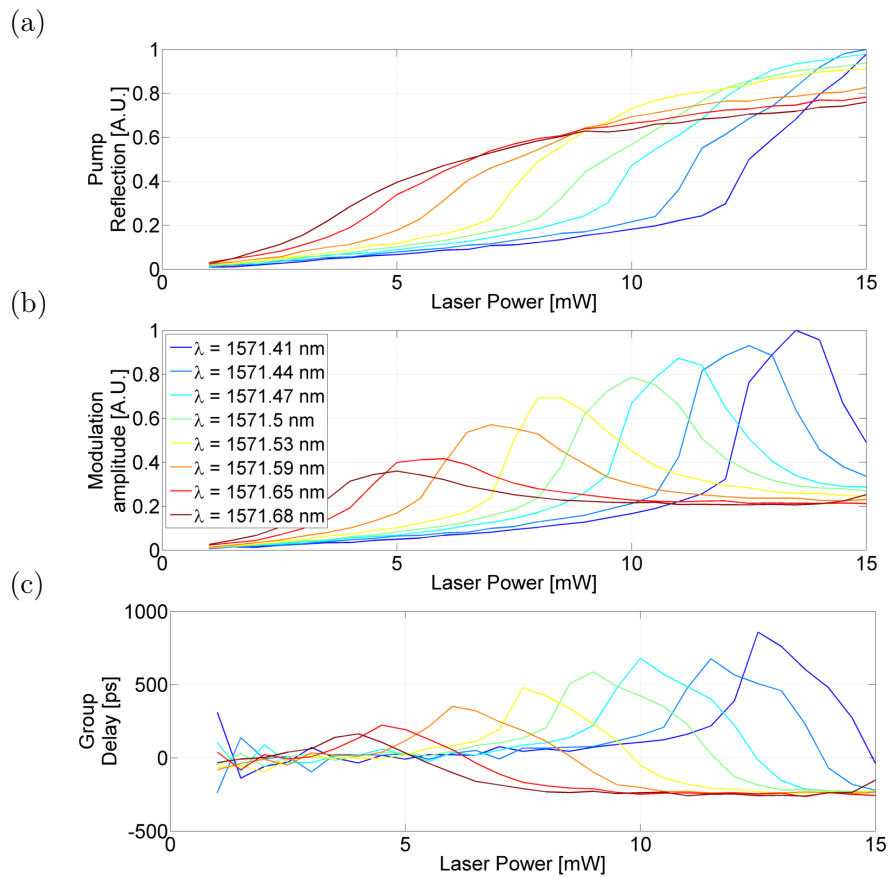


Figure 4.19: Measured pump (a), modulation amplitude (b) reflections and group delay (c) for $\delta = 240$ MHz and for different pump wavelengths.

As we did for the case where we tuned the wavelength for different powers, we calculate the equivalent quality factor for each case. Figure 4.20 shows the equivalent quality factor and group delay as a function of the power P_M at which the maximum delay is attained. We can see that as P_M increases the Q -factor does as well achieving a maximal enhancement of 82 times comparing to the radiation loss limited Q -factor ($Q_{\text{rad}} = 6300$) and 138 times comparing to the loaded Q -factor

($Q_l = 3752$) for $P_M = 14.5$ mW which corresponds to a Q -factor of 520000.

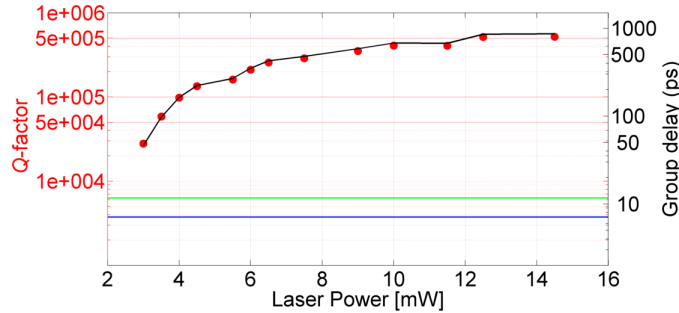


Figure 4.20: • Effective Q -factor and group delay (black line) as a function of the laser power. Blue line $Q_l = 3752$, green line $Q_{\text{rad}} = 6300$.

4.6 Spectral Measurements

For a further confirmation of the enhancement of the nanocavity quality factor spectral measures are performed.

Indeed, as we increase the quality factor, a cavity resonance linewidth narrowing should be observed. Usually this linewidth narrowing is observed by measuring the transmission or the reflection of an electromagnetic field oscillating at ω and by tuning the circular frequency ω around the resonance. In our particular case, this kind of measurements are performed using the digital home-made lock-in described in section 4.4.1. The pump wavelength is set near λ_M and the modulation frequency δ is tuned from 50 to 400 MHz. From a spectral point of view, this is similar to measure the probe beam reflection as the probe frequency is tuned relatively to the pump frequency $\nu_P = c/\lambda_P$ (as explained in section 4.11).

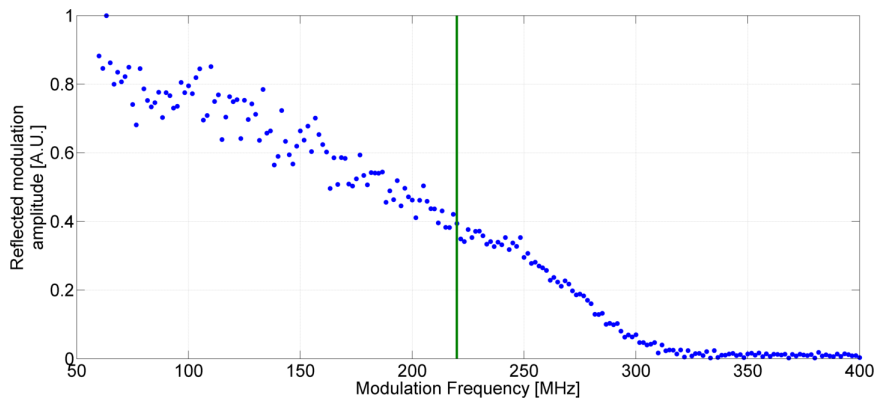


Figure 4.21: Measured modulation amplitude reflection under nonlinear interaction for a pump wavelength near the optimal wavelength λ_M and a power of 10 mW.

Figure 4.21 shows the measured modulation amplitude transfer function of the nanocavity under the CPO configuration. The measurement is achieved using a laser

power of 10 mW, which corresponds to 50 μ W pump power close to the cavity. As the modulation frequency δ is always positive we only measure the half resonance. The resonance Half Width at Half Maximum (HWHM) is about 220 MHz is shown in the figure 4.21 by the green vertical line.

The Q -factor associated to this resonance is then determined knowing that:

$$Q = \frac{\omega}{\Delta\omega}$$

where $\omega = 2\pi c/\lambda_P$ and $\Delta\omega = 2\pi\Delta\nu$. $\Delta\nu = 440$ MHz is the full width at half maximum of the resonance. The Q -factor is $Q = 430000$ is in good qualitative agreement with the overall Q -factor inferred from the measured maximal delay obtained in the temporal measurements, see figures 4.17 and 4.20.

4.7 Frequency Pulling

At last, a study of the spectral hole of the cavity, in terms of the pump-probe detuning is performed for different pump wavelengths. The aim is to analyze this spectral hole for the different wavelength positions with respect to the pump or probe cavity resonance and thus to verify the frequency pulling prediction of chapter 3.5.1.2.

Figure 4.22 shows the modulation reflectivity as a function of the pump-probe detuning δ . This is similar to figure 4.21 for four different laser wavelengths. Note that the four curves have roughly the same shape and linewidth despite the large detunings between the pump frequencies. This is illustrated in the inset, representing the same modulation reflectivity as a function of the frequency relative to a common origin $\nu_M = c/\lambda_M$. For guidance, the theoretical resonance of the nanocavity having the initial quality factor $Q_l = 3752$ is represented in dashed lines. The four vertical lines are the modulation reflectivity resonances extending over hundreds of MHz, whereas the nanocavity linewidth is about 50 GHz. This demonstrates that the final narrow resonance is always achieved in the vicinity of the pump frequency, showing a frequency-pulling-like effect that could be used to overcome technological imperfections.

This result is particularly interesting since, in contrast to usual approaches to achieve high Q -factor nanocavities, in our case the quality factor enhancement is robust and not critical in terms of field detuning with respect to the cavity resonance.

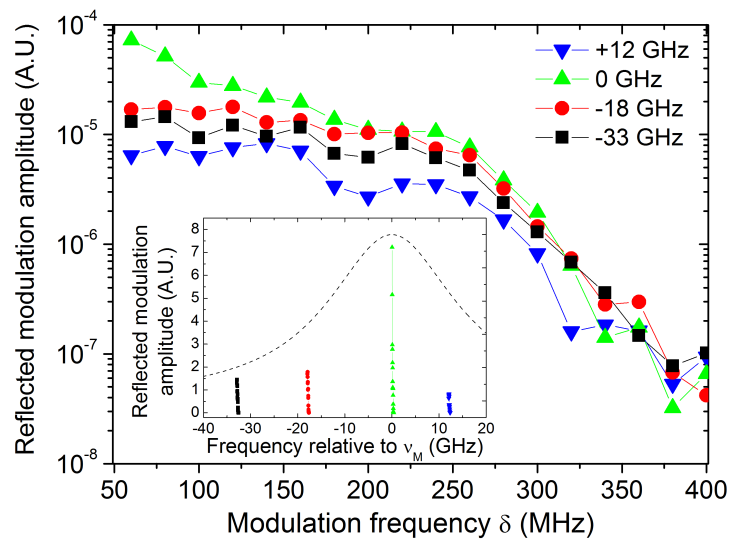


Figure 4.22: Measured reflected modulation amplitude spectra for a pump power of 10 mW and for four different pump frequency ν_P detunings from the optimal frequency ν_M : (\blacktriangledown) 12 GHz, (\blacktriangle) $\nu_P = \nu_M$, (\bullet) -18 GHz, (\blacksquare) -33 GHz. The inset shows in dashed lines the original nanocavity resonance obtained for $Q_l = 3752$ and centered at ν_M . The vertical lines are the few hundreds reflected modulation resonances.

4.8 Theoretical and experimental comparison

In this section the experimental measures are compared with the numerical results obtained via the CMT model developed in chapter 3. The results obtained from temporal and spectral measurements and calculations are compared.

Figure 4.23 shows the theoretical-experimental comparison of the pump and probe reflected powers and the probe group delay as a function of laser wavelength. Figures 4.23 (a) and (b) show respectively the measured pump and modulation amplitude reflectivities from the nanocavity as the laser wavelength is tuned around its resonance, for different laser powers. Figure 4.23.c presents the corresponding group delay for $\delta = 240$ MHz. These experimental results are the same that were shown in figure 4.16. In figures 4.23 (d, e and f) the theoretical results corresponding to the experimental figures 4.23 (a, b and c) are presented.

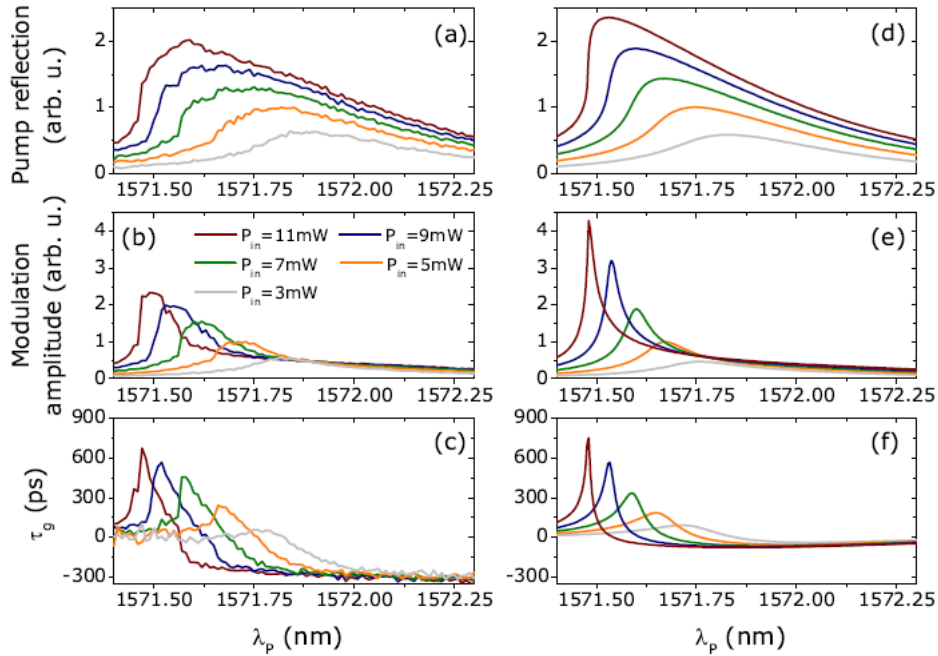


Figure 4.23: Measured pump (a), modulation amplitude (b) reflections and group delay (c) for $\delta = 240$ MHz and for different laser powers as a function of the laser wavelength. (d), (e) and (f) are the corresponding theoretical predictions.

The theoretical evolutions of the pump reflection R_p , the modulation amplitude of the reflection (probe) $R_s(\delta)$ and the group delay $\tau_g(\delta)$ are obtained using the following parameters: $\lambda_0 = 2\pi c/\omega_0 = 1569.96$ nm, $\alpha_H = 25$, $Q_{rad} = 6300$ and $Q_{a0} = 11800$. These values are either independently measured or inferred from experimental measurements.

Note that $Q_0 = 3000$, instead of $Q_0 = 4030$, had to be used in order to reproduce the width of the pump resonance, this value is slightly different from that experimentally measured. This can be explained by the modification in the coupling

conditions between the different experiments. In the numerical calculation we consider $s_1 = s_0/80$ which gives a modulation depth of 10%. The only free parameter is the value of the saturation intracavity energy $|a_{sat}|^2$.

The experimental behaviors, i.e. wavelength shifts, absolute positions, delay vs power and wavelength, are well reproduced. For the highest pump intensity there is a discrepancy on the reflected modulation amplitude and delay that is quite reasonable considering the limited number of adjustable parameters. This is due to limitations both on the measurement of the steep resonances and on the determination of the theoretical parameters close to the highly nonlinear points. For the high wavelengths both experimental and theoretical curves show negative delays. Whereas theory predicts a negative delay of -80 ps, experimentally we measure negative delays up to -300 ps, this result is not yet understood.

Figure 4.24 shows the theoretical-experimental comparison of the pump and probe reflected powers and the probe delay as a function of laser power. Figures 4.24 (a) and (b) show respectively the measured pump and modulation amplitude reflections from the nanocavity as the laser power is changed, for different laser wavelengths. Figure 4.24.c presents the corresponding group delay for $\delta = 240$ MHz. These experimental results are the same that were shown in figure 4.19. In figures 4.24 (d, e and f) the theoretical results corresponding to the experimental figures 4.24 (a, b and c) are presented.

Here also, the experimental behaviors are well reproduced. However, for the highest laser powers and shortest wavelengths there is a discrepancy on the reflected modulation amplitude and delay. This is quite reasonable considering the limited number of adjustable parameters. This is due to limitations both on the measurement of the steep resonances and on the determination of the theoretical parameters close to the highly nonlinear points. As it occurred when tuning the laser wavelength, for the long wavelengths and high laser powers, both experimental and theoretical curves show negative delays. The same disagreement is found, the experimental measurements give negative delays up to -300 ps whereas the theoretical model only predicts negative delays up to -80 ps.

We compare the spectral measurements as well. In figure 4.25 the dots represent the measured modulation amplitude transfer function of the nanocavity under the CPO configuration. The measurement is achieved for a laser power of 10 mW, corresponding to $50 \mu\text{W}$ pump power. The laser wavelength is set near the maximum reflected modulation amplitude λ_M and the modulation frequency δ is tuned from 50 to 400 MHz, changing that way the pump-probe detuning.

The experimental and theoretical results presented in figure 4.25 show qualitative agreement and in the low frequency region ($\delta < 200$ MHz) the agreement is total even from a quantitative point of view. However, it is evident that for higher frequencies differences are noticeable; a signal reduction is observed on theoretical curve but experimental points show null signal from a frequency (δ) of 320 MHz. This disagreement can be partially explained from the fact that the detection system shows a decreasing of the efficiency as the frequency detuning evolves; however, this fact does not explain the phenomenon completely. Resuming, there is a good qual-

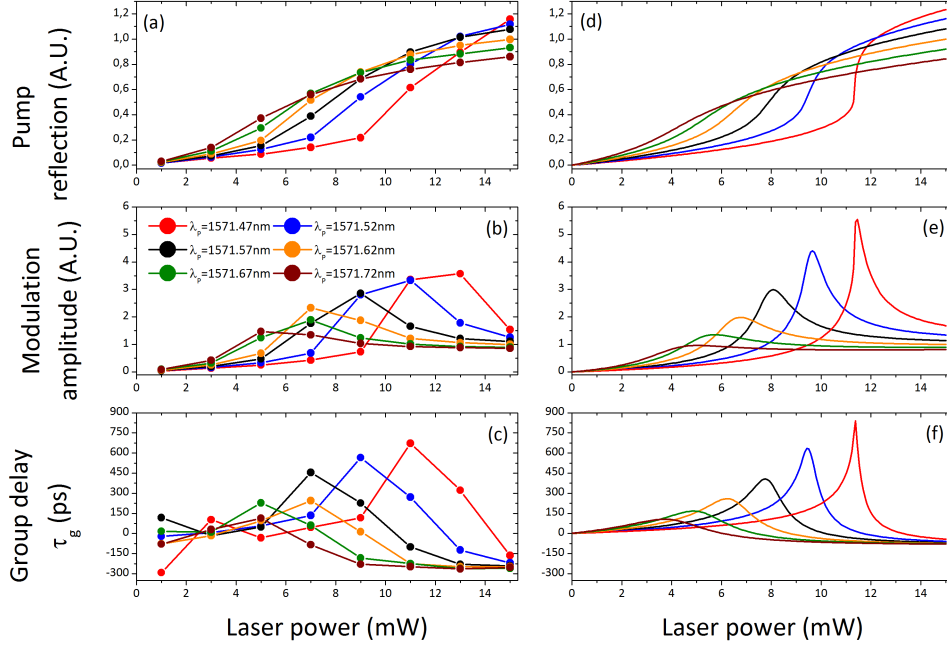


Figure 4.24: Measured pump (a), modulation amplitude (b) reflections and group delay (c) for $\delta = 240$ MHz and for different laser wavelengths as a function of the laser power. (d), (e) and (f) are the corresponding theoretical predictions.

itative agreement and quantitative agreement for the low frequencies and HWHM frequency.

The good qualitative and quantitative theory-experiment agreement for both temporal and spectral measurements, and the agreement between these two kinds of experiments, allows to unambiguously identify the physical mechanisms at the origin of the strong enhancement of the Q -factor, validating the theoretical model. As the pump power is increased the blue shifted resonance undergoes a strong distortion characteristic to the onset of bistable behavior [Yacomotti 2006a]. The stiff profile of the pump reflectivity and the phase shift, induce a steep reflectivity of the modulation amplitude and a strong dispersion as a precursor of the critical slowing down, which occurs above bistability. This effect adds-up to the CPO to strongly increase the cavity lifetime.

The full calculation gives a clear insight on the mechanism at play but CPO and nonlinear phase are intermingled and it is hard to identify their relative role. We thus come back to the simple and intuitive Fabry-Perot model (see chapter 3.2) predicting thus the group delay is:

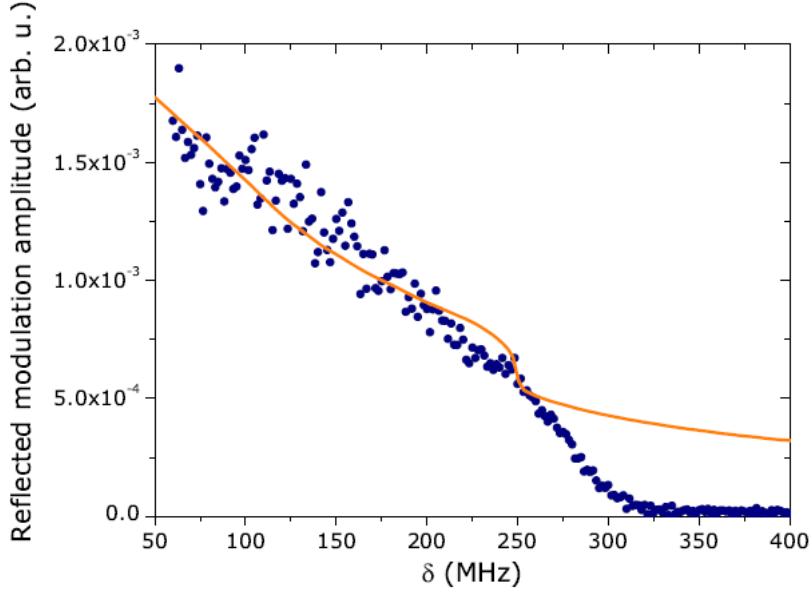


Figure 4.25: Measured modulation amplitude reflection under nonlinear interaction for a pump wavelength near the optimal wavelength λ_M and a power of 10 mW (\bullet). The corresponding theoretical prediction is represented by the line. Note that the calculation has been carried out using an input power of 11.7 mW.

$$\tau_g = \frac{2FLn}{\pi c} \left(1 + \Gamma \frac{n_g^{CPO} - n}{n} \right) \left[1 + \Gamma n_2 \kappa \Delta \omega \left(1 + \Gamma \frac{n_g^{CPO} - n}{n} \right) \right]$$

Figure 4.26 shows in red line the group delay normalized to $2\tau_l = 2Q_l\omega$, calculated using the Fabry-Perot model in the low Q -factor limit. The term $\kappa n_2 |A_p|^2$ in equation (3.31) is then neglected as the intracavity field and κ become weaker. The CPO group index is given by:

$$n_g = \frac{\alpha_0 c \tau_r}{2} \frac{s}{(1+s)^3},$$

where $s = P_p/P_{sat}$ and we assumed that $\delta \ll 1\tau_r$ in equation (1.10). The black squares (\blacksquare) represent the group delay obtained using the coupled mode theory model, section 3.3, when considering a cavity with $Q_l = 100$. All the other parameters are those used for figure 4.23. The black squares perfectly superpose with the red line showing that the nonlinear dispersion can be neglected in the coupled mode theory for $Q_l = 100$, revealing, thus, the bare CPO-induced group delay, which contributes to about a factor 2.6 to the overall group delay enhancement. The dashed black and dotted red lines in the inset are the group delays of figure 4.23 at respectively the maximum transmission of the pump and of the modulation amplitude reflections, corresponding to our experimental situation. They are calculated up to

$P_p/P_{sat} \simeq 0.3$ as for higher values the system becomes bistable. They show that the behavior of the group delay when measured at the pump reflection maxima is dominated by the CPO effect in the delay enhancement at low pump powers. At the maxima of the modulation amplitude reflectivities, corresponding to the steep variation of the pump reflection, the delay is an intertwinement of the CPO effect and the strong nonlinear dispersion.

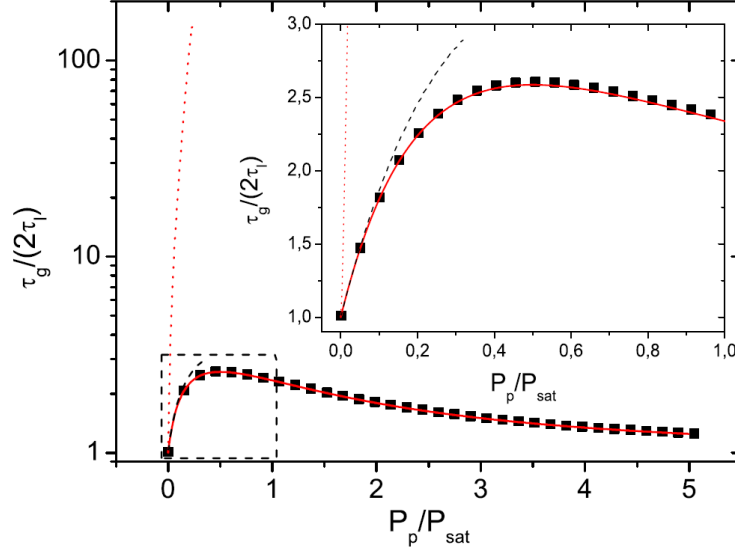


Figure 4.26: Group delay τ_g in units of $(2\tau_l)$ as a function of the intracavity pump power normalized to the saturation power. Red solid line: τ_g obtained using equation (3.31) and neglecting the nonlinear contribution. Black squares: τ_g obtained using equations (3.37) and (3.39) with $Q_l = 100$. Dashed black line (dotted red line): τ_g of figure 4.23 at the maxima of the pump (modulation amplitude) reflections. Inset: zoom of the dashed box.

In conclusion, it has been experimentally demonstrated that the Q -factor of a nanocavity can be dynamically and strongly enhanced by the cooperative use of CPO and dispersive nonlinearities. The numerical model developed in chapter 3 describes the experimental results. An agreement between the experimental measurements and the theoretical model has been showed. Their agreement also enables to predict the frequency pulling of the nanocavity resonance to the pump field. This effect was experimentally demonstrated and can be used to lock the enhanced Q -factor nanocavity to a desired wavelength. It can also be implemented to compensate for technological errors or to lock several nanocavities to the same wavelength. Additionally, the theoretical model also predicts signal amplification, an issue of great importance to compensate/overcome absorptive, diffusive and unavoidable nanocavity coupling losses; this has not been experimentally demonstrated but, anyhow, the measurements show hints that this effect could be present.

Part III

Slow light in photonic crystal waveguides

As discussed in chapter 1 and 2, slow light propagation is at the heart of intense research since two decades. Induced by nonlinear interactions, such as Electromagnetically Induced Transparency (EIT) [Fleischhauer 2005] or Coherent Population Oscillation (CPO), ultra slow light propagation was demonstrated in several systems including cold atoms [Boller 1991, Hau 1999, Inouye 2000], vapors [Kasapi 1995, Kash 1999], rare-earth doped crystals [Bigelow 2003a, Bigelow 2003b, Baldit 2005] and semiconductors [Ku 2004] (see chapter 1). These coherent nonlinear interactions induce a strong refractive index dispersion associated to a narrow spectral hole transparency in the absorption spectrum. This narrow window, related to the inverse of hyperfine coherence (EIT) or population (CPO) relaxation times, also determines the temporal accessible bandwidth. Coherent nonlinear interactions are thus particularly interesting to achieve extremely small group velocities that can be tuned by the absorption level or the light intensity.

An alternative avenue is also intensively explored to achieve slow light based on the moulding of the photonic dispersion diagram via the geometrical engineering of the optical properties. This is particularly the case in 2D Photonic Crystals (2D PhC) where slow light modes can be achieved both as Bloch states in non defective structures that act as distributed resonators and in defective 2D PhC where a missing row of holes created the so called W1 waveguides that can also host a slow mode [Baba 2008] (see chapter 2). In both cases the flat photonic band dispersion ($E(k)$) is designed by adjusting the opto-geometrical parameters in order to induce the slow group velocity ($dE(k)/dk$).

These two avenues were explored in parallel by teams coming from quite different backgrounds and that gained a clear cut intuition of the assets and limitations of their slow light approaches. Only recently the two approaches were started to be considered together generating both an increased interest and some controversies. For instance it is well known, from distributed feed-back lasers, that slow light propagation in an active medium periodically structured to induce the laser feed-back, subsequently generates an increasing of the absorption, implemented in such a case in order to increase the gain and achieve laser operation. Below the laser threshold, slow light can be obtained but the increase of the absorption imposes a severe limitation to the group velocity that can be achieved. In other words, it is now largely accepted that group index higher than 100 are hardly achievable in 2D PhC due to the strong increase of losses that follow at least a linear dependence on n_g . The highest experimental demonstration goes up to $n_g = 280$ [Vlasov 2005] at the expense of prohibitive losses. Conversely, ultra slow group velocities associated to v_g more than 5 orders of magnitude lower than c are currently achieved by EIT and CPO [Baldit 2005]. Moreover, here the optical transmission could be close to 100%, in spite of the extremely high group index. Clearly, in this case losses are independent of the group index and velocity. This apparent paradox is easily solved when considering the physical mechanisms at work in these qualitatively different approaches. The slow light originated by the material structuring is essentially associated to the time delay introduced by the increase of the propagation distance [Krauss 2007]. This increased path is at the hearth of the exaltation of

the light-matter linear and nonlinear interactions and thus generates the increase of the absorption and the additional losses [Mortensen 2007]. This is particularly the case in 2D PhC W1 where the slow light explores more efficiently the technological defects of the periodicity surrounding the WG core and losses due to technological imperfections become prohibitive in transparent or active 2D PhC. In turn, slow light by nonlinear interactions is not associated to the increase of the propagation distance and thus generates no additional loss. This discussion raises the question of benefiting from the assets of both approaches by combining in the same waveguide nonlinearly induced and geometrically engineered slow light.

Only few theoretical papers addressed such a combination. M. Soljačić and co-workers performed numerical calculations [Soljačić 2004, Soljačić 2005a] but, even though, they consider the possibility of slow mode waveguides for enhancing nonlinear effects when considering slow light from nonlinear origins, e.g. EIT, they combine it with PhC microcavities. More recently Mork and co-workers [Nielsen 2009] explicitly considered EIT interaction in the slow mode of a W1 waveguide and demonstrated that the combination of slow light by these two origins converges in a multiplication of the two independent group indexes regulated by the overlap of the optical mode and the active region. In a recent paper [Mørk 2010] the same team also considered the role of absorption and showed that it scales linearly with geometrically engineered group index but it does not have a dependence on nonlinear group index.

CPO differs from EIT by several aspects. In contrast to EIT, CPO does not allow to *burn* the spectral hole completely and to fully stop the propagating light. Nevertheless, its great interest is that there is no need of sophisticated 3-level system. Indeed, as we have seen in chapter 1, CPO could be implemented at room temperature in any 2-level or 2-level like system provided the population lifetime T_1 is sufficiently greater than the dephasing time T_2 . To the best of our knowledge no theoretical work has addressed the combination of CPO and geometrically induced slow light, which is the purpose of this part.

In chapter 5 we present a theoretical approach to the combination of slow light generated by the two means. As for the cavities, our approach is to start with the simplest and intuitive model and to increase the complexity to be closer to an actual experimental situation. We then first introduce a 1D model (5.1), next we develop a perturbative model (5.2) and compare the results with numerical computations (5.3). Chapter 6 presents and proposes a solution to the problem coupling light into a short high absorptive W1 PhC WG. We present tests using the lateral coupling (6.1). Next, we show functioning principle and theoretical calculations of the vertical coupler (6.2.1). Then we perform an experimental validation presenting also our first measures of slow light in PhC WGs (6.2.2). Finally, chapter 7 shows the first measurements on active W1 PhC WGs.

Theoretical studies

Contents

5.1	1D model	79
5.2	Perturbative model	84
5.2.1	Lorentz reciprocity theorem	85
5.2.2	First-order perturbation theory	86
5.3	Numerical simulations	89

In this chapter, theoretical studies on the combination of slow light by both means, material dispersion and structuring dispersion, are presented. In order to fully apprehend the consequences of the combination of slow light by both CPO effect and W1 PhC waveguide, we need to derive the total group index including the contributions of different origins. Since we are interested in implementing the coherent nonlinear interaction, we consider active 2D PhC close to the maximum of absorption. Consequently, 2D PhC technological imperfections are neglected since the absorption constitutes the dominant source of losses.

To gain intuition about the role of each effect and their link with losses we develop a simple 1D model (section 5.1). Next, a perturbative analytical model is presented (section 5.2). And finally, we compare the perturbative model results with numerical computations (section 5.3). Table 5.1 presents the different models specifying the advantages and disadvantages of each model.

	1D model	Perturbative model	Numerical computations
Interest	Simple approach	Analytical model	Validation
Analytical expressions	NO	YES	NO

Table 5.1: Characteristics of the different models.

5.1 1D model

To gain intuition about the role of slow light induced by the dispersive properties of the CPO effect in a W1 PhC waveguide, we develop in this first approach a simple unidimensional (1D) model where light propagates, as shown in figure 5.1,

along the axis x , in a medium having a periodic index variation. In this approach, the wavevector of the propagating mode is calculated including the CPO effect and the dispersion relation is deduced. In fact, our approach is valid for any physical phenomenon that induces, as the CPO effect, a strong dispersion of the index of refraction which is quantified by a group index, labeled in the following n_g^L . In this 1D model, we also consider that an absorption α_0 is initially present in the medium and constitutes the only source of losses.

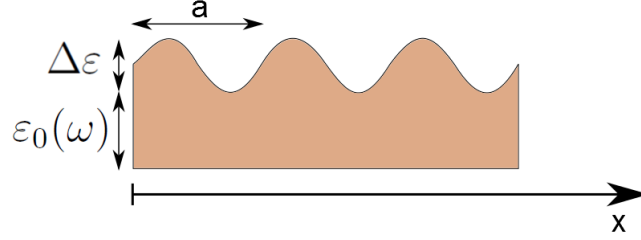


Figure 5.1: Sketch of the periodic sinusoidal grating for the unidimensional model.

In this approach, we essentially follow the introduction of Sakoda's book on Photonic Crystals [Sakoda 2005], further including a frequency dependence of the dielectric constant and an absorption α_0 . The wave equation describing the evolution of the electric field in the 1D medium is:

$$\frac{\partial^2 E(x, \omega)}{\partial x^2} + \frac{\omega^2 \varepsilon(x, \omega)}{c^2} E(x, \omega) = 0 \quad (5.1)$$

where ε is the relative permittivity, which is periodic in space: $\varepsilon(x + a, \omega) = \varepsilon(x, \omega)$. ε is considered as a complex number to include the absorption and is frequency dependent in order to account for dispersive phenomena, such as the CPO effect. For simplicity, we consider that the relative permittivity has a sinusoidal modulation along the propagation axis x as depicted in figure 5.1. The permittivity can be then expressed as:

$$\varepsilon(x, \omega) = \varepsilon_0(\omega) + \Delta\varepsilon e^{\frac{i2\pi}{a}x} + \Delta\varepsilon e^{\frac{-i2\pi}{a}x}, \quad (5.2)$$

where $\Delta\varepsilon$ and a are respectively the amplitude and the period of the permittivity modulation along the x -axis. According to Bloch theorem, a typical solution of equation (5.1) can be written as:

$$E(x, \omega) = u_k(x, \omega) e^{ikx},$$

with $u_k(x, \omega)$ is a periodic function, $u_k(x + a, \omega) = u_k(x, \omega)$. By expanding u_k in Fourier series, we obtain:

$$E(x, \omega) = \sum_{m=-\infty}^{\infty} u_m e^{i(k + \frac{2\pi}{a}m)x}. \quad (5.3)$$

Substituting expressions (5.2) and (5.3) into equation (5.1), we get:

$$u_m = -\frac{\frac{\omega^2}{c^2}(\Delta\varepsilon u_{m-1} + \Delta\varepsilon u_{m+1})}{\frac{\omega^2\varepsilon_0(\omega)}{c^2} - \left(k + \frac{2\pi m}{a}\right)^2}. \quad (5.4)$$

A further simplification is achieved by considering a propagation close to the first order photonic crystal bandgap where $k \simeq \pi/a$. We can write then $|k - 2\pi/a| \simeq k$. Thus, the two dominant coefficients of the Fourier series are u_0 and u_{-1} provided that $\frac{\omega^2}{c^2}\varepsilon_0(\omega) \simeq k^2$. Note that the coefficients u_0 and u_{-1} are the amplitudes of the forward and backward waves of the Bloch mode respectively. In order to calculate the overall group index and the absorption of the system, we consider a small variation of the wavevector k , so that $k = k_0 + \Delta k$, with $k_0 = \pi/a$. The Fourier development given by equation (5.3) considerably simplifies and reduces the field expression to only two Fourier components: the propagative and the counter-propagative modes, so

$$E(x, t) = u_0 e^{i(k_0 + \Delta k)x - \omega t} + u_{-1} e^{-i(k_0 - \Delta k)x - \omega t}.$$

Therefore, two coupled equations for u_0 and u_{-1} can be obtained from relation (5.4):

$$\begin{aligned} \left[\frac{\omega^2}{c^2}\varepsilon_0(\omega) - k_0^2 - 2\Delta k k_0 \right] u_0 + \frac{\omega_0^2}{c^2}\Delta\varepsilon u_{-1} &= 0 \\ \frac{\omega_0^2}{c^2}\Delta\varepsilon u_0 + \left[\frac{\omega^2}{c^2}\varepsilon_0(\omega) - k_0^2 + 2\Delta k k_0 \right] u_{-1} &= 0 \end{aligned} \quad (5.5)$$

where, once more, we have only kept first order terms in Δk and $\Delta\omega$ ($\omega = \omega_0 + \Delta\omega$).

In order to go further with the calculations, it is necessary at this stage to explicitly give an expression for the permittivity of the system starting from the index of refraction and the absorption. The refractive index is simply given by [Soljačić 2005a]:

$$n(\omega) = n_0 + \frac{\Delta\omega}{\omega_0} (n_g^L - n_0), \quad (5.6)$$

where n_0 is the effective index of refraction of the medium and $\omega_0 = ck_0/n_0$. As mentioned before, n_g^L is the group index associated with the dispersive phenomenon such as the CPO effect. Equation (5.6) has a linear dependance with respect to $\Delta\omega$ and is valid only for small detunings $\Delta\omega \ll \omega_0$. It is worth noting that the slope of the linear equation (5.6) is proportional to the group index n_g^L . Then, the permittivity reads:

$$\varepsilon_0(\omega) = \left[n(\omega) + i \frac{\alpha_0 n(\omega)}{2k_0} \right]^2 \simeq n^2(\omega) \left(1 + i \frac{\alpha_0}{k_0} \right), \quad (5.7)$$

where we neglected the second order absorption term. Using (5.7) in (5.5) and neglecting the terms containing $\Delta\omega\alpha_0$ we obtain:

$$\begin{aligned} \left[\frac{\Delta\omega}{v_g^L} - \Delta k + i\frac{\alpha_0}{2} \right] u_0 + hu_{-1} &= 0 \\ hu_0 + \left[\frac{\Delta\omega}{v_g^L} + \Delta k + i\frac{\alpha_0}{2} \right] u_{-1} &= 0, \end{aligned} \quad (5.8)$$

where $h \equiv \frac{\omega_0^2 \Delta \varepsilon}{2c^2 k_0} = \frac{\pi \Delta \varepsilon}{2an_0^2}$ is called the distributed feedback factor which couples the forward and the backward waves through the first order diffraction.

Solutions of (5.8) give the dispersion relation $\Delta\omega(\Delta k)$ close to the first order gap. These are readily obtained by setting the determinant of (5.8) to zero:

$$\left(\frac{\Delta\omega}{v_g^L} + i\frac{\alpha_0}{2} \right)^2 = \Delta k^2 + h^2 \quad (5.9)$$

Now, in order to obtain stationary solutions, $\Delta\omega$ must be real, therefore we can easily compute the real and imaginary parts of the wavevector from (5.9) as:

$$\begin{aligned} \Delta k' &= \pm \Re \left[\sqrt{\left(\frac{\Delta\omega}{v_g^L} + i\frac{\alpha_0}{2} \right)^2 - h^2} \right] \\ \Delta k'' &= \pm \Im \left[\sqrt{\left(\frac{\Delta\omega}{v_g^L} + i\frac{\alpha_0}{2} \right)^2 - h^2} \right] \end{aligned} \quad (5.10)$$

It is worth noting here that in the absence of absorption ($\alpha_0 = 0$) and when the medium has no permittivity modulation ($h = 0$), we retrieve from equation (5.9) that light propagates in the medium at the group velocity v_g^L imposed by the index dispersion due to nonlinear phenomenon.

Figure 5.2 shows the solutions of the real part of the wavevector (equation 5.10) for $h = k_0/10$, $n_g^L = 3$ and for different absorptions ($\alpha_0 = 0, 50, 200 \text{ cm}^{-1}$).

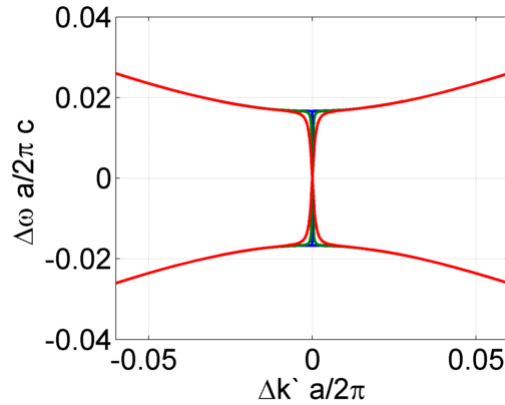


Figure 5.2: Dispersion relation (band diagram) at the first bandgap for $\alpha_0 = 0$ (blue), $\alpha_0 = 50 \text{ cm}^{-1}$ (green) and $\alpha_0 = 200 \text{ cm}^{-1}$ (red).

It is clear from figure 5.2 that in the presence of absorption the band diagram is modified. For instance, there is no longer a *strictly true bandgap*. This is particularly important as in this case the group index (n_g^{TOT}), proportional to the derivative $d\omega/dk$ and which can be deduced from figure 5.2, does not diverge.

Figure 5.3(top) shows the evolution of the group index deduced from the dispersion relation when the group n_g^L is changed (figure 5.3.a: $n_g^L = 3$, 5.3.b: $n_g^L = 10$ and 5.3.c: $n_g^L = 30$) and $h = 0.1k_0$ remains constant. Figure 5.3(bottom) shows the corresponding absorption proportional to the imaginary part of the wavevector given by equation 5.10. The blue, green and red curves correspond respectively to an absorption $\alpha_0 = 0$, $\alpha_0 = 50 \text{ cm}^{-1}$ and $\alpha_0 = 200 \text{ cm}^{-1}$.

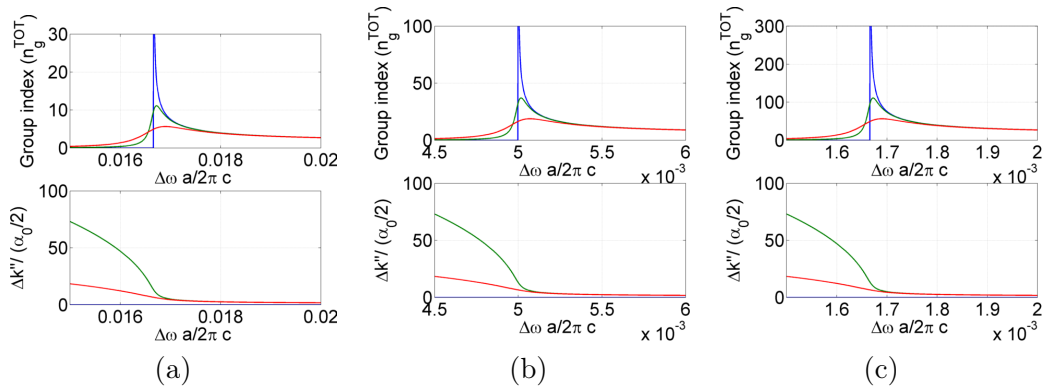


Figure 5.3: Top: group index (n_g^{TOT}) as a function of the frequency for $\alpha = 0$ (blue), $\alpha = 50 \text{ cm}^{-1}$ (green) and $\alpha = 200 \text{ cm}^{-1}$ (red). Bottom: enhancement of the distributed absorption losses due to the structuration as a function of frequency for $\alpha = 50 \text{ cm}^{-1}$ (green) and $\alpha = 200 \text{ cm}^{-1}$ (red). For: $h = 0.1k_0$ and (a) $n_g^L = 3$, (b) $n_g^L = 10$ and (c) $n_g^L = 30$.

We see that for a given absorption the group index increases with n_g^L , whereas the overall losses remains constant. It is important to emphasize here the fact that the slowing down induced by the dispersive phenomenon, such the CPO effect for example, increases the group index without adding additional losses.

This is unlike modifying the group index by changing the geometry of the modulated medium. Indeed, this is shown in figure 5.4, similar to figure 5.3, where this time the group index $n_g^L = 10$ is kept constant and where h is varied (figure 5.4.a: $h = 0.01k_0$, 5.4.b: $h = 0.05k_0$ and 5.4.c: $h = 0.1k_0$). The h factor can be changed by changing the period a or the modulation depth of the permittivity $\Delta\varepsilon$, two geometrical properties of the medium. For a given absorption, the deeper is the modulation the higher is the overall group index. However in contrast with the previous case, the losses also are increased.

These first results already highlight the fact that increasing the group index of a medium with a periodic modulation of the refractive index impacts differently whether it is caused by a coherent optical effect or by the geometrical engineering of the medium structuration. Indeed, in coherent effect case the losses remain

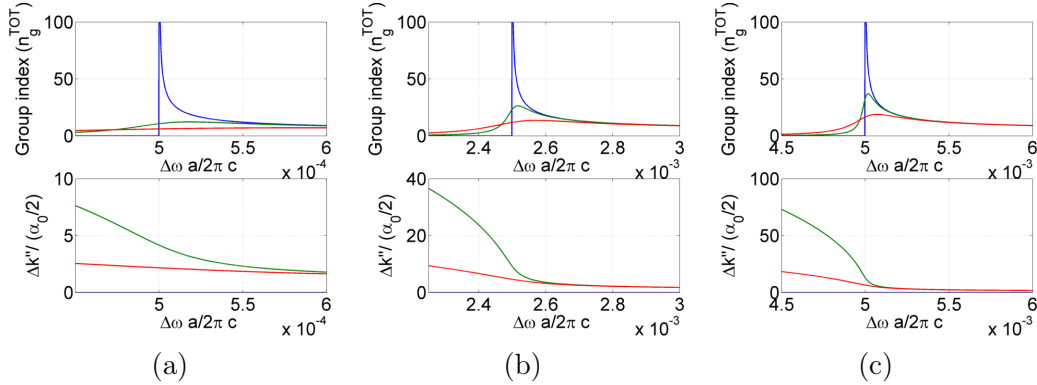


Figure 5.4: Top: group index (n_g^{TOT}) as a function of the frequency for $\alpha = 0$ (blue), $\alpha = 50 \text{ cm}^{-1}$ (green) and $\alpha = 200 \text{ cm}^{-1}$ (red). Bottom: enhancement of the distributed absorption losses due to the structuration as a function of frequency for $\alpha = 50 \text{ cm}^{-1}$ (green) and $\alpha = 200 \text{ cm}^{-1}$ (red). For: $n_g^L = 10$ and (a) $h = 0.01k_0$, (b) $h = 0.05k_0$ and (c) $h = 0.1k_0$.

constant, whereas for the geometrical engineering case, the losses goes growing with the overall group index. In the case of a coherent interaction, when the group index n_g^L is increased through the steep dispersion, the light propagates slowly over a distance L in the medium feeling the same amount of losses independently on how slow it is. In the case where the overall group index is increased geometrically through the h factor, the coupling between the propagative and counter-propagative modes is strengthen. As a consequence, the light instead of propagating following a rectilinear trajectory, it goes back and forth over single or multiple periods a . The light then propagates over a length much longer than the real length L of the medium, and feels thus additional losses.

In summary, this simple 1D model has allowed to show that the imaginary part of k (distributed losses) is increased due to the increased trajectory induced by the periodical structuration, but it is not modified when changing the background group velocity, for instance by means of CPO.

5.2 Perturbative model

In this section, we develop a perturbative 3D model considering a periodic waveguide along the z -direction. This work has been made in collaboration with P. Lalanne and C. Sauvan at Institut d'Optique. The cross-section in the (x, y) plane is arbitrary. The materials can be absorptive, dispersive or anisotropic and the system is characterized by the permittivity and permeability tensors $\varepsilon(\mathbf{r})$ and $\mu(\mathbf{r})$. The sole assumption is that the materials are reciprocal, $\mu = \mu^T$ and $\varepsilon = \varepsilon^T$, where the superscript denotes matrix transposition. The electromagnetic field $(\mathbf{E}_m^{(0)}, \mathbf{H}_m^{(0)})$ of the waveguide modes at the frequency ω (we have adopted the $e^{-i\omega t}$ time-dependence for the fields) is solution of Maxwell's equations in the absence of source,

$$\begin{aligned}\nabla \times \mathbf{E}_m^{(0)} &= i\omega\mu(\mathbf{r})\mathbf{H}_m^{(0)}, \\ \nabla \times \mathbf{H}_m^{(0)} &= -i\omega\varepsilon(\mathbf{r})\mathbf{E}_m^{(0)}.\end{aligned}\tag{5.11}$$

Since the waveguide is periodic along the z -direction, Bloch's theorem allows us to write

$$\begin{aligned}\mathbf{E}_m^{(0)}(x, y, z) &= \mathbf{e}_m^{(0)}(x, y, z)e^{ik_m^{(0)}z}, \\ \mathbf{H}_m^{(0)}(x, y, z) &= \mathbf{h}_m^{(0)}(x, y, z)e^{ik_m^{(0)}z},\end{aligned}\tag{5.12}$$

where the mode profiles $\mathbf{e}_m^{(0)}(x, y, z)$ and $\mathbf{h}_m^{(0)}(x, y, z)$ are periodic in the z -direction with the same period a as the waveguide.

A small periodic perturbation of the dielectric permittivity, $\varepsilon \rightarrow \varepsilon + \Delta\varepsilon$, modifies the waveguide modes, which are now given by

$$\begin{aligned}\nabla \times \mathbf{E}_m &= i\omega\mu(\mathbf{r})\mathbf{H}_m, \\ \nabla \times \mathbf{H}_m &= -i\omega[\varepsilon(\mathbf{r}) + \Delta\varepsilon(\mathbf{r})]\mathbf{E}_m.\end{aligned}\tag{5.13}$$

This way, we have written the Maxwell equations for both, the perturbed and unperturbed system. We assumed that the perturbation has the same periodicity as the waveguide, so that the modes of the perturbed waveguide are still Bloch modes,

$$\begin{aligned}\mathbf{E}_m(x, y, z) &= \mathbf{e}_m(x, y, z)e^{ik_m z}, \\ \mathbf{H}_m(x, y, z) &= \mathbf{h}_m(x, y, z)e^{ik_m z}.\end{aligned}\tag{5.14}$$

In the following, we derive the new propagation constant $k_m(\omega)$. For that purpose we use perturbation theory to calculate the first-order modification of the propagation constant as a function of the unperturbed mode. We first derive Lorentz reciprocity theorem [Snyder 1983] between unperturbed and perturbed modes before applying perturbation theory in a second step.

5.2.1 Lorentz reciprocity theorem

Figure 5.5 (left) shows an unperturbed mode propagating toward $z > 0$, $(\mathbf{E}_m^{(0)+}, \mathbf{H}_m^{(0)+}, k_m^{(0)})$ and figure 5.5 (right) shows a perturbed mode propagating toward $z < 0$, $(\mathbf{E}_n^-, \mathbf{H}_n^-, -k_n)$ at the same frequency ω .

By applying the divergence theorem, $\iiint_V \vec{\nabla} \cdot \vec{F} dr^3 = \oint_{\Sigma} \vec{F} \cdot d\vec{S}$, to the vector $\mathbf{F} = \mathbf{E}_n^- \times \mathbf{H}_m^{(0)+} - \mathbf{E}_m^{(0)+} \times \mathbf{H}_n^-$ and noting that from equations (5.11) and (5.13) $\nabla \cdot \mathbf{F} = -i\omega\mathbf{E}_m^{(0)+} \cdot \Delta\varepsilon\mathbf{E}_n^-$, we obtain

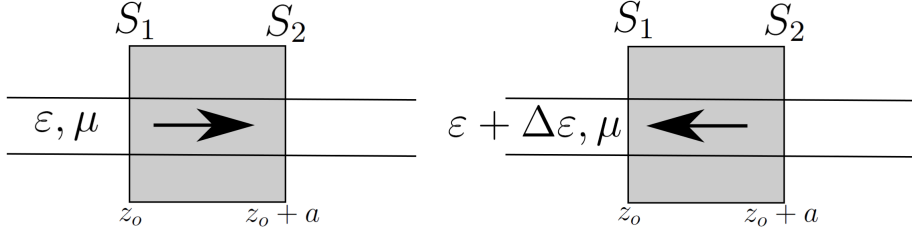


Figure 5.5: Sketch of the system of study for the perturbative model. Left, unperturbed propagative mode; right, perturbed counter-propagative

$$\iint_{\Sigma} (\mathbf{E}_n^- \times \mathbf{H}_m^{(0)+} - \mathbf{E}_m^{(0)+} \times \mathbf{H}_n^-) \cdot d\mathbf{S} = -i\omega \iiint_V \mathbf{E}_m^{(0)+} \cdot \Delta\epsilon \mathbf{E}_n^- d^3\mathbf{r}, \quad (5.15)$$

where Σ denotes a closed surface that encloses the volume V . As shown in figure 5.5, we consider a cylindrical closed surface formed by the cross-section planes $z = z_0$ and $z = z_0 + a$ that extends to infinity in the (x, y) plane. With this choice, the surface integral on the left-hand side of equation (5.15) can be decomposed into two surface integrals that run over the waveguide cross-section at $z = z_0$ and $z = z_0 + a$ and a third integral over the lateral surface of the cylinder that vanishes since the fields of the Bloch guided modes are assumed to be zero at infinity. Because the waveguide modes are Bloch modes, see equations (5.12) and (5.14), we have $\mathbf{F}(x, y, z_0 + a) = \mathbf{F}(x, y, z_0) e^{i(k_m^{(0)} - k_n)a}$ and Lorentz reciprocity theorem becomes

$$\begin{aligned} \left[1 - e^{i(k_m^{(0)} - k_n)a}\right] \iint_S (\mathbf{E}_n^- \times \mathbf{H}_m^{(0)+} - \mathbf{E}_m^{(0)+} \times \mathbf{H}_n^-) \cdot \mathbf{u}_z dS = \\ i\omega \iiint_V \mathbf{E}_m^{(0)+} \cdot \Delta\epsilon \mathbf{E}_n^- d^3\mathbf{r}, \end{aligned} \quad (5.16)$$

where S is the waveguide cross-section at $z = z_0$ and \mathbf{u}_z is a unitary vector of space in the z -direction.

5.2.2 First-order perturbation theory

Since the permittivity modification $\Delta\epsilon$ is small compared to ϵ , we use the first-order perturbation theory to derive the modification of the propagation constant $k_m - k_m^{(0)}$. We introduce a small dimensionless parameter $x \ll 1$ defined as

$$\epsilon + \Delta\epsilon = \epsilon + x\Delta\hat{\epsilon}, \quad (5.17)$$

and we develop the perturbed propagation constant and the perturbed fields in power series of x ,

$$k_m = k_m^{(0)} + xk_m^{(1)} + \dots \quad (5.18)$$

$$\mathbf{E}_m = \mathbf{E}_m^{(0)} + x\mathbf{E}_m^{(1)} + \dots \quad (5.19)$$

$$\mathbf{H}_m = \mathbf{H}_m^{(0)} + x\mathbf{H}_m^{(1)} + \dots \quad (5.20)$$

In the following, we restrict ourselves to the first-order perturbation.

We now introduce the expansions (5.18), (5.19) and (5.20) in the expression of Lorentz reciprocity theorem in equation (5.16) applied to the same mode ($m = n$). By expanding the exponential function, we get, up to the first order in x

$$\begin{aligned} ixk_m^{(1)} a \iint_S (\mathbf{E}_m^{(0)-} \times \mathbf{H}_m^{(0)+} - \mathbf{E}_m^{(0)+} \times \mathbf{H}_m^{(0)-}) \cdot \mathbf{u}_z dS = \\ ix\omega \iiint_V \mathbf{E}_m^{(0)+} \cdot \Delta\hat{\varepsilon}\mathbf{E}_m^{(0)-} d^3\mathbf{r}, \end{aligned} \quad (5.21)$$

This relation evidences that we can calculate the first-order modification of the propagation constant as a function of the known field of the unperturbed mode. If we note $\Delta k = xk_m^{(1)}$ the first-order perturbation, equation (5.21) straightforwardly leads to

$$\Delta k = \frac{\omega}{a} \frac{\iiint_V \mathbf{E}_m^{(0)+} \cdot \Delta\varepsilon\mathbf{E}_m^{(0)-} d^3\mathbf{r}}{\iint_S (\mathbf{E}_m^{(0)-} \times \mathbf{H}_m^{(0)+} - \mathbf{E}_m^{(0)+} \times \mathbf{H}_m^{(0)-}) \cdot \mathbf{u}_z dS}. \quad (5.22)$$

It is interesting to introduce the group velocity $v_g^{(0)} = d\omega/dk_m^{(0)}$ of the unperturbed mode in this expression. The group velocity of a guided Bloch mode can be expressed as [Lecamp 2007]

$$\iint_S (\mathbf{E}_m^{(0)-} \times \mathbf{H}_m^{(0)+} - \mathbf{E}_m^{(0)+} \times \mathbf{H}_m^{(0)-}) \cdot \mathbf{u}_z dS = \frac{2v_g^{(0)}}{a} \iiint_V \mathbf{E}_m^{(0)+} \cdot \varepsilon\mathbf{E}_m^{(0)-} d^3\mathbf{r}, \quad (5.23)$$

and inserting equation (5.23) into equation (5.22) leads to:

$$\boxed{\Delta k = \frac{\omega}{2v_g^{(0)}} \frac{\iiint_V \mathbf{E}_m^{(0)+} \cdot \Delta\varepsilon\mathbf{E}_m^{(0)-} d^3\mathbf{r}}{\iiint_V \mathbf{E}_m^{(0)+} \cdot \varepsilon\mathbf{E}_m^{(0)-} d^3\mathbf{r}}}. \quad (5.24)$$

This result is general and applies to any periodic waveguide and to any perturbation $\Delta\varepsilon$.

We now assume that (1) the waveguide permittivity and the perturbation are isotropic, (2) the waveguide is non-absorbing (ε is real and $\mathbf{E}_m^{(0)-} = \mathbf{E}_m^{(0)+*}$) and (3) the perturbation is either zero or a constant. With these assumptions and by introducing the refractive index perturbation Δn , $\Delta\varepsilon \simeq 2\varepsilon\Delta n/n$, equation (5.24) becomes

$$\Delta k = k_0 n_g^{(0)} \Gamma \frac{\Delta n}{n} \quad (5.25)$$

where $k_0 = \omega/c$, $v_g^{(0)} = c/n_g^{(0)}$ and Γ is the normalized overlap of the unperturbed mode with the perturbation,

$$\Gamma = \frac{\iiint_P \varepsilon |\mathbf{E}_m^{(0)}|^2 d^3\mathbf{r}}{\iiint_V \varepsilon |\mathbf{E}_m^{(0)}|^2 d^3\mathbf{r}}, \quad (5.26)$$

with P the volume where the perturbation stands ($\Delta\varepsilon \neq 0$).

Group Index We can now derive the total group index as the derivative of the perturbed wave vector:

$$n_g^{TOT} = c \frac{dk}{d\omega} = c \frac{dk_m^{(0)}}{d\omega} + c \frac{d\Delta k}{d\omega} = n_g^{(0)} + c \frac{d\Delta k}{d\omega} \quad (5.27)$$

and from equation 5.25, it results:

$$\frac{d\Delta k}{d\omega} = \frac{\Gamma}{v_g^{(0)}} \frac{d}{d\omega} \left(\omega \frac{\Delta n}{n} \right) \quad (5.28)$$

where we have considered that the structuration group index $n_g^{(0)}$ and Γ are constant since the spectral interval where $\Delta n \neq 0$ is small. We now use $\Delta n = n - n_0$ then

$$\frac{d\Delta k}{d\omega} = \frac{\Gamma}{v_g^{(0)}} \frac{d}{d\omega} \left[\omega n_0 \left(\frac{n}{n_0} - 1 \right) \right] = \frac{\Gamma}{v_g^{(0)}} \left(\frac{n_g^{CPO}}{n_0} - 1 \right), \quad (5.29)$$

where n corresponds to the index of the material taking into account the dispersion generated by CPO effect. We now replace the expression obtained in (5.29) in (5.27)

$$n_g^{TOT} = c \frac{dk}{d\omega} = n_g^{(0)} + \Gamma \frac{c}{v_g^{(0)}} \left(\frac{n_g^{CPO}}{n_0} - 1 \right).$$

This way the total group index resulting from the combination of nonlinear dispersion (CPO) and geometrical structuration (PhC) reads:

$$\boxed{n_g^{TOT} = n_g^{(0)} \left[1 + \Gamma \left(\frac{n_g^{CPO}}{n_0} - 1 \right) \right]} \quad (5.30)$$

Absorption We can also calculate the total absorption of the system, for this we need to consider the imaginary part of the propagation constant $\Im k$, indeed absorption (α) is defined as:

$$\alpha = 2\Im k$$

We can assume that the imaginary part comes from the *perturbative* contribution, Δk . Using (5.25), we can then obtain the total absorption:

$$\boxed{\alpha^{TOT} = \alpha^{CPO} \Gamma \frac{n_g^{(0)}}{n_0}} \quad (5.31)$$

where α^{CPO} is the absorption given by relation (1.9).

Looking at the equation 5.31 a clear difference between slow light from structuration and from nonlinear effects pops up: while an enhancement of group index by means of the structuration induces also an increase of the absorption of the system, the group index enhancement via the CPO effect does not enhance the absorption which is even reduced (as shown in chapter 1). Also, it is important to highlight the fact that the increase of the absorption is not due to the enhancement of interaction time as claimed in [Mortensen 2007]; this is a straightforward deduction from the fact that slowing down by CPO effect does not involve such enhancement of the light matter interaction, but only increases the propagation time. As already discussed, the absorption is increased due to the increase of interaction length produced by the periodical structuration.

5.3 Numerical simulations

To evaluate the validity of the model developed in the previous section, we make the exact numerical simulations using the Bloch mode solver developed at the Institut d'Optique [Lalanne 2002] (numerical simulations were performed at Institut d'Optique Graduate School by Christophe Sauvan), in the particular situation of 2D photonic crystal waveguide.

The numerical calculations are made using the properties of the 2D photonic crystal waveguide designed and fabricated at LPN for the experimental demonstrations: period $a = 420$ nm, hole radius $r = 125$ nm, thickness $e = 265$ nm, material refraction index $n = 3.16$ and effective index $n_{\text{eff}} = 3.31$. We also set a constant absorption $\alpha_0 = 100 \text{ cm}^{-1}$ of the active medium (quantum wells), with a carriers recombination time $T_1 = 200$ ps and a dephasing time $T_2 = 10$ ps. The numerical calculations were performed for 3 different wavelengths $\lambda = 1550, 1560$ and 1561.5 nm, each of which corresponds to a different group index $n_g^{PhC} = 13, 53$, and 100 . The normalized overlap of the unperturbed mode with the perturbation (quantum wells) are respectively $\Gamma = 0.292, 0.29$, and 0.2891 .

In figures 5.6, 5.7 and 5.8 we show the comparison between the results obtained using the perturbative model for the group index and the absorption (equations (5.30) and (5.31)), and the exact numerical calculations.

Figures 5.6, 5.7 and 5.8 show a quite good agreement between both results providing a validation for the perturbative model. However, we can notice that when the group index is high, there is a slight disagreement.

In conclusion, we developed two simple models that allows to predict slow light in a system where we combine group index and absorption coming from two different origins, nonlinear effect and periodical structuration. Both models show that the

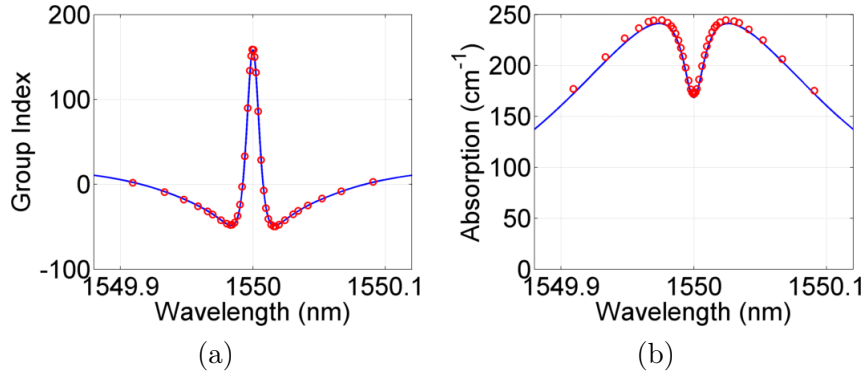


Figure 5.6: Graphics of the group index (a) and the absorption (b) as a function of the wavelength comparing perturbative results (blue line) and exact numerical calculations (\circ) at $\lambda = 1550$ nm and then a photonic crystal group index $n_g^{PhC} = 13$. Numerical simulations were performed at *Institut d'Optique* by Christophe Sauvan.

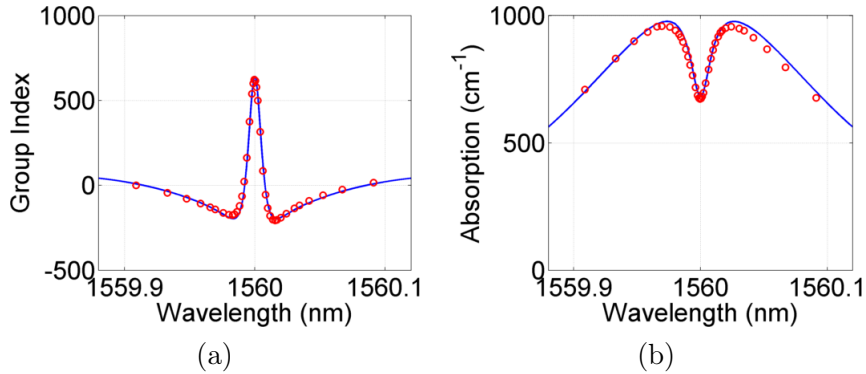


Figure 5.7: Graphics of the group index (a) and the absorption (b) as a function of the wavelength comparing perturbative results (blue line) and exact numerical calculations (\circ) at $\lambda = 1560$ nm and then a photonic crystal group index $n_g^{PhC} = 53$. Numerical simulations were performed at *Institut d'Optique* by Christophe Sauvan.

total group index has a linear dependence with each group index. Regarding the absorption, it must be said that differences between both slow light origin arises: while structuration group index increases linearly the absorption, CPO-induced group index does not contribute to the modification of the absorption.

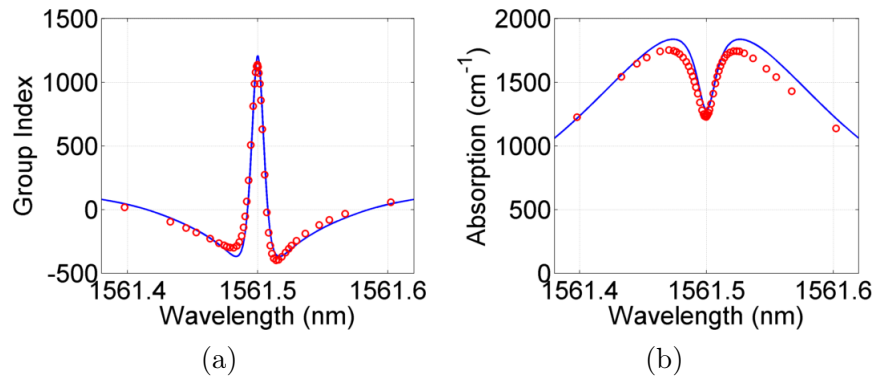


Figure 5.8: Graphics of the group index (a) and the absorption (b) as a function of the wavelength comparing perturbative results (blue line) and exact numerical calculations (\circ) at $\lambda = 1561.5$ nm and then a photonic crystal group index $n_g^{PhC} = 100$. Numerical simulations were performed at *Institut d'Optique* by Christophe Sauvan.

Coupling into a W1 waveguide

Contents

6.1 Lateral coupling	94
6.1.1 Sample fabrication	95
6.1.2 Cleaving process	97
6.2 Vertical coupling	98
6.2.1 Theoretical calculations	99
6.2.2 Experimental validation of the coupler and measurement of the group index	105
6.3 Conclusion	114

We will now consider the experimental aspects associated to the predictions of chapter 5. As we will see, coupling light to an absorptive short nano-waveguide is a difficult task. The aim of this chapter is to propose and study a vertical (to the periodicity) coupling strategy.

Coupling into W1 waveguides (WGs) is a challenging issue as generally a light beam of few micrometers diameter has to be injected in the rectangular cross-section of the W1 PhC WG of few square nanometers. There are different approaches that can be used to overcome this difficulty. Various types of matching systems have shown the ability for a good coupling between waveguides (ridge or PhCW in *standard* regime) and slow-light PhCWs [Talneau 2008, Hugonin 2007, Vlasov 2006]. Several solutions such as tapered-fiber evanescent couplers [Barclay 2003, Lee 2008], adiabatic mode convertor couplers [McNab 2003, Notomi 2004] and grating based couplers [Taillaert 2002, Van Laere 2007] have proven to be very efficient for coupling with very low insertion loss (1dB) and typical coupling efficiency reaching values up to 60%. These approaches have shown to be efficient, however, it requires long propagation distances (\sim mm). When working in passive waveguides, this is not an issue since losses in the ridge waveguides are negligible compared to coupling and propagation losses in the W1. On the other hand, and more particularly for the studies reported in this thesis, it is necessary to reduce the propagation lengths since the CPO effect requires absorptive QWs embedded in the waveguide.

Another issue that must be considered, besides the geometrical coupling aspects, is the coupling to the slow mode of the W1 PhC WG. This problem has been widely studied in the past [Hugonin 2007, Vlasov 2006] and the solution is basically to use a W1 access waveguide with a modified period, where the slow mode (in the unmodified waveguide) propagates with low group index (\sim 5).

In this chapter, we first present our initial, naive, attempt to couple light into the W1 PhC WG directly from free space (butt coupling). Then we present an original proposal based on the vertical coupling through a region where the period of the lattice and radius of the holes of the PhC is modulated. This produces a folding of the photonic band which allows vertical coupling. At last, an experimental validation of this technique is presented.

6.1 Lateral coupling

The most simple approach to couple light into a waveguide is the butt coupling. This is done by cleaving the PhC W1 waveguide on both sides, input and output, and coupling the light directly into it directly after focusing the free space propagative beam. Though this approach is very simple, the efficiency of this type of coupling has a strong dependence on the group index of the waveguide. Indeed, the lower is the group index, the higher the coupling efficiency will be. To maximize the coupling an intermediate low group index region is then suitable.

Figure 6.1 shows a typical W1 waveguide arrangement consisting of a high group index waveguide, called *slow-waveguide*, sandwiched between two low group index waveguides called *fast-waveguides*. Following the work in [Hugonin 2007], this arrangement allows optimizing the coupling through the fast waveguide into the slow waveguide under investigation. The *slow-waveguide* consists of a W1 waveguide obtained in a triangular lattice photonic crystal with period a . The *fast-waveguide* has the same lattice structure, however the period a' in the propagation direction is slightly increased with respect to a .

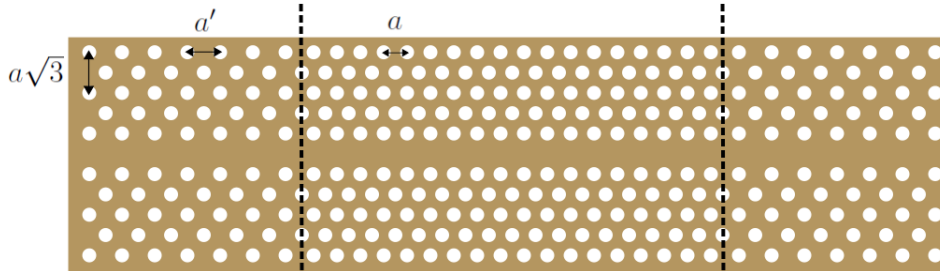


Figure 6.1: Sketch of sample to cleave on both ends consisting of *fast waveguides* at the ends and *slow waveguides* in the center

Figures 6.2 (a) and (b) show respectively the calculated dispersion curves and the group index of the *fast and slow waveguides* as a function of the wavelength for the following set of parameters: $n = 3.31$ is the refractive index of the material, $a = 420$ nm, $a' = 440$ nm, $r = 125$ nm is the radius of the holes, and $e = 265$ nm is the thickness of the membrane. Figure 6.2.c represents the transmission from the fast to the slow waveguide calculated with the 3D fully-vectorial Bloch-modal method in [Lecamp 2007]. As an example, when working at $\lambda = 1560$ nm, the group index in the *fast and slow waveguide* are respectively $n_g = 5$ and $n_g = 50$, whereas

the transmission from the fast to the slow waveguide is as high as 95%.

It is then more efficient to couple light into the structure depicted in figure 6.1, going from air with unity index of refraction to the *fast-waveguide* with a group index of about $n_g = 5$, than directly to the *slow-waveguide* having a high group index, for which the coupling losses directly from free space are expected to be very high.

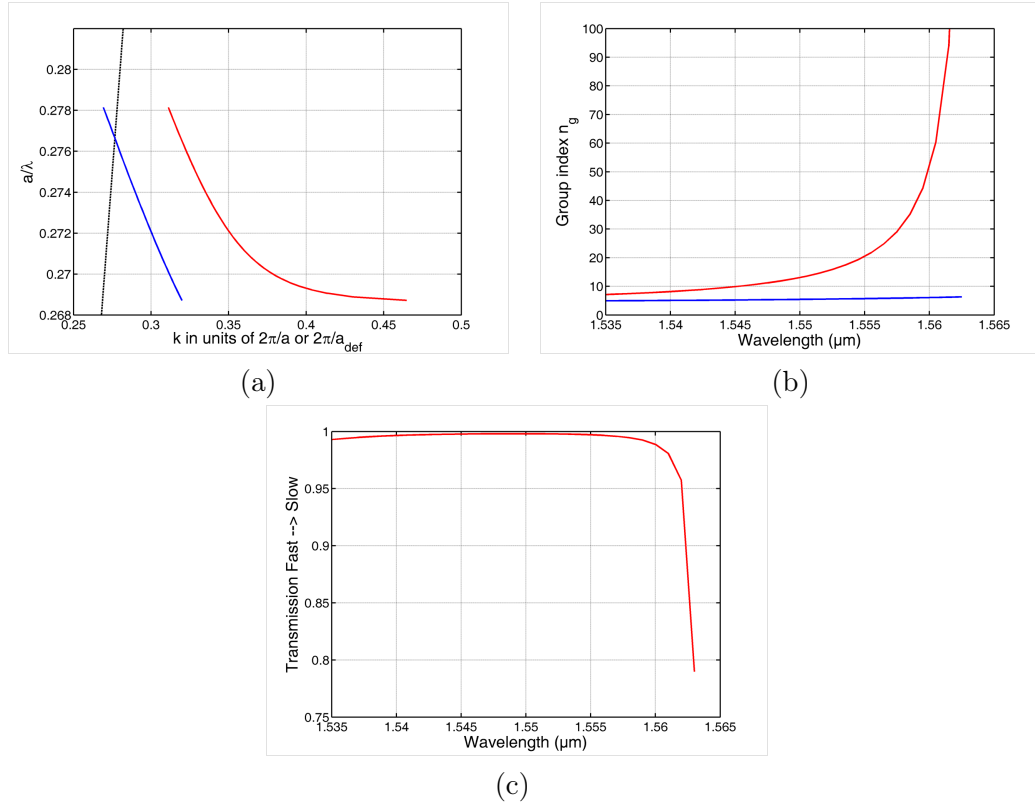


Figure 6.2: (a) Band diagram of the W1 waveguides (In red standard waveguide; in blue waveguide with modified period in the direction of propagation). (b) Group index of light propagating in the waveguide as a function of the wavelength (In red standard waveguide; in blue waveguide with modified period in the direction of propagation) (c) Transmission from the modified to the standard waveguide.

6.1.1 Sample fabrication

The W1 waveguides used in this thesis are similar to the one depicted in figure 6.1. The process described in section 4.1 was used for their fabrication. For these studies, samples with and without quantum wells are considered.

Coupling into the fabricated waveguides requires cleaving the input and output facets with waveguide lengths ranging from 100 μm to 300 μm . Figure 6.3 shows a SEM image of a typical sample fabricated in the clean room facilities of our laboratory.

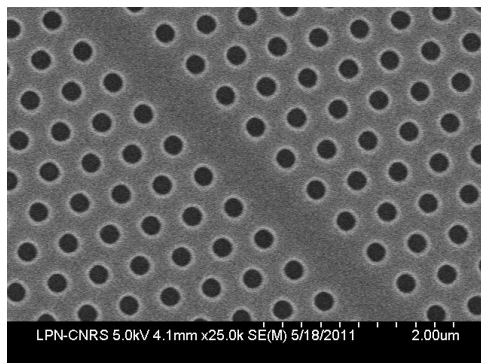


Figure 6.3: SEM image of the W1 waveguide sample (without quantum wells).

To anticipate fabrication imperfections and fluctuations, several waveguides with various parameters are designed on the same sample of the photonic crystal lattice. The length of the *slow-waveguide* is also varied. The different parameters used for the design are summarized in table 6.1.

$r(\text{nm})$	$a(\text{nm})$	$a'(\text{nm})$	L of the slow waveguide(μm)
115	410	430	All fast, 50, 100, 200, 300, 400, All slow
	415	435	
	420	440	
	425	445	
	430	450	
125	410	430	
	415	435	
	420	440	
	425	445	
	430	450	

Table 6.1: Different set of parameters used for the photonic crystal waveguides.

Figure 6.4 is an image of all the waveguides of a unique sample taken by illuminating the sample with a white light and using a CCD camera with a 10X telescope lens. The same set of waveguides is repeated three times. Typically, the waveguides, in the red box in figure 6.4, have the same geometrical parameters a , a' and hole radius r . However the lengths of the slow waveguide, which diffuses less than the fast waveguide and looks grey, are: 0 nm (bottom, the whole waveguide is fast), 50 μm , 100, 200, 300, 400 μm and 2 mm (top). The total length of each waveguide is 2 mm. In order to make the cleavage, 2 sets of square markers are made, separated by 500 μm and 1 mm. These markers can be seen in the top and bottom of the picture in figure 6.4 as white squares.

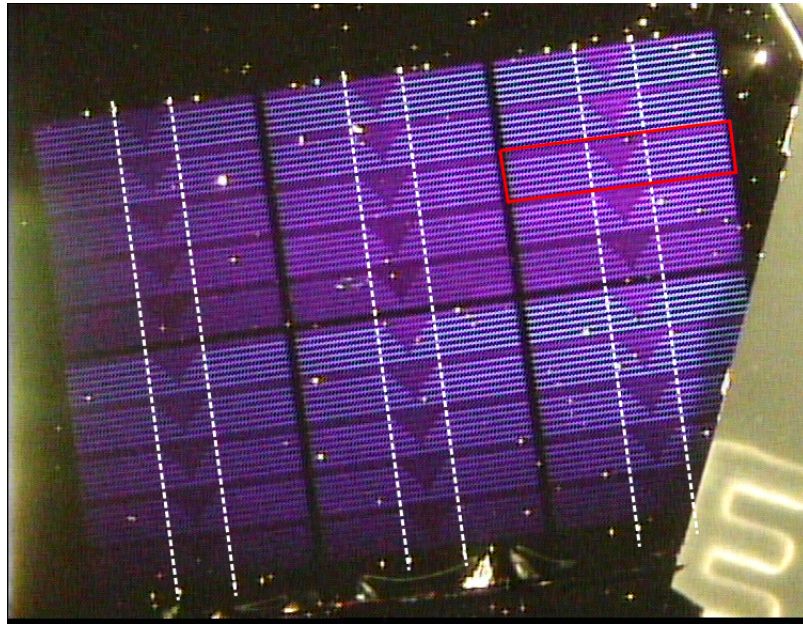


Figure 6.4: Picture of the full sample (without quantum wells) before cleaving. The two dashed white lines are guidance to show the marks where the sample should be cleaved. The red square shows a unit of waveguides with the same lattice parameters and different slow waveguide length.

6.1.2 Cleaving process

In order to couple light into the waveguides, the fabricated samples are cleaved at both ends following preferably the white dashed lines in figure 6.4.

I have to state here that the cleaving process is very delicate due to the fact that our samples are reported on Si which is not the material the best suited for cleavage. On the other hand, the length of the waveguides we wish to obtain, $\sim 500 < \mu\text{m}$, is very short to fully control it.

Figure 6.5 is a picture of a sample after the cleavage. This cleaved sample has a length of $\sim 550\mu\text{m}$, which is close to the targeted length. However, looking at the brightness of the guides, which depends on whether the waveguide is *slow* or *fast*, we can see that: the cleavage is not well centered on the *slow waveguide* and is not perpendicular to the propagation direction of the waveguides.

The fact that cleavage is not symmetric is not of great importance as long as at both ends a part of *fast waveguide* is present, so in the example of figure 6.5 some guides could be used for transmission measurements. When small, the angle between the direction of cleavage and the normal to the propagation direction in the waveguide is not an important issue as it should not affect much the coupling efficiency. It could even be helpful to avoid possible Fabry-Perot interferences coming from Fresnel reflections on the cleaved facets.

The difficulty of the cleaving process is well illustrated in figure 6.6, showing

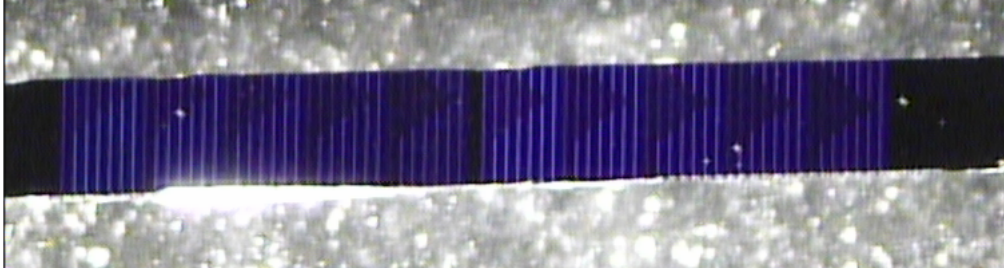


Figure 6.5: Picture of the cleaved sample (without quantum wells).

SEM images of broken end facets caused by the cleavage. These waveguides can not be used.

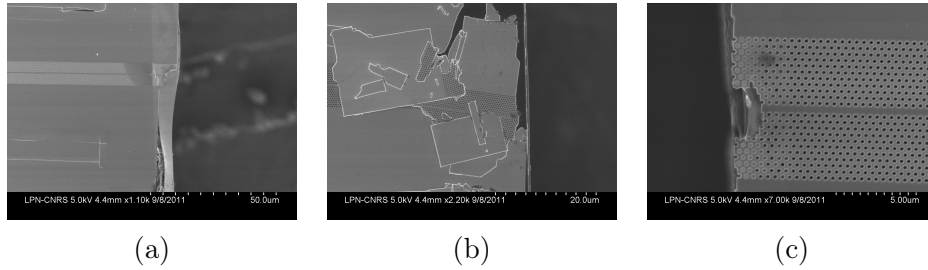


Figure 6.6: SEM images of the cleaved sample (without quantum wells).

In conclusion, we did not succeed to use the butt coupling method directly into a W1 PhC WG. Even though the lateral coupling is a simple method to couple the light into the W1 PhC WG, it has a serious limitation: the cleaving process. Indeed, this process is not reproducible and the minimum length that could be cleaved is around $500 \mu\text{m}$ which could be limiting for a W1 waveguide with QWs, due to the absorption. Finally, because of the low success rate of the cleaving process, the same sample should be repeated several times. An alternative to overcome these difficulties is to use the so-called vertical coupling that has been developed in collaboration with Philippe Lalanne (LCFIO) in the framework of this thesis.

6.2 Vertical coupling

In what follows we will call vertical coupling the coupling perpendicular to the plan of the PhC. The vertical coupling into nanophotonic structures has been widely studied since it allows injecting light into the structure with relatively small technological issues. Vertical grating couplers have already been widely reported since their first theoretical proposition [Tamir 1977] achieving experimental coupling efficiencies of up to 60% [Taillaert 2002, Van Laere 2007]. Another possibility that has been studied in the case of ridge waveguides is the use of metallic gratings [Scheerlinck 2007, Scheerlinck 2008]. Those solutions either imply additional complex technological issues or relatively long access system that are not compatible

with highly nonlinear absorptive PhC. An alternative approach consists in the engineering of the PhC lattice itself at the vicinity of W1. In their article, Tsai et al [Tsai 2011] reported a method allowing direct vertical coupling to a PhC WG. An FDTD analysis was performed to calculate local PhC lattice modifications that could generate a vertical coupler. Theoretical calculations showed an emission angle from the PhC WG restrained to low values ($< 20^\circ$) and a very good coupling efficiency ($\sim 60\%$) from its fundamental mode to a Gaussian beam. However, to our knowledge, no experimental demonstration of such method has been reported. Furthermore the aforementioned study mainly focused on a single frequency at the band edge while this frequency should correspond to extremely high group index values either beyond cut-off or liable to introduce strong disorder-induced losses [Kuramochi 2005].

6.2.1 Theoretical calculations

The vertical coupling method we have adopted is based on the grating approach [Tamir 1977]. By modulating periodically the characteristics of the W1 waveguide lattice in the propagation direction z , light is diffracted out of the waveguide. Symmetrically, by injecting light in the same axis as the diffraction, but in the opposite direction, coupling into the waveguide can be achieved.

The diffraction direction can be deduced using the Bragg *phase-matching* condition in the propagation direction z , between the wavevector β of the guided mode, the wavevector k of the diffracted light and K the wavevector corresponding to the periodicity introduced. However, the Bragg condition does not give an insight on the efficiency of the diffraction.

Analytically, the Bragg condition can be written as:

$$k_z = \beta + pK \quad (6.1)$$

where k_z is the z -component with $|k| = 2\pi/\lambda$, the wavevector of the diffracted light in the air, $\beta = 2\pi n_{W1}/\lambda$, with n_{W1} the effective index of the Bloch mode of the W1 waveguide and $|K| = 2\pi/\Lambda$, is the wavevector associated to the grating having a period Λ . The integer p is the diffraction order.

To obtain vertical coupling one needs to have $k_z = 0$. According to equation (6.1), we obtain the following condition:

$$n_{w1} + p \frac{\lambda}{\Lambda} = 0. \quad (6.2)$$

In our particular case, this condition can be fulfilled at a particular wavelength λ by optimizing the periodicity Λ of the grating. We assume that the W1 waveguide is perturbed by an added periodic modulation. This perturbation acts as a grating coupler with a leakage perpendicular to the propagation direction provided that the phase-matching condition (6.2) is valid provided that one neglects the effective-index change induced by the weak modulation [Tamir 1977]

The coupler has been designed for coupling or decoupling light perpendicularly to the waveguide at a group index of 20 ($\lambda = 1538$ nm). We have first calculated the effective index $n_{W1} = 2.32$ of the Bloch mode of the W1 waveguide (sketched in figure 6.7.a) for this specific wavelength. For $p = 1, 2 \dots$ we find $\Lambda = 0.68 \mu\text{m}$ ($\sim 1.6a$) and $\Lambda = 1.35 \mu\text{m}$ ($\sim 3.2a$). The perturbed waveguide (see figure 6.7.b) is no longer periodic (or the period is very long) because Λ and a are not commensurate in general. Although the perturbed waveguide of figure 6.7.b is likely decoupling light normally, we have deliberately chosen to opt for a full-periodic coupler design by changing the PhC period along the propagation direction in order to render Λ and the new period a' commensurate. In comparison to the case $p = 1$, the $p = 2$ case is more favorable since a periodicity of $\sim 3.2a$ requires only a very slight increase of the longitudinal period, which becomes $a' = \Lambda/3 = a + 30$ nm. The resulting perturbed coupler with a periodicity of $3a'$ is shown in figure 6.7.c. Finally, to ease the fabrication process, we have decided to avoid etching the central part of the waveguide and to use a heterostructure coupler, in which solely the two inner rows of holes are modified. To keep the average effective index almost constant in order to satisfy the phase matching condition of equation (6.2) we decided to increase the radius of some holes and to decrease that of others. The radius increment is denoted by Δr . Figure 6.7.d shows the resulting heterostructure. Finally, by using a Bloch mode solver able to analyze leaky Bloch modes of photonic crystal waveguides operating above the light [Lalanne 2002], we have optimized the parameter Δr to guaranty an efficient decoupling at normal incidence.

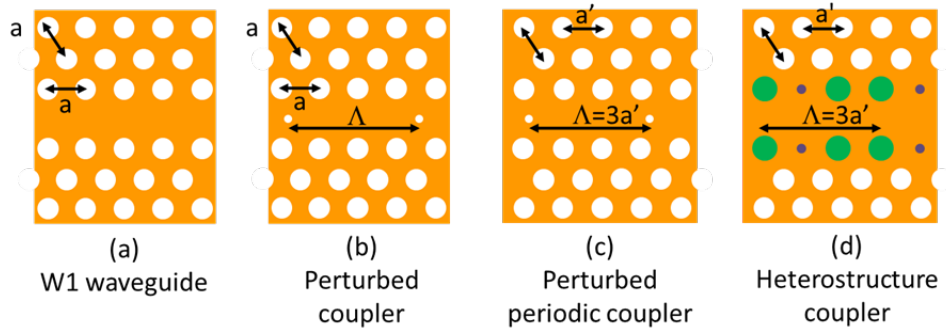


Figure 6.7: Description of the steps of the design conception of the vertical coupler.

Resuming, the vertical coupler is achieved by modifying the period a of the triangular lattice of the PhC and the radius r of the holes. The period in the z -direction of the triangular lattice is changed to a' and the periodic modification of the holes radius allow us to have a grating period (Λ) which can be a multiple the triangular lattice: $\Lambda = ma'$ where m is an integer. We can then rewrite equation (6.2) in terms of these parameters:

$$n_{w1} + p \frac{\lambda}{ma'} = 0 \quad (6.3)$$

where a' is the modified period and m is the factor by which we multiply the original period of the triangular lattice.

Figure 6.8 presents the adopted solution. The period is $\Lambda = 3a'$ and the diffraction is at second order ($p = 2$). In the coupler region the period (a') in direction of the propagation of light is increased and the radius of the holes in the holes line adjacent to the guiding region are modified: every three holes the radius of one is reduced by Δr and the other two are increased by the same amount (Δr).

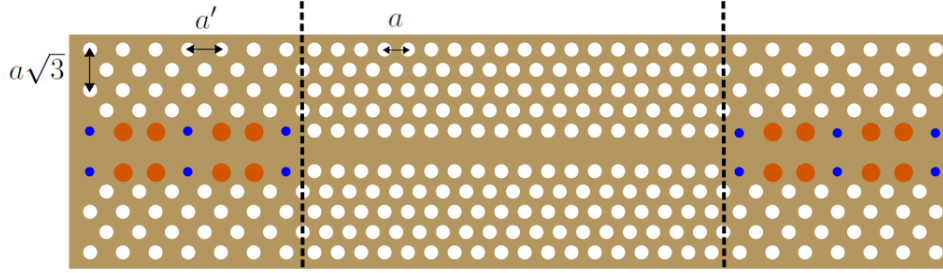


Figure 6.8: Sketch of sample with vertical couplers at the two extremities.

Once the parameters of the coupler are defined, we make exact numerical computations (numerical simulations were performed at Institut d'Optique Graduate School by Philippe Lalanne) in order to study its characteristics. The method used hereafter has been described in a previous work [Lecamp 2007] for the general case of light propagation and light emission in three-dimensional (3D) periodic waveguides and in stacks of them. In brief, the Bloch-mode method operates in the frequency domains and relies on an analytical integration of Maxwell's equations along the longitudinal direction and on a supercell approach in the two others. Perfectly-Matched-Layers implemented as nonlinear coordinate transforms [Hugonin 2005] are used in the transverse x - and y -directions to carefully handle out-of-plane far-field radiations in the air clad. The numerical sampling in the transverse direction is performed in the Fourier space using truncated Fourier series. The approach directly relies on methods developed in the 90's for grating analysis [Moharam 1995, Li 1997]. The numerical results are obtained for truncation ranks, $m_x = 25$ and $m_y = 14$. This implies that a total number of $N_s = (2m_x + 1) \times (2m_y + 1) = 1479$ Fourier coefficients are retained in the calculation. Indeed, the accuracy of the computational results increases as N_s increases, but calculations performed for larger N_s have revealed that the truncation error has no influence on the discussion and on the conclusion. The reflection, the transmission and the diffraction, referred as the out-of-plan losses, are calculated along with the diffraction angle. These parameters are defined in figure 6.9.

Figure 6.10 presents the transmission (a), the out of plane losses (b), the reflexion (c) and the diffraction angle θ (d) for a triangular lattice photonic crystal period $a = 420$ nm, holes radius $r = 125$ nm and $n = 3.31$. In the coupler, the period is $a' = 450$ nm, $\Delta r = 35$ nm and the number of periods Λ is 15 decided as a compromise between the coupling efficiency and the short length of the coupler.

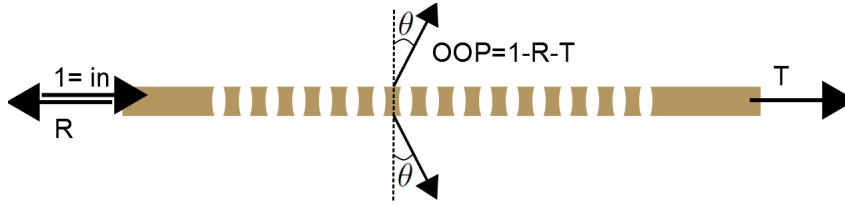


Figure 6.9: Unidimensional sketch of the vertical coupler with the definitions of the parameters: R (reflection), T (transmission), OOP (out of plane), θ (angle of out of plane with respect to the vertical).

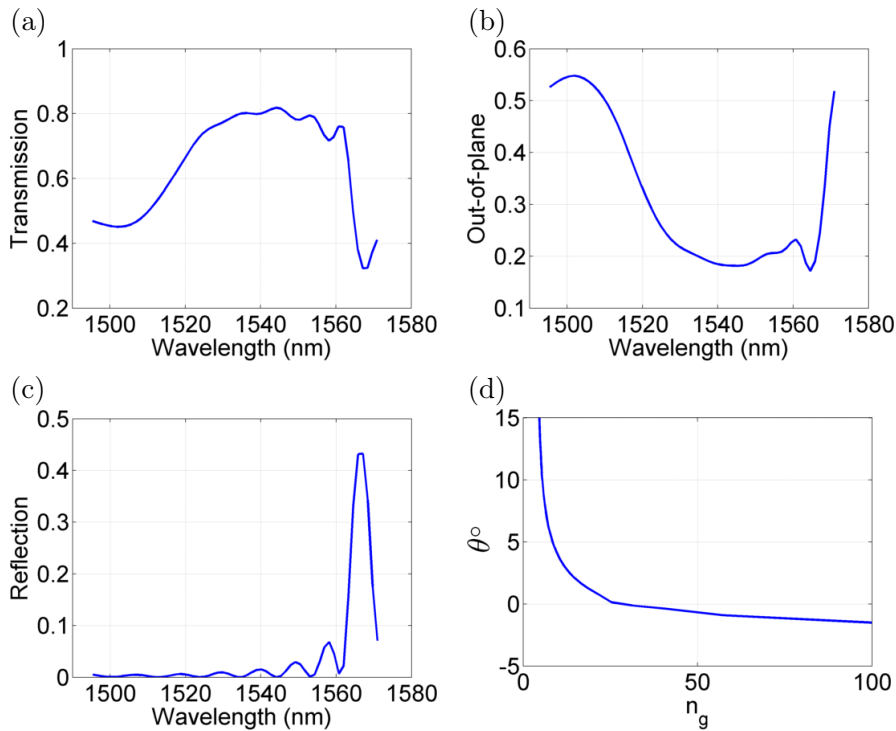


Figure 6.10: Characteristics of the coupler for a waveguide with: $a = 420$ nm, $r = 125$ nm and $n = 3.31$, and a coupler with: $a' = 450$ nm, $\Delta r = 35$ nm and 15 periods (Λ). (a) Transmission, (b) Out of plane and (c) reflexion as a function of the wavelength and (d) θ as a function of the group index of the waveguide. Numerical simulations were performed at *Institut d'Optique* by Philippe Lalanne.

The transmission losses, presented in figure 6.10.a, shows two minima one at $\lambda \simeq 1505$ nm, at the fast regime ($n_g \sim 5$) and the other at $\lambda \simeq 1568$ nm corresponding to $n_g = 40$. We can see in figure 6.10.b that the diffraction efficiency (*OOP*) ranges between 10 and 55 % depending on the wavelength, it presents maxima at the wavelengths where the transmission is minimum. Figure 6.10.d shows that we have a broadband extraction within a diffraction angle smaller than 5° from a group index of 10 to more than 100. However, looking at figure 6.10.c we can notice

that the coupler also introduces an important reflection, presenting a maximum at $\lambda \simeq 1567$ nm which coincides with the *OOP* maximum at the slow light regime. On one hand, this generates difficulties to do a one way transmission measurements: coupling into the waveguide, propagating along the waveguide, and extracting light from the waveguide. On the other hand, the reflections allow to measure the group index of the waveguide since the couplers act as mirrors and the system constituted by the two couplers and the waveguide (see figure 6.8) behaves like a Fabry-Perot resonator.

We will now analyze the modification of the different parameters due to this Fabry-Perot effect and show the way the group index can thus be extracted. A basic sketch of a Fabry-Perot interferometer is shown in figure 6.11, where E_i is incoming signal, t_1 and r_1 are the transmission and reflection of the first mirror and t_2 and r_2 those of the second mirror of the Fabry-Perot. The transmitted intensity is then given by:

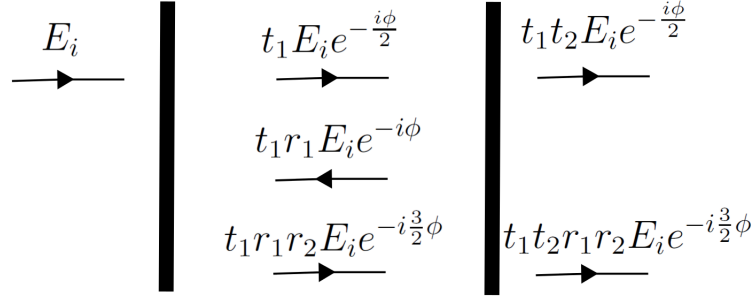


Figure 6.11: Fabry-Perot model

$$I_t = \frac{I_i}{1 + \frac{4}{\gamma^2} \sin^2\left(\frac{\phi}{2}\right)} \quad (6.4)$$

where we have assumed that $r_1 = r_2 \equiv r$, $t_1 = t_2 \equiv t$ and have defined $t^2 = T$ and $r^2 = R = 1 - T$. The phase ϕ is associated to the propagation round-trip in the resonator and is defined as $\phi = 2\pi n/L$ where n is the resonator index of refraction and L the cavity length. γ is defined as $\gamma \equiv (1 - R)/\sqrt{R}$. Figure 6.12 is a Fabry-Perot equivalent sketch of the waveguide with the in-coupler and the out-coupler playing the role of the Fabry-Perot mirrors. One has to replace the transmission coefficient of the mirrors in figure 6.11 by the coefficient o representing the out-of-plan amplitude diffraction of the couplers. The transmitted intensity is then given by:

$$I_t = \frac{I_i O^2}{(1 - R)^2 + 4R \sin^2\left(\frac{\phi}{2}\right)} \quad (6.5)$$

where $O = o^2$.

According to expression (6.5), Fabry-Perot peaks are expected when tuning the wavelength. These peaks have been shown to be helpful when one wants to deter-

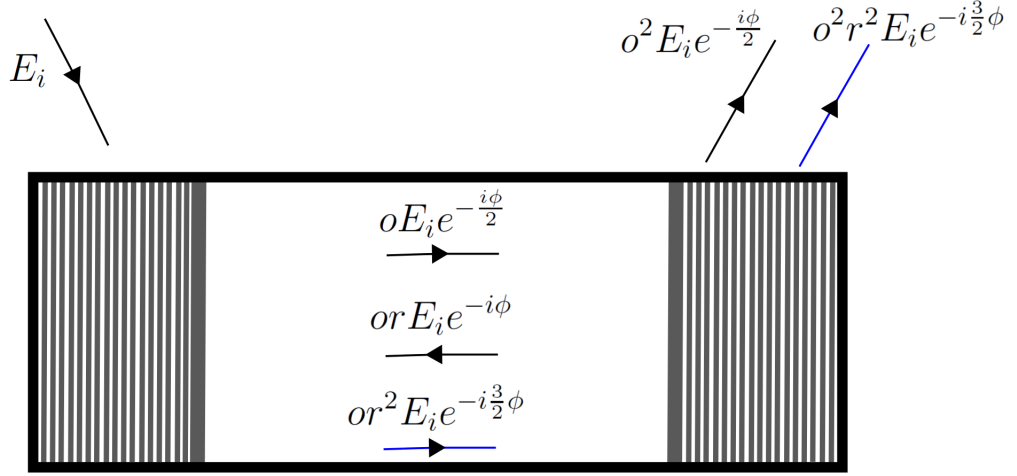


Figure 6.12: Sketch of a Fabry-Perot interferometer with vertical coupling

mine the group index of the waveguide. Measuring the free spectral range between peaks we determine the group index as we will show next.

Calculation of the group index from the free spectral range The expression of the phase of a wave after the propagation through a length L with an effective index n_{eff} is

$$\phi(\omega) = n_{\text{eff}}(\omega) \frac{\omega}{c} L$$

We can then write the phase difference between two consecutive maxima

$$n_{\text{eff}}(\omega') \frac{\omega'}{c} L - n_{\text{eff}}(\omega) \frac{\omega}{c} L + \phi_m(\omega') - \phi_m(\omega) = \pi$$

Setting $\omega' = \omega + \Delta\omega$ and $n'_{\text{eff}} = n_{\text{eff}} + \Delta n_{\text{eff}}$ where $n_{\text{eff}} = n_{\text{eff}}(\omega)$ and $n'_{\text{eff}} = n_{\text{eff}}(\omega')$, we can rewrite the previous equation as:

$$n_{\text{eff}} \frac{\omega}{c} L + (n_{\text{eff}} + \Delta n_{\text{eff}}) \frac{\Delta\omega}{c} L - n_{\text{eff}} \frac{\omega}{c} L + \Delta\phi_m = \pi$$

Throwing away the second order term we can rewrite then:

$$\frac{\Delta\omega}{c} L (n_{\text{eff}} + \omega \frac{\Delta n_{\text{eff}}}{\Delta\omega}) + \Delta\phi_m = \pi$$

The group index, $n_g = n_{\text{eff}} + \omega \frac{\Delta n_{\text{eff}}}{\Delta\omega}$, is written as:

$$n_g = \frac{c}{L\Delta\omega} (\pi - \Delta\phi_m) \quad (6.6)$$

We can finally rewrite the expression as a function of the wavelength,

$$n_g = \frac{\lambda^2}{2\pi L \Delta\lambda} (\pi - \Delta\phi_m), \quad (6.7)$$

where $\Delta\phi_m$ can be neglected as shown in [Mazoyer 2011a] from 3D numerical computations.

Expression (6.7) has shown to be very practical to determine the group index experimentally. Indeed from the transmission spectrum, one only has to determine the free spectral ranges $\Delta\lambda$ between two successive Fabry-Perot peaks and their wavelengths to calculate the group index. We will implement this approach at the end of this chapter.

6.2.2 Experimental validation of the coupler and measurement of the group index

The purpose of this section is to present one implementation of the proposed vertical couplers, as well as its characterization. Its functioning is tested here on conventional passive W1 photonic crystal waveguides (W1 PhC WGs) with an injecting and an extracting coupler. Next chapter is devoted to an analogue structure containing active (absorptive) media.

6.2.2.1 Sample design

The photonic crystals (PhCs) are $10 \mu\text{m} \times 500 \mu\text{m}$ air hole triangular lattice InP suspended membranes. The waveguide is placed at the center of the PhC small side, as shown by the scanning electron microscope (SEM) image in figure 6.13. The W1 waveguide is generated by missing a row of holes (in the long axis) during the fabrication. Two couplers are also introduced in this line defect setting the propagating length L_p .

The sample was fabricated following the same process described for the cavities in section 4.1. The only difference is that here the PhC layer is constituted of a membrane of indium phosphate (InP) with a thickness $e = 265 \text{ nm}$. This gives a refractive index of 3.16 instead of 3.31 for the samples containing the active media.

Different PhC WGs were fabricated changing the parameters of triangular lattice, those of the coupler and the propagating distance. The radius remains constant at $r = 115 \text{ nm}$, the periods of the triangular lattice are $a = 420, 430, 440 \text{ nm}$, the periods of the coupler in the propagation direction are such that $a' - a = 30, 40 \text{ nm}$ and the propagating lengths are $L_p = 100$ and $200 \mu\text{m}$. This set of parameters is showed in table 6.2.

6.2.2.2 Experimental set-up and sample description

Figure 6.14 shows the experimental set-up. A fibered continuous-wave (cw) laser emitting up to 15 mW and tunable from 1490 nm to 1650 nm is used (*Tunics*). The light is sent to free space using an achromatic reflective collimator (ARC), this is of

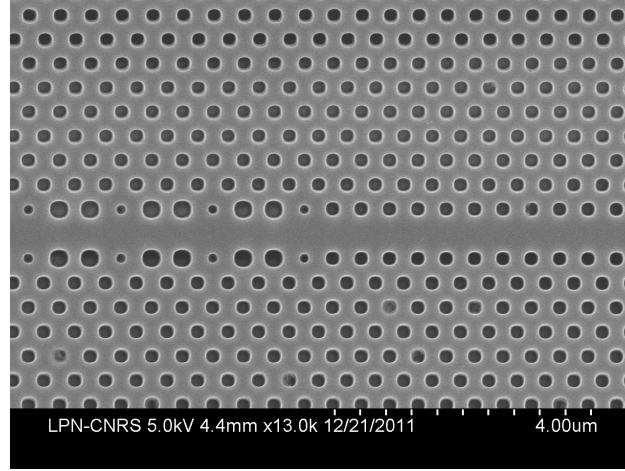


Figure 6.13: SEM (scanning electron microscope) image of the transition between W1 waveguide (triangular lattice with period $a=440$ nm, holes radius $r=115$ nm) and the coupler (modified period $a'=470$ nm, radius increment/reduction $\Delta r=35$ nm).

$r(\text{nm})$	$a(\text{nm})$	$a'(\text{nm})$	$\Delta r(\text{nm})$	$L_p(\mu\text{m})$
115	430	460	35	100 and 200
		470		
	440	470		
		480		
	450	480		
		490		

Table 6.2: Different parameters used for the W1 photonic crystal waveguides with injecting/extracting coupler.

particular importance since a wide spectral sweep is performed. A polarizing beam splitter and a half-wave plate (HWP) are used to guarantee a linear polarization in the direction x . The use of a 50/50 beam splitter allows to send the signal to the sample -through a 10X microscope objective (0.25 NA)- and to recover it through the same objective. The signal is injected into the sample by one coupler and coupled out by the other, after a propagation through the waveguide of $L_p = 100$ or $200 \mu\text{m}$ depending on the given PhC WG. Finally, a second beam splitter (99% of transmission) sends a small part of the signal to a high sensitivity InGaAs camera and the most part of the signal is coupled into an optical fiber using a second collimator identical to the implemented at the input of the set-up. The signal is then sent to a fast avalanche photo-diode (APD).

Figure 6.15 shows an image of the sample taken with the infrared camera presenting three W1 waveguides with the coupling achieved in the central one. The brightest spot (on the left) is due to the reflexion of the injection signal which is not coupled into the waveguide; the small and elongated spot corresponds to the light

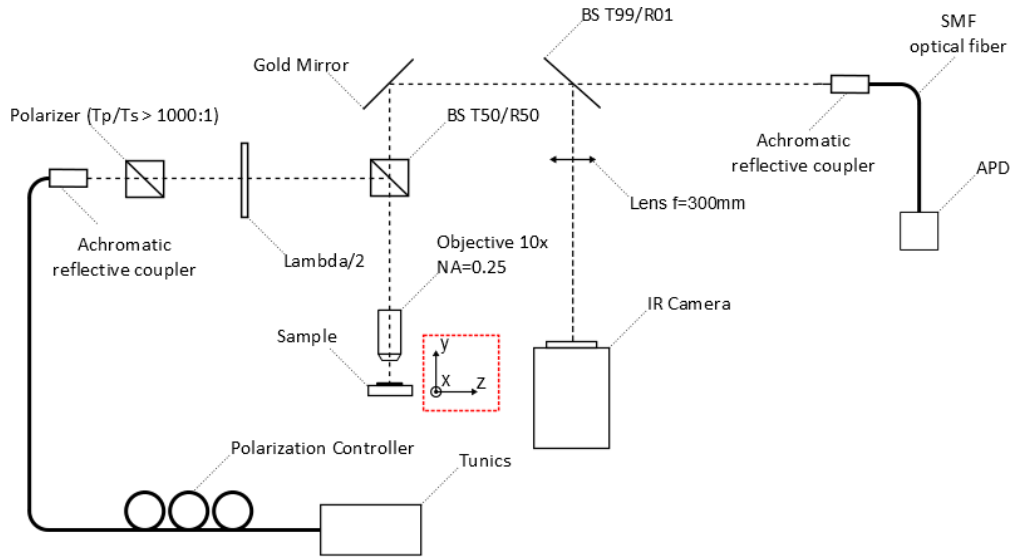


Figure 6.14: Experimental set-up used to characterize the W1 photonic crystal couplers.

scattered at the output coupler after passing through the $200 \mu\text{m}$ long W1 PhC WG.

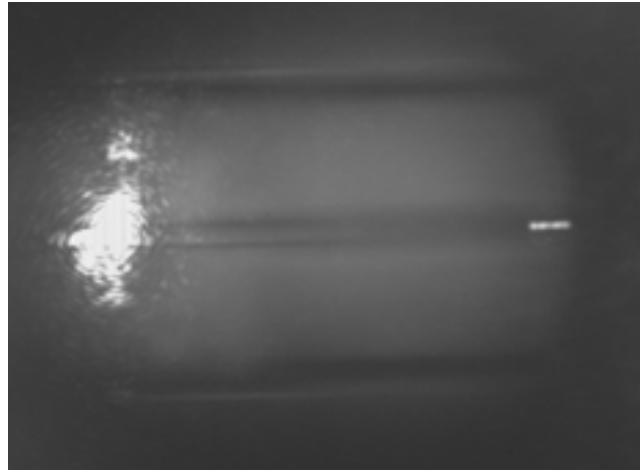


Figure 6.15: InGaAs infrared camera snap shot of the reflected and transmitted signal over the sample, light is injected from the left, propagates in the waveguide and then is outcoupled on the right side.

Looking at the image in figure 6.15 it becomes clear that a spatial filter is needed to isolate the transmitted signal from the reflection, this can be performed in two alternative ways. The simplest one, if only intensity is needed, is to digitally integrate the pixel intensity in a selected region of the image, this is done using a *LabView* program. The *LabView* program controls the tunable laser source -drive

the wavelength scan- and allows to select two areas of integration in order to measure the reflected and transmitted signal for a given waveguide.

The other option in order to measure the transmitted signal is to use a confocal spatial filtering system. This system is implemented in this particular case using the SMF optical fiber as *pinhole* (spatial filtering device) and light is focalized in it using the ARC. This particular system offers one advantage. It is possible to replace the detector by a laser and to do an inverse coupling; this procedure guarantees that the selected area is the most adequate one. Also, this approach enables, by the use of a fast avalanche photo diode, the possibility of making temporal measurements.

First experimental measurements are performed for a W1 PhC WG with a triangular lattice period $a = 440$ nm and a hole radius $r = 115$ nm. Figure 6.16 shows the calculated evolution of the group index in such a waveguide as a function of wavelength.

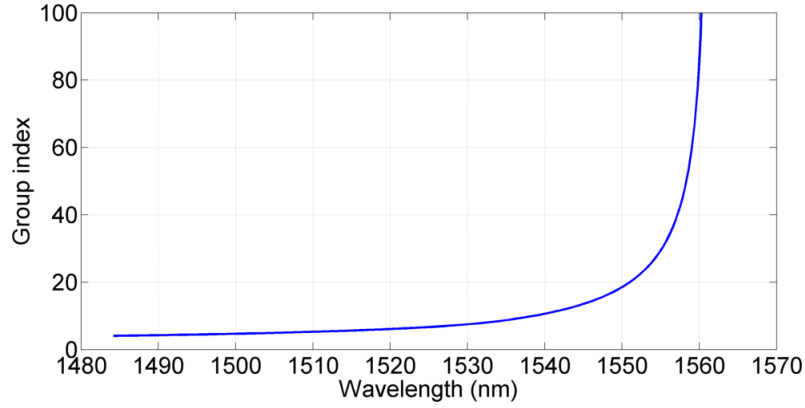


Figure 6.16: Group index as a function of the wavelength for a W1 PhC WG with: triangular lattice period $a = 440$ nm, hole radius $r = 115$ nm, membrane thickness $e = 265$ nm and $n = 3.16$. The 3D numerical simulations were performed at *Institut d'Optique* by Philippe Lalanne with a Fourier modal method [Lalanne 2002].

The couplers used had a modified period $a' = 470$ nm, an increment/reduction of the hole radius $\Delta r = 35$ nm and a length of 15 periods (Λ) giving approximately $20 \mu\text{m}$ length of the the coupler area. The numerical calculations for such a coupler are presented in figure 6.17. Figure 6.17.a shows the transmission (T) spectrum, figure 6.17.b the reflexion (R) spectrum and figure 6.17.c the out of plane coupling (OOP) spectrum. We can see that for low wavelengths -corresponding to $n_g \sim 5$ - the OOP is not negligible ($\sim 50\%$), nevertheless the losses (transmission) are also important. Closer to the band-gap, at $\lambda \sim 1535$ -corresponding to $n_g \sim 10$ the transmission is reduced having then an increase of the reflection and OOP .

6.2.2.3 Experimental results

The propagation length (distance between couplers) L_p of the waveguide was $200 \mu\text{m}$. The laser source wavelength is tuned from 1490 nm to 1550 nm mea-

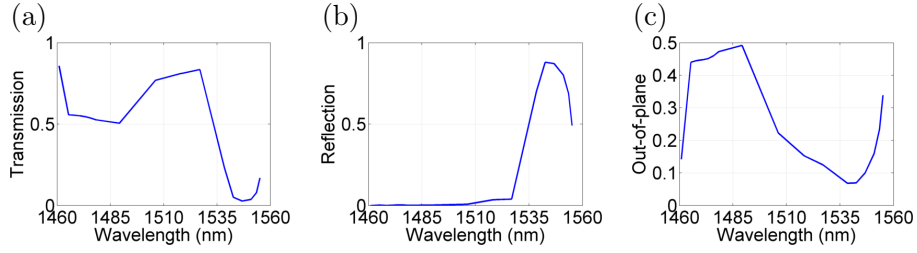


Figure 6.17: Characteristics of the coupler for a waveguide with: triangular lattice period $a = 440$ nm, hole radius $r = 115$ nm, membrane thickness $e = 265$ nm and $n = 3.16$, and a coupler with: $a' = 470$ nm, $\Delta r = 35$ nm and 15 periods (Λ). (a) Modal transmission T , (b) modal reflexion R and (c) Out of plane loss $(1 - R - T)$ as a function of the wavelength. Numerical simulations were performed at *Institut d'Optique Graduate School* by Philippe Lalanne with a 3D Bloch-mode modal method using Fourier expansions and perfectly-matched layers [Lecamp 2007].

asuring the transmitted signal by spatially filtering in the camera. Figure 6.18 shows in blue the obtained spectrum and in green a theoretically obtained spectrum.

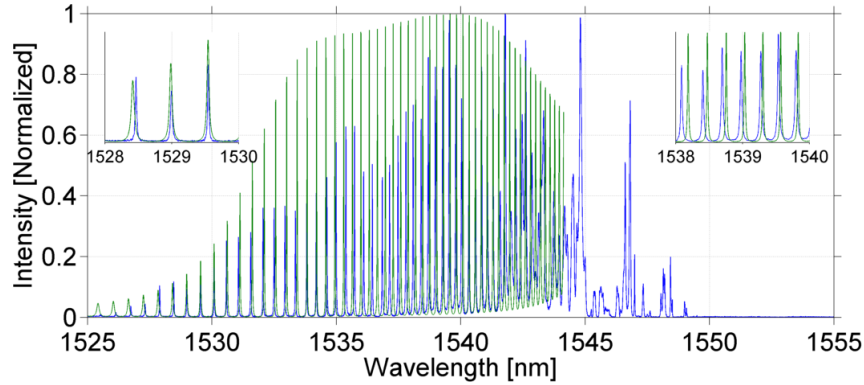


Figure 6.18: Transmission spectrum for a waveguide with a propagation length $L_p = 200 \mu\text{m}$, $a = 440$ nm triangular lattice period, $r = 115$ nm hole radius and $a' = 470$ nm period of the coupler in the direction of propagation. Blue, experimental; Green, theoretical.

The spectrum presents Fabry-Perot resonances, as expected from the high reflection predicted by the simulations shown in figure 6.17. The high wavelength limit in this transmission spectrum is set by the waveguide cut-off. The large group indices enhance the consequences of the fabrication imperfections generating strong losses and a chaotic behavior [Mazoyer 2011b]. The low wavelength limit is due to the high losses of the whole system given by couplers transmission, as shown in figure 6.17.a.

To compare the theoretical predictions with the experimental results we introduce the values for the reflexion (R), the transmission (T) and the out of plane coupling (OOP) represented in figure 6.17 in the expression (6.5). This is repre-

sented by the green line in figure 6.18. The theoretical curve (green line) was shifted in order to set the $n_g = 10$ for the wavelength $\lambda = 1527$ nm in order to compensate for the uncertainties and lack of knowledge of exact values for the membrane thickness and refractive index. Also, the normalized intensity is corrected so that both intensities have the same value at the peak at 1531 nm. Considering these uncertainties, the agreement between theory and experience is good. It must be said that for the calculations there are not any free parameter with the only exception, the already mentioned slight shift of the wavelength.

Exploiting the Fabry-Perot resonances we retrieve the group index evolution of the waveguide mode as a function of the wavelength through the measurement of the free spectral range (FSR) of the transmitted signal using the relation (6.6). Figure 6.19 shows the inferred experimental group indices (circles in blue ●) and the green line corresponds to the same numerical calculations presented in figure 6.16.

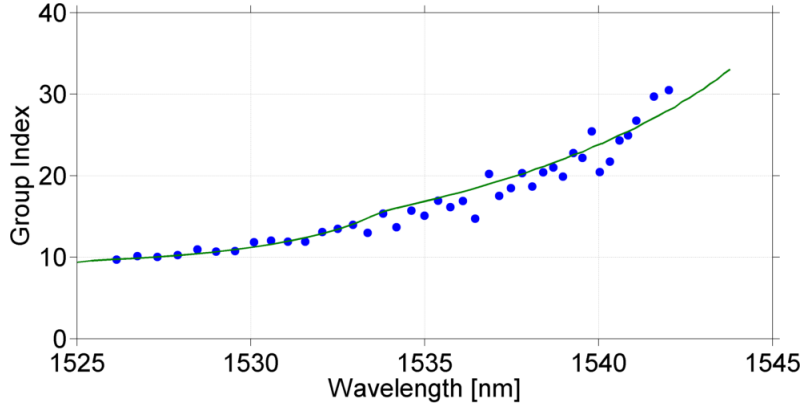


Figure 6.19: Group index as a function of the wavelength for a waveguide with a propagation length $L_p = 200 \mu\text{m}$, $a = 440$ nm triangular lattice period, $r = 115$ nm hole radius and $a' = 470$ nm period of the coupler in the direction of propagation. ●: obtained from experimental spectra; green line: theoretical data.

The transmission spectra are performed for all the W1 PhC WGs presented in table 6.2. Figure 6.20 shows the spectra obtained for samples with $a' = a + 30$ nm and $L_p = 200 \mu\text{m}$.

As previously described, using the experimental transmission spectra the group index can be deduced from the free spectral range. Figure 6.21 shows the group indices for all the waveguides with $a' = a + 30$ nm. It is noteworthy that the measured group indices for every set of parameters is equivalent regardless of the length, confirming the reproducibility of the fabrication. Also, group indices go from values around 10 to values around 100. The measurement of the smaller values of n_g is limited by the small reflexion of the coupler inducing a poor contrast for the Fabry-Perot fringes. On the other hand, at high group index values, the limitation is given by the fact that when group indices are large the imperfections on the fabrication make the transmission low and chaotic [Mazoyer 2011b].

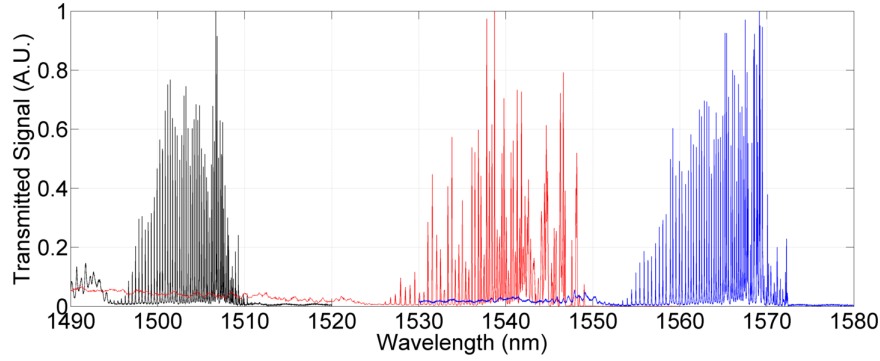


Figure 6.20: Transmission spectra for different waveguides of $L_p = 200 \mu\text{m}$ propagation length and period of the coupler in the direction of propagation of $a' = a + 30 \text{ nm}$, a hole radius $r = 115 \text{ nm}$ and a hole radius increment/reduction in the coupler $\Delta r = 35 \text{ nm}$. Black $a = 430 \text{ nm}$, red $a = 440 \text{ nm}$, blue $a = 450 \text{ nm}$.

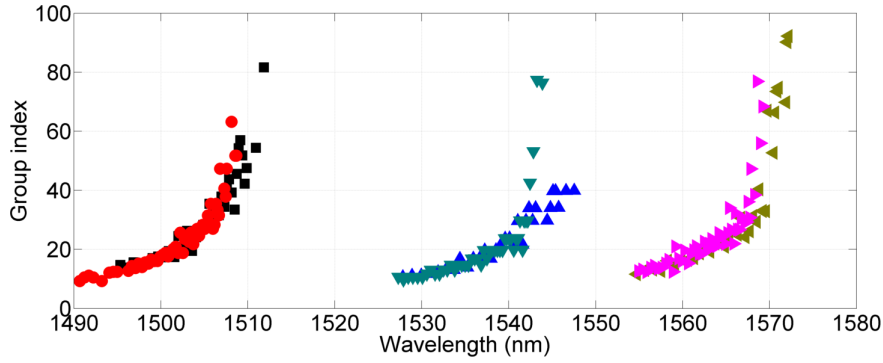


Figure 6.21: Group index for different waveguides in function of the wavelength. \blacksquare $a = 430 \text{ nm}$, $L = 100 \mu\text{m}$, \bullet $a = 430 \text{ nm}$, $L = 200 \mu\text{m}$, \blacktriangle $a = 440 \text{ nm}$, $L = 100 \mu\text{m}$, \blacktriangledown $a = 440 \text{ nm}$, $L = 200 \mu\text{m}$, \blacktriangleleft $a = 450 \text{ nm}$, $L = 100 \mu\text{m}$, \blacktriangleright $a = 450 \text{ nm}$, $L_p = 200 \mu\text{m}$. $a' = a + 30 \text{ nm}$ and $r = 115 \text{ nm}$ in all cases.

Next, we study the samples where the period of the coupler in the propagation direction is such that $a' = a + 40 \text{ nm}$ and the propagation length (distance between couplers) $L_p = 200 \mu\text{m}$. Transmission spectra for the three waveguides ($a = 430 \text{ nm}$, $a = 440 \text{ nm}$, $a = 450 \text{ nm}$) are presented in figure 6.22.

The cut-off wavelengths are approximately 1508, 1542 and 1569 nm for the triangular lattice periods $a=430$, 440 and 450 nm, respectively. As expected, these cut-offs wavelengths are similar to the cut-offs wavelengths of W1 PhC WGs with the same waveguide lattice parameters (a and r) and $a' = a + 30 \text{ nm}$. This is, cut-off wavelength depends on waveguide lattice parameters and not on the coupler parameters. However, the contrast of the Fabry-Perot resonances is much smaller making the determination of the free spectral range imprecise and thus group index determination impossible.

As a partial conclusion, we have showed that using the designed vertical coupler

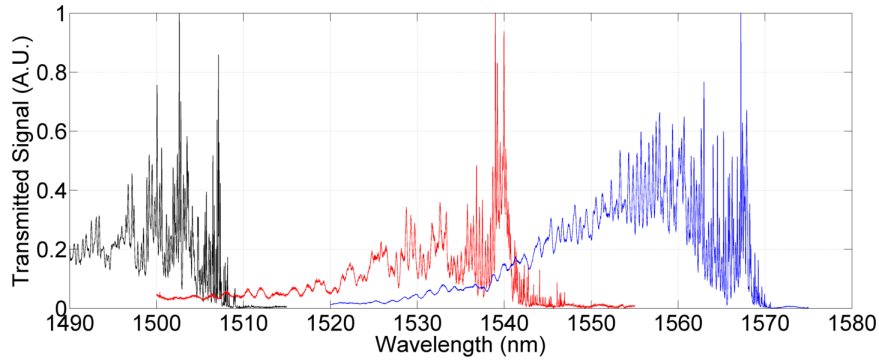


Figure 6.22: Transmission spectra for different waveguides of $L_p = 200 \mu\text{m}$ propagation length and period of the coupler in the direction of propagation of $a' = a + 40 \text{ nm}$, a hole radius $r = 115 \text{ nm}$ and a hole radius increment/reduction in the coupler $\Delta r = 35 \text{ nm}$. Black $a = 430 \text{ nm}$, red $a = 440 \text{ nm}$, blue $a = 450 \text{ nm}$.

we succeeded to inject and extract light into a W1 PhC WG. The coupler design should be improved in order to diminish its reflectivity. Nevertheless, we have shown that it is possible to take benefit from this drawback to measure the W1 group index evolution. Using the Fabry-Perot FSR, group indices going from ~ 10 to ~ 100 were measured. However, the small reflectivity for $n_g < 10$ prevents from measuring n_g in the whole wavelength range. In the following we implement an additional engineering to fill this gap.

Indeed, it has been showed by S. Mazoyer in his PhD. thesis [Mazoyer 2011a] that the introduction of one hole in the row of missing holes produces broadband, strong reflection. In figure 6.23 we show the design done to exploit this specificity. The full structure is identical as before, the only difference is that two additional holes are introduced, one at the input of the W1 the other at the output. The hole radius is the same that those at the lattice surrounding the W1.

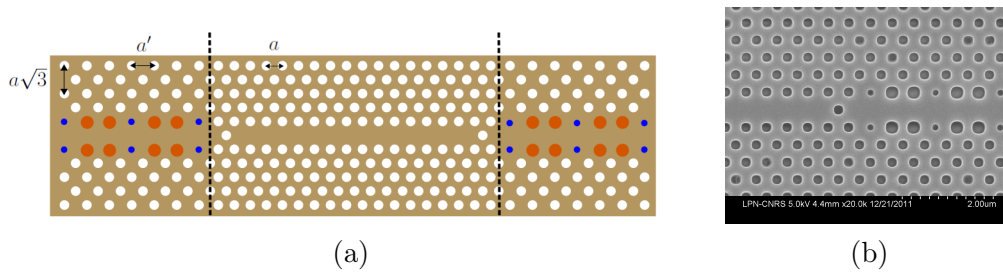


Figure 6.23: (a) Sketch of sample with the vertical coupler and the *reflecting holes*. (b) SEM image of the transition between the coupler (on the right) and W1 waveguide (on the left) with the *reflecting hole* with a triangular lattice period $a = 440 \text{ nm}$, a hole radius $r = 115 \text{ nm}$, a coupler period in the direction of propagation $a' = 470 \text{ nm}$ and a radius increment/reduction $\Delta r = 35 \text{ nm}$.

In figure 6.24 the spectrum obtained at the output of the regular W1 (without

additional holes) is presented in red -it is the same as in figure 6.20 (red)-. The black line shows the spectrum obtained for a sample of same parameters where the two *reflecting holes* are introduced. They allow to obtain contrasted Fabry-Perot fringes over the 1490 nm-1525 nm range. A spectral region complementary to the one obtained without holes.

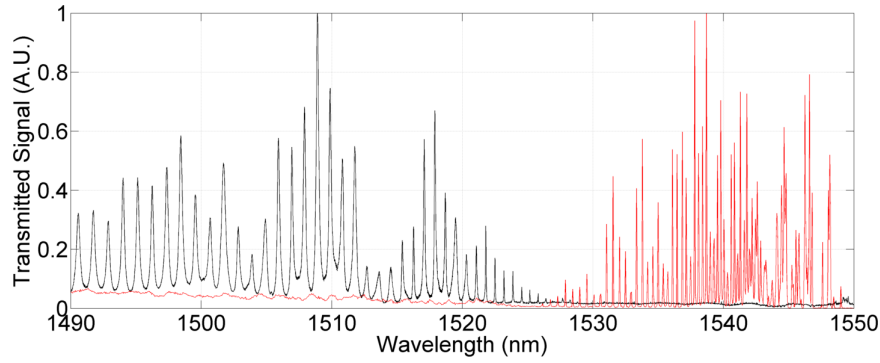


Figure 6.24: Transmission spectra for waveguides of $L_p = 200 \mu\text{m}$ length, $a = 440 \text{ nm}$ period, $r = 125 \text{ nm}$ radius and $a' - a = 30 \text{ nm}$ difference between the period of the coupler in the direction of propagation a' and waveguide period a with (black) and without (red) reflecting holes.

We use again the Fabry-Perot resonances FSR to retrieve the group index via relation (6.6). The group indices corresponding to the spectra shown in figure 6.24 are presented in figure 6.25 with the same color code, red for the regular sample and black for the one with additional holes. It can be seen that both curves are connected. Together they allow to cover the spectral range going from 1490 nm to 1543 nm in which the group index varies from $n_g = 5$ to $n_g = 78$.

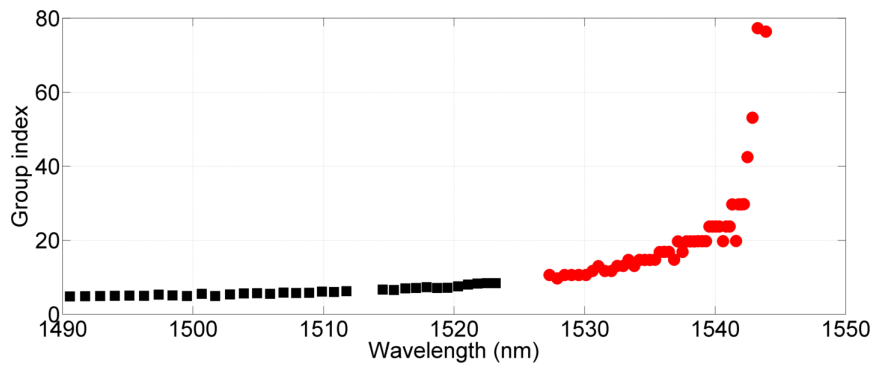


Figure 6.25: Group index for waveguides of $L_p = 200 \mu\text{m}$ length, $a = 440 \text{ nm}$ triangular lattice period, $r = 115 \text{ nm}$ hole radius, $a' = 470 \text{ nm}$ period of the coupler in the direction of propagation and an increment/reduction of the hole radius $\Delta r = 35 \text{ nm}$ with (■) and without (●) reflecting holes.

6.3 Conclusion

Coupling light into a short W1 PhC WG is not a simple task. We first tried the simplest possible method: butt coupling from free space. The cleavage of such a short waveguide with the additional difficulty of the Si substrate was very problematic. We then explore an alternative approach using a periodical perturbation before the waveguide to achieve a short vertical coupler. We fabricated and tested such approach both to couple light into a short W1 PhC WG and to decouple it. Thanks to its angular acceptance the coupler works for a quite wide wavelength range. Its efficiency is not high but largely enough for the envisaged nonlinear experiments.

The main drawback of the present design is the reflectivity of the coupler that induces Fabry-Perot effects. We however take advantage of this Fabry-Perot resonances to measure the group index values up to $n_g \sim 90$.

During my PhD it was not possible to optimize further the coupler, fabricate and test new designs. We preferred to apply the method as it is to active structures and to have a first insight on their nonlinear response. This is the purpose of the next chapter.

Active W1 waveguides

Contents

7.1	Experimental method	115
7.2	Experimental results	117

This chapter presents preliminary experimental results on the combination of slow light based on the CPO effect and slow mode in photonic crystal waveguides, as calculated in chapter 5. Experiments were performed using W1 PhC waveguide containing semiconductor quantum wells (QWs) as active, absorptive, nonlinear medium and exploiting the vertical coupled described in chapter 6. The pump and probe beams are generated by the intensity modulation of a single laser beam. Delay measurements of the probe signal are performed using a lock-in amplifier. We show delays in this photonic crystal waveguides going up to 2 μ s.

7.1 Experimental method

In this section we present the characteristics of the W1 PhC WGs sample and the experimental set-up used for the nonlinear measurements.

The photonic crystals (PhCs) are 10 μ m x 500 μ m air hole triangular lattice InP suspended membranes. As in the passive samples, the waveguide is placed in the center of the short side of the PhC. The W1 waveguide is generated by missing a row of holes (in the long axis) during the fabrication. Two couplers are also introduced in this line defect setting the propagating length L_p .

The fabrication process has been described in section 4.1. The PhC period and hole radius are $a = 430$ nm and $r = 115$ nm, respectively. The PhC suspended InP membrane (265 nm-thick, $\lambda/2n$) is grown by metalorganic vapour phase epitaxy (MOCVD), containing four central layers of InGaAs/InGaAsP QWs (see figure 4.3.a), each layer having a thickness of ~ 13.5 nm and ~ 16 nm for the well and the barrier, respectively.

As done for the cavity, we first perform a photoluminescence study of the QWs. The experimental set up used for the photoluminescence is the same as that used for the cavities, shown in figure 4.5. The sample is pumped using a pulsed Ti:Sa laser source emitting at 810 nm, having a 80 MHz-repetition rate and 100 fs-pulse duration. The pump is focused on the sample with a 20X microscope objective. The emission is collected by the same objective and send to, either a CCD camera

in order to visualize the sample, or a spectrometer ('Princeton Instruments', Acton SP2500i, with a 600 g/mm grating 1.6 μm blaze and Ni cooled camera) to record the spectrum of the QWs fluorescence. After passing through the spectrometer the signal is sent to an InGaAs 1D array spectroscopy camera ('Princeton Instruments', OMA V, spectral range 0.7 μm -1.6 μm , resolution FWHM: 0.315 nm). Figure 7.1 shows a typical photoluminescence spectrum for a pump average power of 70 μW .

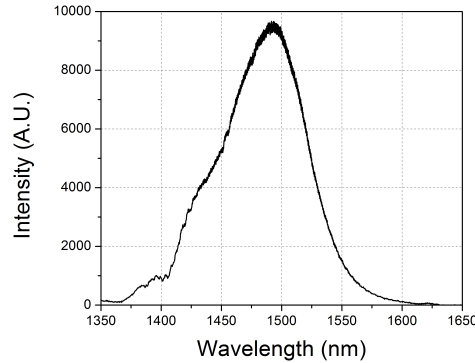


Figure 7.1: Quantum wells photoluminescence spectrum.

Coupling into the waveguide is achieved using the vertical coupler with a period increase in the propagation direction $a' - a = 30$ nm ($a' = 460$ nm) and an increment/reduction of the hole radius in the lines adjacent to the missing line $\Delta r = 35$ nm. Samples with 3 different lengths $L = 50; 100; 200$ μm were fabricated. Figure 7.2 presents the experimental set-up used, it is almost the same as the one used for the measurements on passive waveguides, see figure 6.14, with two modifications.

We use a fibered acousto-optic modulator (AOM) to generate a sine-wave modulation of the signal coupled into the W1 waveguide and a supplementary laser emitting at 800 nm wavelength (Ref. Diode Thorlabs) impinging on the sample at oblique incidence (i.e. without passing through the microscope objective).

This laser, focused using a lens ($f=100$ mm), is used to pump the quantum wells. An infrared camera is then used to detect the fluorescence of the QWs and determine optically the location of the couplers. Figure 7.3 shows a picture of the sample taken with the infrared camera as it is pumped with the 800 nm laser. The brighter parts of the waveguides are the couplers, three waveguide lengths ($L = 50, 100, 200$ μm) between the couplers are clearly visible.

To generate the pump and probe beams a sinusoidal modulation of the *Tunics* intensity is performed, as it was done in section 4.3. The amplitude modulation is generated via a fibered acousto-optic modulator at a frequency, δ , of 100 kHz.

The pump intensity is measured in the same way as the transmitted intensity in the passive waveguides (see section 6.2.2), i.e. we use the IR camera to measure the intensity at the extraction coupler. Alternatively, as shown in the same section, spatial filtering can also be implemented by confocal detection; in this case, the

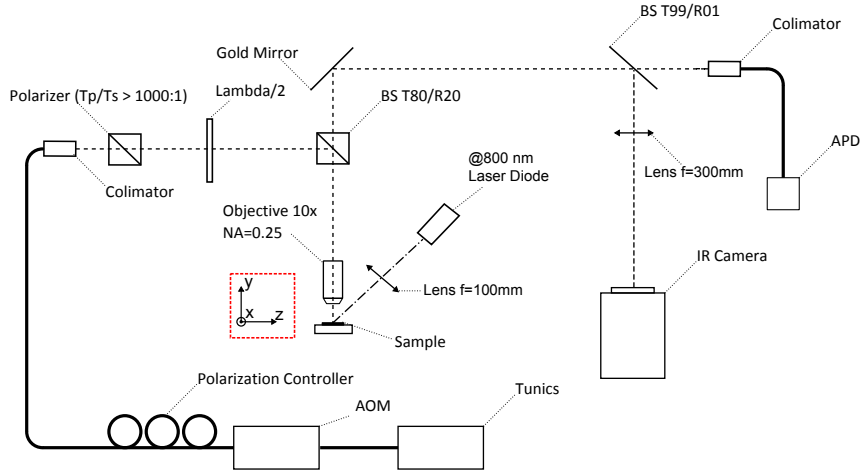


Figure 7.2: Experimental set-up used to perform the measurements of the active W1 photonic crystal waveguides.

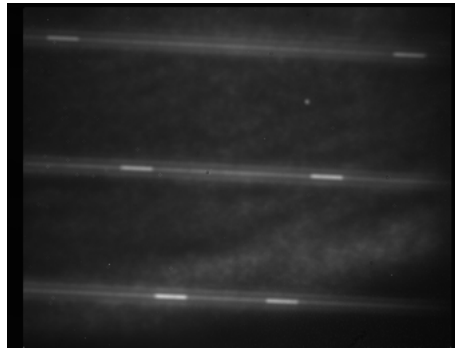


Figure 7.3: Infrared picture of the sample (taken with the InGaAs camera) of the sample with $a = 430$ nm, $a' = 460$ nm, $r = 115$ nm, $e = 265$ nm. The picture shows three waveguides with lengths (distance between couplers) $L = 50, 100, 200$ μm .

transmitted signal is detected through an APD and using a lock-in detector we obtain the amplitude and phase of the modulation (i.e. intensity and delay of the probe). Since the modulation frequency is 100 kHz, a commercial lock-in (Stanford Research Systems-SR830) is used this time.

7.2 Experimental results

The first experimental measurement in the active waveguides is simply a repetition of the one performed in the passive ones.

The transmission spectrum there is measured by integrating the intensity of the IR camera pixels in the extraction coupler region, for each frequency. Figure 7.4 shows the transmission spectrum (black line) and group index, calculated using the free spectral range, (red square ■) for a waveguide with a lattice period $a = 430$ nm,

a radius $r = 115$ nm and a length $L = 50$ μm . The pump intensity is 20 μW .

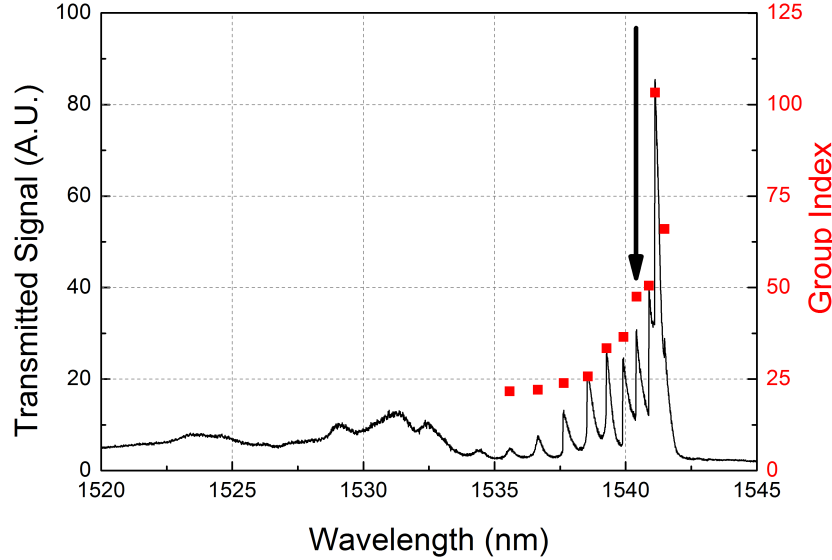


Figure 7.4: Transmission spectrum (black line) and group index as a function of the wavelength (■) for a W1 PhC WG with a propagation length $L_p = 50$ μm , $a = 430$ nm triangular lattice period, $r = 115$ nm hole radius and $a' = 460$ nm period of the coupler in the direction of propagation.

The transmission spectrum of figure 7.4 does not exhibit a lower limit in the wavelength range considered and the cut-off at high wavelength is approximately 1543 nm. As in the case of absorption free samples (chapter 6) Fabry-Perot resonances are observed before the cut-off, while transmission variation is smooth between 1520 and 1535 nm. From the Fabry-Perot peaks the free spectral range can be measured and the group index evaluated. It varies from 20 at 1536 nm to 80 at 1541.5 nm.

Strong nonlinear behaviors are already presents in the transmission spectrum presented figure 7.4, obtained for a pump power of 20 μW . Indeed, with the exception of the resonances around 1535 nm, all the others present a steep profile at the blue side. This is strongly reminiscent of the nonlinear response of the cavities studied in chapter 4. The steepness at the blue side of the resonance is a signature of the electronic origin of the nonlinear response.

To further investigate this response figure 7.5.a presents transmission spectra around the Fabry-Perot resonances (1535 nm-1543 nm) for different pump powers. It becomes clear that even for the lowest powers investigated most of the resonances are non symmetric and exhibit its nonlinear behavior. This strong nonlinearity is clearly not associated to the finesse of the Fabry-Perot peaks, but rather to the length of the nonlinear interaction.

Figure 7.5.b presents the transmission spectra of the probe (modulation ampli-

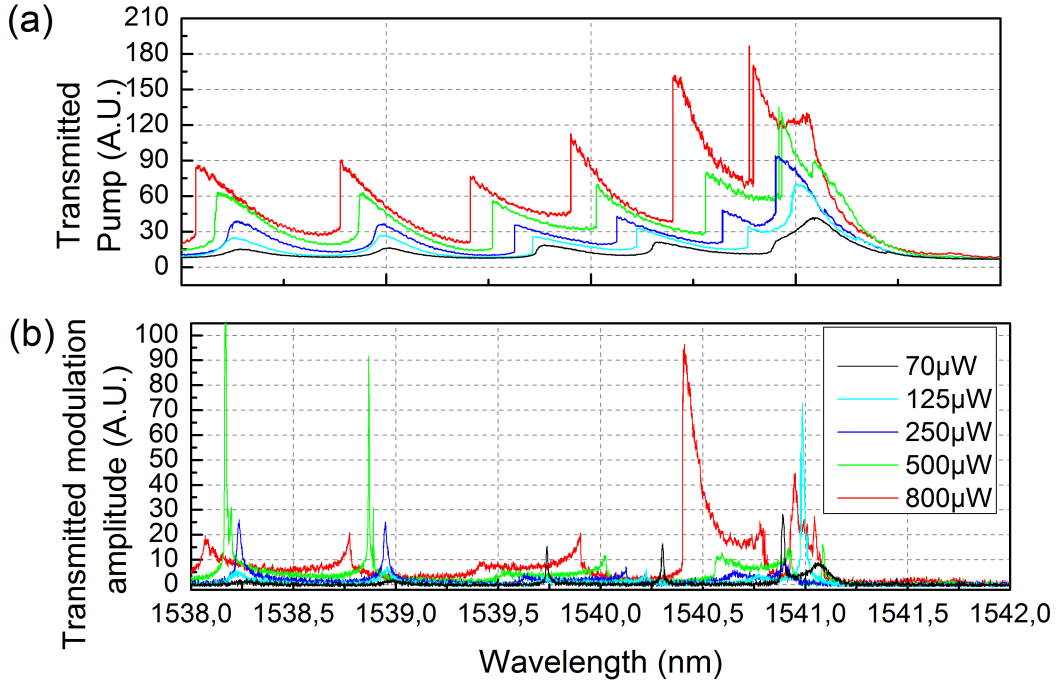


Figure 7.5: (a) Pump transmission spectrum. (b) Probe transmission spectrum. Black 70 μW , light blue 125 μW , blue 250 μW , green 500 μW , red 800 μW laser intensity. For a W1 PhC WG with a propagation length $L_p = 50 \mu\text{m}$, $a = 430 \text{ nm}$ triangular lattice period, $r = 115 \text{ nm}$ hole radius and $a' = 460 \text{ nm}$ period of the coupler in the direction of propagation.

tude). Very narrow resonances are seen in coincidence with the steep slope wavelength of the pump resonances. Most of the probe resonances are not appearing in the measurement due to the step resolution of the wavelength scan.

In order to analyze as a very preliminary result the nonlinearly induced delay we will now focus on the resonance at 1540.43 nm labeled by an arrow in figure 7.4. We focus our studies in this maximum because it represent a good compromise between the intensity of the signal and the spectral width of the probe.

Figure 7.6.a shows the transmitted pump intensity as the laser wavelength is tuned around the resonance (1540.53 nm) measured with the IR camera for the different laser powers, we can see that as the power increases the resonance becomes larger, and more importantly asymmetric as the blue side slope becomes steeper than the red side slope of the resonance. Figure 7.6.b shows the probe intensity (modulation amplitude) as the laser wavelength is tuned, we can see that the resonances are centered around the respective pump blue side slope. Also that as the laser power increases and the pump blue side slope becomes steeper, the probe res-

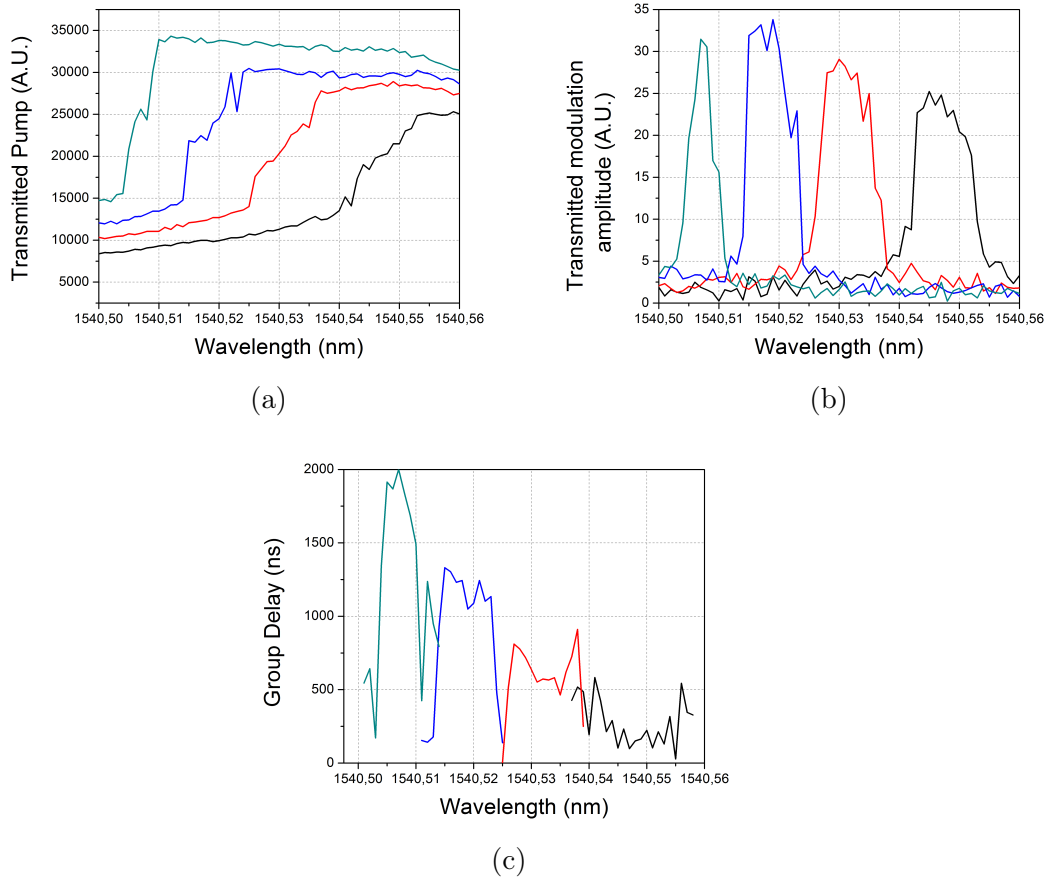


Figure 7.6: (a) Pump, (b) probe and (c) delay spectra for a W1 waveguide of $50 \mu\text{m}$ length with difference between the period of the waveguide, $a = 430 \text{ nm}$, a period of the coupler in the direction of propagation, $a' = 460 \text{ nm}$ and a radius $r = 115 \text{ nm}$; for different pump intensities ($60 \mu\text{W}$ black, $70 \mu\text{W}$ red, $80 \mu\text{W}$ blue, $90 \mu\text{W}$ green).

onance becomes narrower. Finally, figure 7.6.c shows the probe delay as a function of the laser wavelength, the maximum delay wavelength is centered in the probe resonance (also, the steep slope of the pump resonance) as in the L3 PhC cavities, exhibiting a clear nonlinear behavior. The maximum delay achieved is $2 \mu\text{s}$ for a pump intensity of $90 \mu\text{W}$. One may think that larger delay could be achieved by simply increasing the laser power, however, as we enhance the laser power the probe resonance becomes narrower and the hole system becomes too unstable to perform the delay measurements.

The origin of this delay enhancement comes, as in the L3 PhC cavity from a combination of effects, including both the CPO effect and nonlinear behavior showed by the asymmetry of the resonance. Nevertheless, in this case we do not have developed yet the theoretical model to compare to the experimental result as it becomes really difficult to estimate: the absorption of QWs, the linewidth

enhancement factor and the coupling rate.

In conclusion, we have demonstrated vertical coupling in active slow-light photonic crystal waveguides, allowing propagation distances of some tens of micrometers. We have measured the group index of the W1 PhC waveguide for values from 20 to 80 through a Fabry-Perot method. We have showed that the coupler acts as a mirror creating a cavity that (because of the presence of the QWs) has a clear nonlinear behavior attaining delays up to 2 μ s.

This system requires further studies as the high reflection of the vertical coupler have not allowed until now to make simple one way transmission measurements on the waveguide and we are forced to work on the cavity regime. Nowadays we are working to reduce the reflection of the coupler.

Part IV

Conclusions and prospects

Conclusions and prospects

8.1 Conclusions

Slow light propagation is at the heart of intense research since two decades. There are many possible applications of slow light in non-linear optics, quantum optics and telecommunications. Usually there are two principal approaches material dispersion and material structuration. Material dispersion is originated by nonlinear interactions, such as Electromagnetically Induced Transparency (EIT) or Coherent Population Oscillation (CPO). The alternative option is to achieve slow light based on the moulding of the photonic dispersion diagram via the geometrical engineering of the optical properties. This is particularly the case in 2D Photonic Crystals (2D PhC) where slow light modes can be achieved both as Bloch states in non defective structures that acts as distributed resonators and in defective 2D PC where a missing row of holes created the so called W1 waveguides that can also host a slow mode. In both cases the flat photonic band dispersion $E(k)$ is designed by adjusting the opto-geometrical parameters in order to induce the slow group velocity ($dE(k)/dk$). Additionally large delays can be obtained using resonators. The purpose of this thesis was to combine slow light by material dispersion with photonic crystal cavities and slow mode photonic crystal waveguides.

We have proposed a simple approach, which can be analytically solved, to describe coherent population oscillations in a nonlinear microcavity. The analytical model enables us to discuss the physical processes which lead both to a strong enhancement of the Q -factor and to a control of the transmission at the probe frequency. The simultaneous action of population oscillations and the nonlinear response of the cavity induces a strong intracavity dispersion and a differential gain. This technique could be used to stabilize a microcavity using the frequency pulling effect for example. Finally, it is also possible to take advantage of the active control of the Q -factor via the pump beam in optical pulse buffering applications.

We have also shown some of our predictions experimentally demonstrating that the Q -factor of a nanocavity can be dynamically and strongly enhanced by the cooperative use of CPO and dispersive nonlinearities. The numerical model we developed describes these experimental results and a good agreement between the experimental measurements and the theoretical model was obtained. The predicted frequency pulling effect was also experimentally demonstrated and can be used to lock the enhanced Q -factor nanocavity to a desired wavelength. It can also be implemented to compensate for technological errors or to lock several nanocavities to the same wavelength.

Concerning photonic crystal waveguides, we developed a simple perturbative model that allows to predict the absorption and group index behaviour in a system where we combine slow light by CPO and slow mode W1 PhC waveguides. The model shows that the total group index has a linear dependence with each one of the group indices while the absorption has linear dependence with the slow mode group index and does not depend on the CPO group index.

We extended to PhC waveguides (WGs) the band-folding procedure already applied to PhC cavities. By adding a periodical perturbation in the region before and after the waveguide short couplers are designed able to insert (extract) the light in (from) the waveguide. This couplers have a quite large wavelength and group velocities acceptance into a reduced angle range. For instance with a given set of parameters the whole range of $5 < n_g < 100$ can be addressed within a reasonable coupling angle range of $-4^\circ < \theta < 6^\circ$. We design and fabricated InP based W1 suspended PhC WG and demonstrated the couplers ability over a > 50 nm spectral range and we take benefit from Fabry-Perot oscillations to assess the group index of the W1.

We have also performed preliminary nonlinear tests on active W1 PhC WG where light is coupled and extracted thanks to the proposed band-folding approach. The system exhibits a strong nonlinear response for low pump powers. Group delays were measured on the Fabry-Perot resonances reaching values as high as $2 \mu\text{s}$.

8.2 Prospects

During my PhD these I studied the CPO effect in semiconductor photonic crystals, showing theoretical and experimentally that this effect enables to enhance the lifetime in photonic crystal cavities. The experimental measures were done in a shifted L3 PhC cavity and the active material were semiconductor quantum wells. Theoretical studies also predict signal amplification, an issue of particular interest since it could compensate absorptive, diffusive and nanocavity coupling losses; however, this signal amplification could not be done experimentally during this thesis; this is mainly due to the difficulties calibrating the incoming power in the tapered fiber configuration. In order to perform these measures a study of free space coupling alternative to the tapered fiber was done in our laboratory to achieve vertical coupling using the band folding technique [Haddadi 2012].

Work done on erbium-doped fiber amplifiers has shown that the utilization of a forced modulated pump enables to enhance the relative phase delay obtained with the CPO effect by an order of magnitude [Arrieta-Yañez 2009]. This is an interesting approach to be applied for our semiconductor active PhC. In this case we should consider a three-level system as sketched in figure 8.1 where we have levels $|1\rangle$ and $|2\rangle$ that are connected via Ω_s and a third level $|3\rangle$ that is connected to $|1\rangle$ via Ω_p . The decay rate from $|3\rangle$ to $|2\rangle$ is much faster than the one from $|2\rangle$ to $|1\rangle$ (lifetime τ). Using the modulated source approach employed during this thesis we would send a signal at frequency $\omega \sim \Omega_s$ with a small amplitude modulation at

$\delta < 1/\tau$. In this case additionally to that signal we should send a second beam at $\omega \sim \Omega_p$ also modulated at δ enhancing the population oscillation as the decay from $|3\rangle$ to $|2\rangle$ is fast and achieving then an enhancement of the delay. We expect to use this technique in semiconductors; particularly, the experimental set-up described in chapter 7 would allow such experiment.

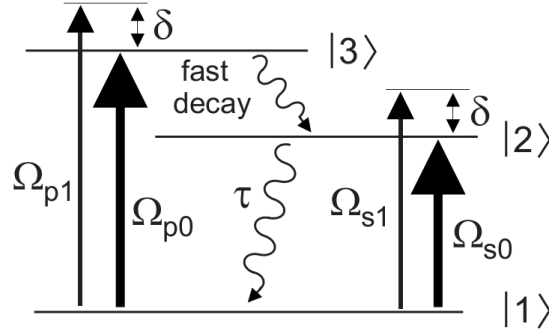


Figure 8.1: Three-level atom with the control (Rabi frequency Ω_{s0}) and the probe (Rabi frequency Ω_{s1}) signal fields coupling $|1\rangle$ to the excited state $|2\rangle$. The strong (Rabi frequency Ω_{p0}) and weak (Rabi frequency Ω_{p1}) pump fields couple the ground state $|1\rangle$ to the fast decaying excited state $|3\rangle$. The Rabi frequencies are expressed in frequency units [Arrieta-Yañez 2009].

The work on W1 photonic crystal waveguides done in this thesis showed a system enabling us to couple from free space into the W1 PhC WG. We have shown experimentally that this system allows us to couple into short ($\sim 50 \mu\text{m}$) active (semiconductor QWs) PhC WGs. We have also shown measures of the group index of such a waveguide up to $n_g = 80$. The utilization of this system suffers however from a relatively high reflection of the coupler that have not allowed until now to make a simple one way transmission measurement on the waveguide. We were forced to work on the cavity regime.

The very long delay achieved is very promising, since this reflection *transforms* the waveguide in a Fabry-Perot cavity that shows nonlinear response even for low pump intensities.

However, it would be very interesting to achieve the situation we envisaged for the WG: that is single pass long delays coupling reasonable n_g associated to the PhC slow mode and CPO effect. A next step is thus to improve the vertical coupler design to decrease the reflectivity and increase the out of plane coupling. The introduction of CPO in a slow mode PhC WG would allow us to increase the delay without increasing the losses. Additionally, this increase on the delay would be optically controlled.

Bibliography

- [Akahane 2003] Yoshihiro Akahane, Takashi Asano, Bong-Shik Song and Susumu Noda. *High-Q photonic nanocavity in a two-dimensional photonic crystal*. Nature, vol. 425, no. 6961, pages 944–947, 2003. (Cited on pages 17, 23 and 48.)
- [Aoki 2009] Takao Aoki, A. S. Parkins, D. J. Alton, C. A. Regal, Barak Dayan, E. Ostby, Kerry J. Vahala and H. J. Kimble. *Efficient routing of single photons by one atom and a microtoroidal cavity*. Physical review letters, vol. 102, no. 8, page 083601, February 2009. (Cited on page 23.)
- [Arnold 2009] S. Arnold, D. Keng, S. I. Shopova, S. Holler, W. Zurawsky and F. Vollmer. *Whispering Gallery Mode Carousel -a photonic mechanism for enhanced nanoparticle detection in biosensing*. Optics Express, vol. 17, no. 8, pages 6230–8, April 2009. (Cited on page 23.)
- [Arrieta-Yañez 2009] Francisco Arrieta-Yañez, Sonia Melle, Oscar Calderón, M. A. Antón and F. Carreño. *Phase tunability of group velocity by modulated-pump-forced coherent population oscillations*. Physical Review A, vol. 80, no. 1, page 011804, July 2009. (Cited on pages 126 and 127.)
- [Baba 2008] Toshihiko Baba. *Slow light in photonic crystals*. Nature Photonics, pages 465–473, 2008. (Cited on pages 18 and 77.)
- [Baldit 2005] Elisa Baldit, Kamel Bencheikh, Paul Monnier, Juan Ariel Levenson and V. Rouget. *Ultraslow Light Propagation in an Inhomogeneously Broadened Rare-Earth Ion-Doped Crystal*. Physical Review Letters, vol. 95, no. 14, page 143601, 2005. (Cited on pages v, 4, 7, 8, 11, 56 and 77.)
- [Barclay 2003] Paul E. Barclay, Kartik Srinivasan and Oskar Painter. *Design of photonic crystal waveguides for evanescent coupling to optical fiber tapers and integration with high-Q cavities*. Journal of the Optical Society of America B, vol. 20, no. 11, page 2274, 2003. (Cited on page 93.)
- [Bigelow 2003a] Matthew S. Bigelow, Nick N. Lepeshkin and Robert W. Boyd. *Observation of Ultraslow Light Propagation in a Ruby Crystal at Room Temperature*. Physical Review Letters, vol. 90, no. 11, page 113903, March 2003. (Cited on pages 7, 8, 26, 56 and 77.)
- [Bigelow 2003b] Matthew S. Bigelow, Nick N. Lepeshkin and Robert W. Boyd. *Superluminal and slow light propagation in a room-temperature solid*. Science (New York, N.Y.), vol. 301, no. 5630, pages 200–2, July 2003. (Cited on pages 7, 8, 11 and 77.)

- [Boller 1991] K.-J. Boller, Atac Imamoglu and Stephen E. Harris. *Observation of Electromagnetically Induced Transparency*. Physical Review Letters, vol. 66, no. 20, pages 2593–2596, 1991. (Cited on pages 7 and 77.)
- [Bonifacio 1979] R. Bonifacio and P. Meystre. *Critical slowing down in optical bistability*. Optics Communications, vol. 29, no. 1, pages 131–134, 1979. (Cited on page 45.)
- [Boyd 1981] Robert W. Boyd, Michael G. Raymer, Paul Narum and Donald J. Harter. *Four-wave parametric interactions in a strongly driven two-level system*. Physical Review A, vol. 24, no. 1, pages 411–423, 1981. (Cited on pages v, 4 and 26.)
- [Boyd 2003] Robert W. Boyd. Nonlinear Optics. Academic Press, second édition, 2003. (Cited on pages 8 and 37.)
- [Brunstein 2009] Maia Brunstein, Remy Braive, Richard Hostein, Alexios Beveratos, Isabelle Robert-Philip, Isabelle Sagnes, Timothy J. Karle, Alejandro M. Yacomotti, Juan Ariel Levenson, Virginie Moreau, Gilles Tessier and Yannick De Wilde. *Thermo-optical dynamics in an optically pumped Photonic Crystal nano-cavity*. Optics Express, vol. 17, no. 19, pages 17118–29, September 2009. (Cited on page 52.)
- [Brunstein 2011] Maia Brunstein. *Nonlinear Dynamics in III-V Semiconductor Photonic Crystal Nano-cavities*. PhD thesis, Université Paris Sud (XI), 2011. (Cited on pages 34, 51 and 52.)
- [Chang 2004] Shu-Wei Chang, Shun-Lien Chuang, Pei-Cheng Ku, Connie J. Chang-Hasnain, Phedon Palinginis and Hailin Wang. *Slow light using excitonic population oscillation*. Physical Review B, vol. 70, no. 23, page 235333, December 2004. (Cited on page 8.)
- [Chang 2005] Shu-Wei Chang and Shun-Lien Chuang. *Slow light based on population oscillation in quantum dots with inhomogeneous broadening*. Physical Review B, vol. 72, no. 23, page 235330, December 2005. (Cited on pages 7, 8 and 11.)
- [Chembo 2010] Yanne K. Chembo, Dmitry V. Strekalov and Nan Yu. *Spectrum and Dynamics of Optical Frequency Combs Generated with Monolithic Whispering Gallery Mode Resonators*. Physical Review Letters, vol. 104, no. 10, page 103902, March 2010. (Cited on page 23.)
- [Daunois 1988] A. Daunois and J. Y. Bigot. *Switching dynamics of optical bistable devices*. Applied Physics B Photophysics and Laser Chemistry, vol. 45, no. 3, pages 157–162, March 1988. (Cited on page 45.)
- [Dumeige 2008] Yannick Dumeige, Stéphane Trebaol, Laura Ghisa, Thi Kim Ngân Nguyễn, Hervé Tavernier and Patrice Féron. *Determination of coupling regime of high-Q resonators and optical gain of highly selective amplifiers*.

- Journal of the Optical Society of America B, vol. 25, no. 12, pages 2073–2080, 2008. (Cited on page 23.)
- [Dumeige 2009a] Yannick Dumeige. *Stopping and manipulating light using a short array of active microresonators*. EPL (Europhysics Letters), vol. 86, no. 1, page 14003, April 2009. (Cited on page 23.)
- [Dumeige 2009b] Yannick Dumeige, Stéphane Trebaol and Patrice Féron. *Intracavity coupled-active-resonator-induced dispersion*. Physical Review A, vol. 79, no. 1, page 013832, January 2009. (Cited on page 27.)
- [Dumeige 2012] Yannick Dumeige, Alejandro M. Yacomotti, Patricio Grinberg, Kamel Bencheikh, E. Le Cren and Juan Ariel Levenson. *Microcavity-quality-factor enhancement using nonlinear effects close to the bistability threshold and coherent population oscillations*. Physical Review A, vol. 85, no. 6, page 063824, June 2012. (Cited on page 25.)
- [Fizeau 1849] Hippolyte Fizeau. *Sur une expérience relative a la vitesse de propagation de la lumiere*. Comptes Rendus de l'Académie des sciences, vol. 29, pages 90–92; 132, 1849. (Cited on pages v and 3.)
- [Fleischhauer 2005] Michael Fleischhauer, Atac Imamoglu and Jonathan P. Marangos. *Electromagnetically induced transparency: Optics in coherent media*. Reviews of Modern Physics, vol. 77, no. 2, pages 633–673, 2005. (Cited on pages 7 and 77.)
- [Frandsen 2006] Lars H. Frandsen, Andrei V. Lavrinenko, Jacob Fage-Pedersen and Peter I. Borel. *Photonic crystal waveguides with semi-slow light and tailored dispersion properties*. Optics Express, vol. 14, no. 20, page 9444, October 2006. (Cited on page 19.)
- [Gibbs 1976] H. M. Gibbs, S. L. McCall and T. N. C. Venkatesan. *Differential gain and bistability using a sodium-filled Fabry-Perot interferometer*. Physical Review Letters, vol. 36, no. 19, pages 1135–1138, 1976. (Cited on page 37.)
- [Gibbs 1985] H. M. Gibbs. *Optical Bistability: Controlling Light With Light*. Academic Press, New York, 1985. (Cited on page 40.)
- [Goorskey 2002] D. J. Goorskey, Hai Wang, W. H. Burkett and Min Xiao. *Effects of a highly dispersive atomic medium inside an optical ring cavity*. Journal of Modern Optics, vol. 49, no. 1-2, pages 305–317, 2002. (Cited on page 23.)
- [Grinberg 2012] Patricio Grinberg, Kamel Bencheikh, Maia Brunstein, Alejandro M. Yacomotti, Yannick Dumeige, Isabelle Sagnes, Fabrice Raineri, Laurent Bigot and Juan Ariel Levenson. *Nanocavity Linewidth Narrowing and Group Delay Enhancement by Slow Light Propagation and Nonlinear Effects*. Physical Review Letters, vol. 109, no. September, page 113903, 2012. (Cited on page 47.)

- [Haddadi 2012] Samir Haddadi, Luc Le-Gratiet, Isabelle Sagnes, Fabrice Raineri, Alexandre Bazin, Kamel Bencheikh, Juan Ariel Levenson and Alejandro M. Yacomotti. *High quality beaming and efficient free-space coupling in L3 photonic crystal active nanocavities*. Optics Express, vol. 20, no. 17, pages 18876–18886, 2012. (Cited on page 126.)
- [Hamachi 2009] Yohei Hamachi, Shousaku Kubo and Toshihiko Baba. *Slow light with low dispersion and nonlinear enhancement in a lattice-shifted photonic crystal waveguide*. Optics Letters, vol. 34, no. 7, page 1072, April 2009. (Cited on page 19.)
- [Hau 1999] Lene Vestergaard Hau, Stephen E. Harris, Zachary Dutton and Cyrus H. Behroozi. *Light speed reduction to 17 metres per second in an ultracold atomic gas*. Nature, vol. 397, no. February, pages 594–598, 1999. (Cited on pages v, 4, 7 and 77.)
- [Haus 1984] H. A. Haus. Waves and Fields in Optoelectronics. Prentice-Hall, Englewood Cliffs, NJ, 1984. (Cited on page 33.)
- [Henry 1982] C. Henry. *Theory of the linewidth of semiconductor lasers*. IEEE Journal of Quantum Electronics, vol. 18, no. 2, pages 259–264, 1982. (Cited on page 34.)
- [Hillman 1983] Lloyd W. Hillman, Robert W. Boyd, Jerzy Krasinski and C. R. Stroud. *Observation of a spectral hole due to population oscillations in a homogeneously broadened optical absorption line*. Optics Communications, vol. 45, no. 6, pages 416–419, 1983. (Cited on page 7.)
- [Hugonin 2005] Jean-Paul Hugonin and Philippe Lalanne. *Perfectly matched layers as nonlinear coordinate transforms: a generalized formalization*. Journal of the Optical Society of America. A, Optics, image science, and vision, vol. 22, no. 9, pages 1844–9, September 2005. (Cited on page 101.)
- [Hugonin 2007] Jean-Paul Hugonin, Philippe Lalanne, Thomas P. White and Thomas F. Krauss. *Coupling into slow-mode photonic crystal waveguides*. Optics letters, vol. 32, no. 18, pages 2638–40, September 2007. (Cited on pages 93 and 94.)
- [Hwang 2005] In-Kag Hwang, Sun-Kyung Kim, Jin-Kyu Yang, Se-Heon Kim, Sang Hoon Lee and Yong-Hee Lee. *Curved-microfiber photon coupling for photonic crystal light emitter*. Applied Physics Letters, vol. 87, no. 13, page 131107, 2005. (Cited on page 53.)
- [Ilchenko 2006] Vladimir S. Ilchenko and Andrey B. Matsko. *Optical resonators with whispering-gallery modes-part II: applications*. IEEE Journal of Selected Topics in Quantum Electronics, vol. 12, no. 1, pages 15–32, 2006. (Cited on page 23.)

- [Inouye 2000] S. Inouye, R. F. Low, S. Gupta, T. Pfau, A. Gorlitz, T. L. Gustavson, D. E. Pritchard and W. Ketterle. *Amplification of light and atoms in a bose-einstein condensate*. Physical review letters, vol. 85, no. 20, pages 4225–8, November 2000. (Cited on pages 7 and 77.)
- [Joannopoulos 2008] John D. Joannopoulos, Steven G Johnson, Joshua N. Winn and Robert D. Meade. Photonic crystals: molding the flow of light. Princeton University Press, Singapore, second édition, 2008. (Cited on pages 15 and 16.)
- [Kapon 1999] Eli Kapon. Semiconductor Laser I: Fundamentals. Academic Press, New York, 1999. (Cited on page 34.)
- [Karle 2010] Timothy J. Karle, Yacine Halioua, Fabrice Raineri, Paul Monnier, Remy Braive, Luc Le-Gratiet, Gregoire Beaudoin, Isabelle Sagnes, G. Roelkens, Frederik Van Laere, Dries Van Thourhout and Rama Raj. *Heterogeneous integration and precise alignment of InP-based photonic crystal lasers to complementary metal-oxide semiconductor fabricated silicon-on-insulator wire waveguides*. Journal of Applied Physics, vol. 107, no. 6, page 063103, 2010. (Cited on page 49.)
- [Kasapi 1995] A. Kasapi, Maneesh Jain, G. Y. Yin and Stephen E. Harris. *Electromagnetically induced transparency: propagation dynamics*. Physical review letters, vol. 74, no. 13, pages 2447–2451, 1995. (Cited on pages 7 and 77.)
- [Kash 1999] Michael M. Kash, Vladimir A. Sautenkov, Alexander S. Zibrov, L. Hollberg, George R. Welch, Mikhail D. Lukin, Yuri Rostovtsev, Edward S. Fry and Marlan O. Scully. *Ultraslow Group Velocity and Enhanced Nonlinear Optical Effects in a Coherently Driven Hot Atomic Gas*. Physical Review Letters, vol. 82, no. 26, pages 5229–5232, June 1999. (Cited on pages 7 and 77.)
- [Kawasaki 2007] Takashi Kawasaki, Daisuke Mori and Toshihiko Baba. *Experimental observation of slow light in photonic crystal coupled waveguides*. Optics Express, vol. 15, no. 16, pages 10274–10281, 2007. (Cited on page 19.)
- [Kim 2004] J. Kim, Shun-Lien Chuang, Pei-Cheng Ku and Connie J. Chang-Hasnain. *Slow light using semiconductor quantum dots*. Journal of Physics: Condensed Matter, vol. 16, no. 35, pages S3727–S3735, September 2004. (Cited on page 7.)
- [Krauss 2007] Thomas F. Krauss. *Slow light in photonic crystal waveguides*. Journal of Physics D: Applied Physics, vol. 40, no. 9, pages 2666–2670, 2007. (Cited on pages 18 and 77.)
- [Ku 2004] Pei-Cheng Ku, Forrest Sedgwick, Connie J. Chang-Hasnain, Phedon Palinginis, Tao Li, Hailin Wang, Shu-Wei Chang and Shun-Lien Chuang.

- Slow light in semiconductor quantum wells*. Optics letters, vol. 29, no. 19, pages 2291–2293, 2004. (Cited on pages 7, 8, 11, 12 and 77.)
- [Kuramochi 2005] Eiichi Kuramochi, Masaya Notomi, S Hughes, Akihiko Shinya, T. Watanabe and L. Ramunno. *Disorder-induced scattering loss of line-defect waveguides in photonic crystal slabs*. Physical Review B, vol. 72, no. 16, page 161318, 2005. (Cited on page 99.)
- [Lalanne 2002] Philippe Lalanne. *Electromagnetic analysis of photonic crystal waveguides operating above the light cone*. IEEE Journal of Quantum Electronics, vol. 38, no. 7, pages 800–804, 2002. (Cited on pages 89, 100 and 108.)
- [Lauprêtre 2011] T. Lauprêtre, C. Proux, R. Ghosh, S. Schwartz, F. Goldfarb and Fabien Bretenaker. *Photon lifetime in a cavity containing a slow-light medium*. Optics letters, vol. 36, no. 9, pages 1551–3, May 2011. (Cited on page 23.)
- [Lecamp 2007] G. Lecamp, Jean-Paul Hugonin and Philippe Lalanne. *Theoretical and computational concepts for periodic optical waveguides*. Optics express, vol. 15, no. 18, pages 11042–60, September 2007. (Cited on pages 87, 94, 101 and 109.)
- [Lee 2008] Michael W. Lee, Christian Grillet, Christopher G. Poulton, Christelle Monat, Cameron L. C. Smith, Eric Mägi, Darren Freeman, Steve Madden, Barry Luther-Davies and Benjamin J. Eggleton. *Characterizing photonic crystal waveguides with an expanded k -space evanescent coupling technique*. Optics express, vol. 16, no. 18, pages 13800–8, September 2008. (Cited on page 93.)
- [Li 1997] Lifeng Li. *New formulation of the Fourier modal method for crossed surface-relief gratings*. Journal of the Optical Society of America A, vol. 14, no. 10, page 2758, October 1997. (Cited on page 101.)
- [Li 2010] Qiang Li, Tao Wang, Yikai Su, Min Yan and Min Qiu. *Coupled mode theory analysis of mode-splitting in coupled cavity system*. Optics express, vol. 18, no. 8, pages 8367–82, April 2010. (Cited on pages 39 and 58.)
- [Lorentz 1880] H. A. Lorentz. *Über die Beziehung zwischen der Fortpflanzung des Lichtes und der Körperdichte (About the relationship between the propagation of light and the body density)*. Wiedemann Ann., vol. 9, page 641, 1880. (Cited on pages v and 3.)
- [Lu 2010] Jesse Lu and Jelena Vuckovic. *Inverse design of nanophotonic structures using complementary convex optimization*. Optics Express, vol. 18, no. 4, pages 3793–804, February 2010. (Cited on page 23.)

- [Lukin 1998] Mikhail D. Lukin, Michael Fleischhauer, Marlan O. Scully and Vladimir L. Velichansky. *Intracavity electromagnetically induced transparency*. Optics letters, vol. 23, no. 4, pages 295–7, February 1998. (Cited on pages 23 and 42.)
- [Matsko 2006] Andrey B. Matsko and Vladimir S. Ilchenko. *Optical resonators with whispering-gallery modes-part I: basics*. IEEE Journal of Selected Topics in Quantum Electronics, vol. 12, no. 1, pages 3–14, 2006. (Cited on page 23.)
- [Mazoyer 2011a] Simon Mazoyer. *Lumière lente dans les guides à cristaux photoniques réels*. PhD thesis, Université Paris-Sud XI, 2011. (Cited on pages 105 and 112.)
- [Mazoyer 2011b] Simon Mazoyer, Alexandre Baron, Jean-Paul Hugonin, Philippe Lalanne and Andrea Melloni. *Slow pulses in disordered photonic-crystal waveguides*. Applied Optics, vol. 50, no. 31, pages G113–7, November 2011. (Cited on pages 109 and 110.)
- [McNab 2003] Sharee McNab, Nikolaj Moll and Yurii Vlasov. *Ultra-low loss photonic integrated circuit with membrane-type photonic crystal waveguides*. Optics express, vol. 11, no. 22, pages 2927–39, November 2003. (Cited on page 93.)
- [Minin 2004] Serge Minin, Matthew Robert Fisher and Shun-Lien Chuang. *Current-controlled group delay using a semiconductor Fabry-Perot amplifier*. Applied Physics Letters, vol. 84, no. 17, page 3238, 2004. (Cited on page 23.)
- [Mørk 2010] Jesper Mørk and Torben Roland Nielsen. *On the use of slow light for enhancing waveguide properties*. Optics Letters, vol. 35, no. 17, pages 2834–2836, 2010. (Cited on pages 5 and 78.)
- [Moharam 1995] M. G. Moharam, Eric B. Grann, Drew A. Pommet and T. K. Gaylord. *Formulation for stable and efficient implementation of the rigorous coupled-wave analysis of binary gratings*. Journal of the Optical Society of America A, vol. 12, no. 5, page 1068, May 1995. (Cited on page 101.)
- [Moreau 2010] Virginie Moreau, Gilles Tessier, Fabrice Raineri, Maia Brunstein, Alejandro M. Yacomotti, Rama Raj, Isabelle Sagnes, Juan Ariel Levenson and Yannick De Wilde. *Transient thermoreflectance imaging of active photonic crystals*. Applied Physics Letters, vol. 96, no. 9, page 091103, 2010. (Cited on pages 47 and 56.)
- [Mortensen 2007] Niels Asger Mortensen and Sanshui Xiao. *Slow-light enhancement of Beer-Lambert-Bouguer absorption*. Applied Physics Letters, vol. 90, no. 14, page 141108, 2007. (Cited on pages 78 and 89.)

- [Müller 1997] G. Müller, M. Müller, A. Wicht, R. H. Rinkleff and K. Danzmann. *Optical resonator with steep internal dispersion*. Physical Review A, vol. 56, no. 3, pages 2385–2389, 1997. (Cited on pages 23 and 27.)
- [Murray Sargent III 1978] Murray Sargent III. *Spectroscopic techniques based on Lamb's laser theory*. Physics Reports, vol. 43, no. 5, pages 223–265, 1978. (Cited on page 7.)
- [Nielsen 2009] Torben Roland Nielsen, Andrei V. Lavrinenko and Jesper Mørk. *Slow light in quantum dot photonic crystal waveguides*. Applied Physics Letters, vol. 94, no. 11, pages 113111–3, 2009. (Cited on pages 5 and 78.)
- [Notomi 2001] Masaya Notomi, K. Yamada, Akihiko Shinya, J. Takahashi, C. Takahashi and I. Yokohama. *Extremely Large Group-Velocity Dispersion of Line-Defect Waveguides in Photonic Crystal Slabs*. Physical Review Letters, vol. 87, no. 25, page 253902, 2001. (Cited on pages v, 4 and 18.)
- [Notomi 2004] Masaya Notomi, Akihiko Shinya, S. Mitsugi, Eiichi Kuramochi and H-Y. Ryu. *Waveguides, resonators and their coupled elements in photonic crystal slabs*. Optics express, vol. 12, no. 8, pages 1551–61, April 2004. (Cited on page 93.)
- [Oraevsky 2001] Anatolii N. Oraevsky, Alexander V. Yarovitsky and Vladimir L. Velichansky. *Frequency stabilisation of a diode laser by a whispering-gallery mode*. Quantum Electronics, vol. 31, no. 10, page 987, 2001. (Cited on page 23.)
- [Painter 1999] O. Painter, Jelena Vuckovic and A. Scherer. *Defect modes of a two-dimensional photonic crystal in an optically thin dielectric slab*. Journal of the Optical Society of America B, vol. 16, no. 2, pages 275–285, 1999. (Cited on page 16.)
- [Palinginis 2005a] Phedon Palinginis, Shanna Crankshaw, Forrest Sedgwick, Eui-Tae Kim, Michael Moewe, Connie J. Chang-Hasnain, Hailin Wang and Shun-Lien Chuang. *Ultraslow light (<200 m/s) propagation in a semiconductor nanostructure*. Applied Physics Letters, vol. 87, no. 17, page 171102, 2005. (Cited on pages 8 and 12.)
- [Palinginis 2005b] Phedon Palinginis, Forrest Sedgwick, Shanna Crankshaw, Michael Moewe and Connie J. Chang-Hasnain. *Room temperature slow light in a quantum-well waveguide via coherent population oscillation*. Optics Express, vol. 13, no. 24, pages 9909–9915, 2005. (Cited on pages 8 and 12.)
- [Peng 2006] Peng-Chun Peng, C. T. Lin, Hao-chung Kuo, Gray Lin, W. K. Tsai, Hung-Ping Yang, K. F. Lin, Jim Y. Chi, S. Chi and S. C. Wang. *Tunable optical group delay in quantum dot vertical-cavity surface-emitting laser at 10 GHz*. Electronics Letters, vol. 42, no. 18, pages 1036–1037, 2006. (Cited on page 23.)

- [Phillips 2001] D. Phillips, A. Fleischhauer, A. Mair, R. Walsworth and Mikhail D. Lukin. *Storage of Light in Atomic Vapor*. Physical Review Letters, vol. 86, no. 5, pages 783–786, January 2001. (Cited on pages v and 4.)
- [Pierce 1950] John Robinson Pierce. *Traveling-wave tubes*. The Bell System Technical Journal, vol. 29, no. 1, 1950. (Cited on pages v and 3.)
- [Piredda 2007] Giovanni Piredda and Robert W. Boyd. *Slow light by means of coherent population oscillations: laser linewidth effects*. Journal of the European Optical Society, vol. 2, page 07004, 2007. (Cited on page 34.)
- [Raineri 2009] Fabrice Raineri, Alejandro M. Yacomotti, Timothy J. Karle, Richard Hostein, Remy Braive, Alexios Beveratos, Isabelle Sagnes and Rama Raj. *Dynamics of band-edge photonic crystal lasers*. Optics express, vol. 17, no. 5, pages 3165–72, March 2009. (Cited on page 34.)
- [Rivoire 2011] Kelley Rivoire, Sonia Buckley, Arka Majumdar, Hyochul Kim, Pierre Petroff and Jelena Vuckovic. *Fast quantum dot single photon source triggered at telecommunications wavelength*. Applied Physics Letters, vol. 98, no. 8, page 083105, 2011. (Cited on page 23.)
- [Sakoda 2005] Kazuaki Sakoda. *Optical Properties of Photonic Crystals*. Springer, Berlin, second édition, 2005. (Cited on page 80.)
- [Sauvan 2004] Christophe Sauvan, Philippe Lalanne and Jean-Paul Hugonin. *Photonics: Tuning holes in photonic-crystal nanocavities*. Nature, vol. 429, no. 6988, pages 2003–2004, May 2004. (Cited on page 17.)
- [Sauvan 2005] Christophe Sauvan, Philippe Lalanne and Jean-Paul Hugonin. *Slow-wave effect and mode-profile matching in photonic crystal microcavities*. Physical Review B, vol. 71, no. 16, page 165118, 2005. (Cited on pages 17, 23 and 27.)
- [Savchenkov 2004] Anatoliy Savchenkov, Vladimir S. Ilchenko, Andrey B. Matsko and Lute Maleki. *Kilohertz optical resonances in dielectric crystal cavities*. Physical Review A, vol. 70, no. 5, page 051804, November 2004. (Cited on page 23.)
- [Scheerlinck 2007] Stijn Scheerlinck, Jonathan Schrauwen, Frederik Van Laere, Dirk Taillaert, Dries Van Thourhout and Roel Baets. *Efficient, broadband and compact metal grating couplers for silicon-on-insulator waveguides*. Optics express, vol. 15, no. 15, pages 9625–30, July 2007. (Cited on page 98.)
- [Scheerlinck 2008] Stijn Scheerlinck, Dirk Taillaert, Dries Van Thourhout and Roel Baets. *Flexible metal grating based optical fiber probe for photonic integrated circuits*. Applied Physics Letters, vol. 92, no. 3, page 031104, 2008. (Cited on page 98.)

- [Schwarz 1967] S. E. Schwarz and T. Y. Tan. *Wave Interactions in Saturable Absorbers*. Applied Physics Letters, vol. 10, no. 1, page 4, 1967. (Cited on page 7.)
- [Shinya 2008] Akihiko Shinya, Shinji Matsuo, Yosia, Takasumi Tanabe, Eiichi Kuramochi, Tomonari Sato, Takaaki Kakitsuka and Masaya Notomi. *All-optical on-chip bit memory based on ultra high Q InGaAsP photonic crystal*. Optics express, vol. 16, no. 23, pages 19382–7, November 2008. (Cited on page 23.)
- [Snyder 1983] A. W. Snyder and J. D. Love. *Optical waveguide theory*. Chapman and Hall, Bristol, 1983. (Cited on page 85.)
- [Soljačić 2004] Marin Soljačić and John D. Joannopoulos. *Enhancement of nonlinear effects using photonic crystals*. Nature Materials, vol. 3, no. 4, pages 211–219, 2004. (Cited on pages 4 and 78.)
- [Soljačić 2005a] Marin Soljačić, Elefterios Lidorikis, Lene Vestergaard Hau and John D. Joannopoulos. *Enhancement of microcavity lifetimes using highly dispersive materials*. Physical Review E, vol. 71, no. 2, page 026602, 2005. (Cited on pages 4, 78 and 81.)
- [Soljačić 2005b] Marin Soljačić, Elefterios Lidorikis, John D. Joannopoulos and Lene Vestergaard Hau. *Ultralow-power all-optical switching*. Applied Physics Letters, vol. 86, no. 17, page 171101, 2005. (Cited on pages 23 and 27.)
- [Spinelli 1998] L. Spinelli, G. Tissoni, M. Brambilla, F. Prati and L. A. Lugiato. *Spatial solitons in semiconductor microcavities*. Physical Review A, vol. 58, no. 3, pages 2542–2559, 1998. (Cited on page 34.)
- [Strekalov 2003] Dmitry V. Strekalov, David Aveline, Robert Thompson, Andrey B. Matsko and Lute Maleki. *Stabilizing an optoelectronic microwave oscillator with photonic filters*. Journal of Lightwave Technology, vol. 21, no. 12, pages 3052–3061, December 2003. (Cited on page 23.)
- [Su 2006] Hui Su and Shun-Lien Chuang. *Room-temperature slow light with semiconductor quantum-dot devices*. Optics letters, vol. 31, no. 2, pages 271–273, January 2006. (Cited on page 12.)
- [Taillaert 2002] Dirk Taillaert, Wim Bogaerts, Peter Bienstman, Thomas F. Krauss, Peter Van Daele, Ingrid Moerman, Steven Verstuyft, Kurt De Mesel and Roel Baets. *An out-of-plane grating coupler for efficient butt-coupling between compact planar waveguides and single-mode fibers*. IEEE Journal of Quantum Electronics, vol. 38, no. 7, pages 949–955, 2002. (Cited on pages 93 and 98.)
- [Takahashi 2007] Yasushi Takahashi, Hiroyuki Hagino, Yoshinori Tanaka, Bong-Shik Song, Takashi Asano and Susumu Noda. *High-Q nanocavity with a 2-ns photon lifetime*. Optics express, vol. 15, no. 25, pages 17206–13, December 2007. (Cited on page 23.)

- [Talneau 2008] Anne Talneau, K. H. Lee, S. Guilet and Isabelle Sagnes. *Efficient coupling to W1 photonic crystal waveguide on InP membrane through suspended access guides*. Applied Physics Letters, vol. 92, no. 6, page 061105, 2008. (Cited on page 93.)
- [Tamir 1977] Theodor Tamir and Song-Tsuen Peng. *Analysis and design of grating couplers*. Applied Physics A: Materials Science & Processing, vol. 14, no. 3, pages 235–254, 1977. (Cited on pages 98 and 99.)
- [Tanabe 2006] Takasumi Tanabe, Masaya Notomi, Eiichi Kuramochi, Akihiko Shinya and H. Taniyama. *Trapping and delaying photons for one nanosecond in an ultrasmall high-Q photonic-crystal nanocavity*. Nature Photonics, vol. 1, no. 1, pages 49–52, 2006. (Cited on page 23.)
- [Tsai 2011] Cheng-Chia Tsai, Jacob Mower and Dirk Englund. *Directional free-space coupling from photonic crystal waveguides*. Optics express, vol. 19, no. 21, pages 20586–96, October 2011. (Cited on page 99.)
- [Vahala 2003] Kerry J. Vahala. *Optical microcavities*. Nature, vol. 424, no. 6950, pages 839–46, August 2003. (Cited on page 23.)
- [Van Laere 2007] Frederik Van Laere, Günther Roelkens, Melanie Ayre, Jonathan Schrauwen, Dirk Taillaert, Dries Van Thourhout, Thomas F. Krauss and Baet. *Compact and highly efficient grating couplers between optical fiber and nanophotonic waveguides*. Journal of Lightwave Technology, vol. 25, no. 1, pages 151–156, 2007. (Cited on pages 93 and 98.)
- [Vlasov 2005] Yurii A. Vlasov, Martin O’Boyle, Hendrik F. Hamann and Sharee J. McNab. *Active control of slow light on a chip with photonic crystal waveguides*. Nature Letters, vol. 438, pages 65–69, 2005. (Cited on pages 19 and 77.)
- [Vlasov 2006] Yurii A. Vlasov and Sharee J. McNab. *Coupling into the slow light mode in slab-type photonic crystal waveguides*. Optics letters, vol. 31, no. 1, pages 50–52, January 2006. (Cited on page 93.)
- [Wang 2000] Hai Wang, D. J. Goorskey, W. H. Burkett and Min Xiao. *Cavity-linewidth narrowing by means of electromagnetically induced transparency*. Optics letters, vol. 25, no. 23, pages 1732–4, December 2000. (Cited on page 23.)
- [Weis 2010] Stefan Weis, Rémi Rivière, Samuel Deléglise, Emanuel Gavartin, Olivier Arcizet, Albert Schliesser and Tobias J. Kippenberg. *Optomechanically induced transparency*. Science (New York, N.Y.), vol. 330, no. 6010, pages 1520–3, December 2010. (Cited on page 23.)

- [Wu 2007] Haibin Wu and Min Xiao. *Cavity linewidth narrowing and broadening due to competing linear and nonlinear dispersions*. Optics letters, vol. 32, no. 21, pages 3122–4, November 2007. (Cited on page 23.)
- [Xu 2007] Qianfan Xu, Po Dong and Michal Lipson. *Breaking the delay-bandwidth limit in a photonic structure*. Nature Physics, vol. 3, no. 6, pages 406–410, April 2007. (Cited on page 23.)
- [Yablonovitch 1987] Eli Yablonovitch. *Inhibited spontaneous emission in solid-state physics and electronics*. Physical review letters, vol. 58, no. 20, pages 2059–2062, 1987. (Cited on page 15.)
- [Yacomotti 2006a] Alejandro M. Yacomotti, Paul Monnier, Fabrice Raineri, B. Bakir, C. Seassal, Rama Raj and Juan Ariel Levenson. *Fast Thermo-Optical Excitability in a Two-Dimensional Photonic Crystal*. Physical Review Letters, vol. 97, no. 14, page 143904, October 2006. (Cited on pages 34 and 71.)
- [Yacomotti 2006b] Alejandro M. Yacomotti, Fabrice Raineri, C. Cojocar, Paul Monnier, Juan Ariel Levenson and Rama Raj. *Nonadiabatic Dynamics of the Electromagnetic Field and Charge Carriers in High-Q Photonic Crystal Resonators*. Physical Review Letters, vol. 96, no. 9, page 093901, March 2006. (Cited on page 34.)
- [Yang 2004] Wenge Yang, Amitabh Joshi and Min Xiao. *Enhancement of the cavity ringdown effect based on electromagnetically induced transparency*. Optics letters, vol. 29, no. 18, pages 2133–5, September 2004. (Cited on page 23.)
- [Yanik 2003] Mehmet Fatih Yanik, Shanhui Fan, Marin Soljačić and John D. Joannopoulos. *All-optical transistor action with bistable switching in a photonic crystal cross-waveguide geometry*. Optics letters, vol. 28, no. 24, pages 2506–8, December 2003. (Cited on page 23.)

Slow light in two dimensional semi-conductor photonic crystals

Abstract:

We report on the combination of slow light propagation with the resonance properties of a photonic crystal cavity and with the slow mode of a photonic crystal waveguide.

We demonstrate theoretically and experimentally that slow light induced by the Coherent Population Oscillation (CPO) effect enables to have small-size and ultra-high quality (Q) factor cavity, regardless of the technological and design issues. The experimental proof is performed in an L3 2D PhC cavity with semiconductor quantum wells as active, medium in which the CPO effect is induced. We achieve a cavity Q -factor of 520000 which corresponds to an enhancement 138 comparing to the original Q -factor of the cavity.

We present a theoretical approach to the combination of CPO-based slow light and slow mode in PhC waveguides, showing that the total group index is a multiplication of the group indices associated respectively to the CPO slow light and to the waveguide slow mode. We also set the basis for the experimental demonstration by designing and fabricating samples in the clean room facilities of LPN and addressing the challenging issue of coupling and extracting light in and from the waveguides. A particular design of the PhC in the waveguide is issued as a grating that allows to couple light perpendicularly to the plane of the PhC from free space. The vertical coupler has also been designed and fabricated along the waveguide and has been experimentally characterized. Slow light based on CPO effect in the PhC waveguides is always under experimental investigation.

Keywords: Slow light, coherent population oscillations, photonic crystals, cavity, waveguide
